

## ABSTRACT

Title of dissertation: NON-CLASSICAL LIGHT FOR QUANTUM INFORMATION

Elizabeth Anne Goldschmidt  
Doctor of Philosophy, 2014

Dissertation directed by: Professor Steven Rolston  
Dr. Alan Migdall  
Department of Physics

Non-classical light is both easily encoded with quantum information and robust against decoherence, making it a key resource that enables many quantum information applications including quantum computing, quantum communication, and quantum metrology. We present a wide range of experimental and theoretical research toward the generation, detection, characterization, and storage of non-classical states of light with an eye toward quantum information applications.

To provide a basis for the rest of the work, we begin by discussing theoretically the role of photon number statistics in optical quantum information and the use of second-order optical coherence to characterize non-classical light. Building on that, we present an original tool for the difficult problem of reconstructing the underlying mode distribution of multi-mode optical fields using simple measurements of higher-order optical coherence.

We then move on to the problem of generating and storing single photons. We do this in a solid-state medium, a rare-earth ion-doped crystal, with a long-lived spin

transition ideal for storing quantum information. We experimentally demonstrate the feasibility of this concept by showing correlations between the optical fields that herald storage and retrieval of collective excitations. This scheme can be used for the two important and distinct applications of generating single photons on-demand and storing quantum information and entanglement.

The detection of non-classical light is a task as important as its generation. To this end, we study detectors with near unity detection efficiency and photon number resolution for use in quantum-enabled metrology. We use such a detector to experimentally demonstrate compression of spatial fringes and investigate the possibility of improving measurement resolution with classical and non-classical light.

Finally, we report a set of experiments using photon number statistics to characterize classical and non-classical light. We measure suppression of unwanted multiphoton emission in a heralded single photon source based on four-wave mixing in microstructure optical fiber. And we, for the first time, experimentally demonstrate reconstruction of multi-mode classical and non-classical light from measured photon number statistics.

# NON-CLASSICAL LIGHT FOR QUANTUM INFORMATION

by

Elizabeth Anne Goldschmidt

Dissertation submitted to the Faculty of the Graduate School of the  
University of Maryland, College Park in partial fulfillment  
of the requirements for the degree of  
Doctor of Philosophy  
2014

Advisory Committee:  
Professor Steven Rolston, Chair  
Dr. Alan Migdall, Co-Chair/Adviser  
Professor Christopher Lobb  
Professor Christopher Monroe  
Professor Luis Orozco  
Professor Edo Waks

© Copyright by  
Elizabeth Anne Goldschmidt  
2014

## Dedication

For Aaron.

## Acknowledgments

The work in this thesis was all the result of collaborative efforts with colleagues at NIST, ANU, and elsewhere. First thanks go to my advisor Alan Migdall who mentored me over six and a half years. My development as a physicist and an experimentalist would have been impossible without the support, encouragement, and advice I received from Alan. In addition, Sergey Polyakov at NIST and Matt Sellars at ANU both provided an enormous amount of guidance on many projects and I owe them a great debt. And much thanks go to my partner on the praseodymium experiment both at NIST and ANU, Sarah Beavan.

Many others contributed directly and indirectly to the work presented. Thanks to the members of the Migdall group at NIST including Elohim Becerra, Jun Chen, Matt Eisaman, Jay Fan, Boris Glebov, Alex Ling, Aaron Pearlman, and Joffrey Peters and to the members of the Sellars group at ANU including Rose Ahlefeldt, John Bartholomew, and Morgan Hedges for all their help. In addition I have benefited over the years by helpful discussions with many others at NIST and elsewhere including Mohammad Hafezi, Zachary Levine, Jevon Longdell, Sae Woo Nam, Alessandro Restelli, Jake Taylor, and Christoph Wildfeuer. And I would like to thank all my friends and family for supporting me throughout my PhD work, particularly my parents, Lynn and Bob Goldschmidt, and my husband, Aaron Pearlman.

Finally, I would like to acknowledge the generous financial support I received from the Joint Quantum Institute through my graduate career.

# Table of Contents

Table of Contents	iv
List of Figures	vi
1 Introduction	1
1.1 Single photons . . . . .	3
1.2 Quantum memory . . . . .	5
1.3 Detection . . . . .	8
2 Photon statistics	10
2.1 Quantized electromagnetic field . . . . .	10
2.2 Correlation functions . . . . .	13
2.2.1 Cauchy-Schwarz inequality . . . . .	16
2.2.2 Measuring correlation . . . . .	20
2.3 Types of light . . . . .	22
2.3.1 Coherent states . . . . .	22
2.3.2 Thermal light . . . . .	23
2.3.3 Single photon states . . . . .	24
2.4 Characterizing light . . . . .	26
2.4.1 Heralded single photon sources . . . . .	26
2.4.2 Cross-correlation . . . . .	31
2.4.3 Mode reconstruction . . . . .	33
3 Quantum optics in rare-earth systems	40
3.1 Basic properties . . . . .	41
3.2 Spectral hole burning . . . . .	47
3.3 Quantum memory . . . . .	50
3.3.1 Experimental methods . . . . .	54
3.3.2 Correlation model . . . . .	62
3.3.3 Experimental results . . . . .	64
3.3.4 Spectral filtering . . . . .	68

4	Non-classical detection for metrology	70
4.1	Fringe compression . . . . .	73
4.2	Beam contrast . . . . .	76
5	Characterizing light	82
5.1	Heralded single photon source . . . . .	82
5.2	Non-local realism . . . . .	90
5.3	Mode reconstruction . . . . .	97
6	Conclusion and outlook	104
	Bibliography	106



## List of Figures

2.1	Hanbury Brown-Twiss interferometer . . . . .	21
2.2	Heralded photon number distributions . . . . .	30
2.3	$g^{(2)}$ contour lines . . . . .	36
2.4	Understanding mode reconstruction . . . . .	37
2.5	Mode reconstruction sensitivity . . . . .	38
3.1	Rare-earth orbitals . . . . .	43
3.2	Rare-earth energy levels . . . . .	44
3.3	$\text{Pr}^{3+}:\text{Y}_2\text{SiO}_5$ level structure . . . . .	46
3.4	Spectral hole burning . . . . .	48
3.5	State preparation for quantum memory . . . . .	51
3.6	Praseodymium energy levels . . . . .	56
3.7	Experimental Setup. . . . .	60
3.8	Phase-matching . . . . .	61
3.9	Storage of collective excitations . . . . .	66
3.10	Spectral hole-burning filter . . . . .	69
4.1	Diffraction . . . . .	74
4.2	Finding the center of a distribution . . . . .	77
4.3	Beam contrast . . . . .	78
4.4	Calculated spatial distributions . . . . .	80
5.1	Image of microstructure fiber . . . . .	84
5.2	Fiber pair source experiment . . . . .	86
5.3	$g^{(2)}$ vs. pump power . . . . .	88
5.4	Poincaré sphere . . . . .	93
5.5	Non-local violation setup . . . . .	94
5.6	Non-local realism violation . . . . .	96
5.7	Mode reconstruction experiment . . . . .	99
5.8	Reconstructed thermal modes . . . . .	101
5.9	Reconstructed Poissonian and thermal modes . . . . .	102
5.10	Reconstructed single photon and thermal modes . . . . .	103

## Chapter 1: Introduction

For many years after the development of quantum mechanics, debates about new concepts such as quantum measurement, superposition, and entanglement were thought to be primarily philosophical. Experiments on single quantum systems were far outside the technical state of the art at the time and, as such, many of the counter-intuitive concepts inherent to quantum mechanics were thought to be untestable. The 1970s and 1980s saw an explosion of results opening up entire new quantum possibilities as new experimental techniques allowed studies of single quantum systems such as single trapped atoms and single photons [1, 2] culminating with the 2012 Nobel prize in physics [3, 4]. The paradox presented by Einstein, Podolsky, and Rosen [5] was shown to be testable experimentally [6] and quantum entanglement was verified at the expense of hidden variable theories and local realism [1, 7]. It was shown that simulating a large quantum system would be possible only with another quantum system and the idea of quantum computing was born [8, 9]. The quantum no-cloning theorem [10] along with the uncertainty principle combined to give rise to the possibility of perfect security with quantum resources [11]. Since then, there has been an explosion of research in the field of quantum information designing systems that take advantage of quantum mechanical

phenomena to implement faster computing, more secure communication, and more precise measurement [12, 13].

The fundamental unit of all these quantum information schemes is the quantum bit, or qubit. Unlike a classical bit, a quantum two-state system can be in a coherent superposition of its two states, or even part of a collective entangled state with other qubits in the system. The large space of possible states, exponentially larger than the number of classically possible states, is the underlying reason why simulating a quantum system is exceedingly hard on a classical computer and why a quantum computer can perform tasks of much higher complexity. The existence of multiple, non-commuting bases in which a qubit can be encoded, and the uncertainty relation that accompanies such observables, leads to quantum secure protocols in which an eavesdropper cannot collect information without altering the qubits in a detectable way. And the ability to reduce quantum noise below the limit obeyed by classical systems opens up the possibility of making measurements with greater and greater precision.

In the context of quantum information, photons are often referred to as flying qubits because they are so well-suited for transmitting quantum information. Light is generally robust against decoherence because it only weakly interacts with its environment and thus can maintain a quantum mechanical state for a long time. In addition, light has many natural bases that can be used to define qubit states, including polarization, phase, photon number, arrival time, orbital angular momentum, and frequency. To this end, we present here progress toward generating, storing, and detecting states of light suitable for a variety of quantum information applications.

## 1.1 Single photons

A major task in quantum optics today is producing single photons. Optical quantum information is often encoded in such a way that a single photon holds a single qubit of information. One reason for this is the inherent security of single photon communication. Quantum security is based on the ability to measure in non-commuting bases such that an eavesdropper will alter the state in a detectable way [14]. However, if a qubit is held in more than one photon, the channel is susceptible to photon number splitting attacks in which an eavesdropper makes different measurements on different photons. In addition, many other optical quantum information protocols, such as linear optics quantum computing [15], rely on the two photon interference effect known as Hong-Ou-Mandel interference, which requires single photon inputs [16].

Producing photons one at a time, however, turns out to be a difficult task. Virtually all light sources exhibit natural intensity fluctuations. In particular, sources that we term classical, including the lasers and lamps used in optics laboratories, produce photons at a rate that fluctuates in time according to a well-known distribution. Even if we attenuate a classical source such that we rarely see any photons emitted, there will still be a finite probability that the source will emit more than one photon at a time. Reducing the multi-photon component of a field is therefore an important task and there are many methods for doing just that [17]. In particular, in chapters 2 and 5 we discuss theoretical and experimental work characterizing the single photon nature of a light field [18].

Single photon sources are generally based either on single emitters, such as single atoms, ions, or solid-state defects, which by their nature can only emit one photon at a time, or nonlinear processes in macroscopic systems that produce photons in pairs such that one member of the pair can herald the presence of the other. In the case of single emitters, collection is a significant issue because the photon is emitted into  $4\pi$  steradians unless the system is specifically engineered to emit in a preferred direction. As a result, although there has been much progress coupling single emitters to optical cavities [17, 19, 20], the primary method to date of generating single photons has been via pair production. In particular, spontaneous parametric down conversion (SPDC) in nonlinear crystals is the basis of most single photon sources used to date [17]. Pair production is an inherently probabilistic process, resulting in photons at random times. A photon pair source can be combined with a quantum memory to generate photons on demand, though engineering a highly efficient quantum memory with spectral properties matched to a photon pair source is a significant challenge [21].

In chapters 3 and 5 we discuss two methods for producing photon pairs other than SPDC, four-wave mixing in optical fiber and Raman transitions in atomic ensembles [18, 22]. Producing photon pairs in an optical fiber has a number of advantages over SPDC because photons are produced directly in the single spatial mode of the optical fiber. Atomic ensemble-based photon pair sources have the benefit that the ensemble acts as a built in quantum memory, allowing the photons to be produced on demand, rather than randomly.

Many pair production techniques, including SPDC and four-wave mixing in

optical fiber, produce photons in multiple spectral modes. For quantum information applications, this frequency entanglement is generally undesirable as it causes photons to be non-identical or leads to destruction of other, desired entanglement [23, 24]. In chapter 2 we present a new method that can help determine the degree of frequency entanglement in many photon pair sources and in chapter 5 we present a proof-of-principle experiment demonstrating our method [25].

We noted earlier that the foundations of quantum information were built on the experimental work demonstrating the triumph of quantum theory over local realism [5, 6]. Recently, a new class of non-local hidden variable theories was shown to have predictions different from quantum theory [26]. In chapter 5 we use single photons to show simultaneous violation of both local and non-local hidden variable theories consistent with quantum theory [27]. By demonstrating the infeasibility of both local and non-local realism as underlying descriptions of the natural world, this work suggests that realism (an external reality exists independent of observation), rather than locality (events in space-like separated regions cannot affect each other), is the aspect of classical physics that must be abandoned in favor of quantum mechanics.

## 1.2 Quantum memory

Many quantum information protocols require a quantum memory that allows the transfer of quantum information between propagating photons and internal states of matter to locally store quantum information [28]. Some form of quantum memory is necessary for optical quantum computing protocols that have probabilis-

tic gates or teleportation operations [29]. Long distance quantum communication requires quantum memory to transmit quantum information in a practical amount of time [30]. Loss in optical fiber increases exponentially with distance. Unlike classical communication, where we can use bright states and amplifiers to overcome this loss, quantum communication requires transmission of single photons (or other similarly loss-intolerant states). Thus, the loss in optical fiber means that the time to directly transmit quantum information over a fiber link scales exponentially with distance, making long-distance communication in this manner unfeasible. In [30] it was shown that quantum memories can serve as the basis for quantum repeaters, which allow quantum communication in a time that scales polynomially, rather than exponentially, with distance. A quantum repeater relies on generating and storing entanglement in quantum memory nodes spaced along the communication channel. These nodes break the entire communication length into a series of shorter segments. Entanglement is heralded by transmission of single photons over the shorter segments between quantum memory nodes. If a heralding photon is lost in one or more of the segments, entanglement generation only has to be retried on the segments where it failed. The other quantum memory nodes store the entanglement on the segments that succeeded. The beneficial scaling is a result of the fact that, unlike with direct communication in which a single photon must traverse the entire distance, loss in one part of the link does not negate successful transmission in another. Once entanglement is established over the entire channel, quantum teleportation allows transmission of quantum information over the full distance [31].

Quantum memory can also be used to engineer sources of non-classical light.

As mentioned earlier, heralded single photon sources in combination with quantum memory, such as the atomic-ensemble based system in chapter 3, produce photons on demand, rather than at random, heralded times [21]. One arm of the pair source (heralding arm) goes to a detector while the other (heralded arm) goes into a quantum memory. Rather than heralding a propagating photon, the heralding photon heralds storage of a single photon in the quantum memory, which can be retrieved from the memory on demand. And quantum memory can allow more complicated non-classical states of light, such as higher order Fock states, to be produced by heralded storage of known states [32].

An ideal quantum memory can store quantum information for long enough to perform some computation or communication protocol. Long storage times are achieved in systems that keep the qubit isolated from the surrounding environment because interactions with the environment cause loss and decoherence. In addition, an ideal quantum memory is based on a system that is strongly coupled to light so that the quantum information is not lost in the process of converting between optical and matter-based qubits. Quantum memory demonstrations in rare-earth ion-doped crystals (REIC) have shown storage times of tens of seconds as well as recall efficiencies well over 50 % [33–35]. In addition, REIC are solid state systems, which opens up the possibility of integrated photonic systems in which quantum protocols are all carried out on chip. In chapter 3 we present experimental progress toward implementing a quantum memory in a solid-state REIC [22].



### 1.3 Detection

Detection at the single photon level is a crucial aspect of optical quantum information protocols [17, 36]. Most single photon detectors produce an electronic signal upon absorption of one or more photons, without discriminating the number of photons present. There are many applications in quantum information and elsewhere, however, where photon number resolution is useful or required [15, 17, 25]. One such method for implementing photon number resolving detection is by multiplexing single photon detectors. In chapter 5 we report an experiment using such a detection scheme to reconstruct the modes of mixed states of light. Multiplexed detection, while relatively simple to implement, has drawbacks that include photon number resolution limited by the number of detectors available (or the acceptable time delay for temporal multiplexing) and reduced sensitivity due to splitting probabilities [37] (which can be reduced, but not eliminated with active multiplexing [38]). True photon number resolution is possible using detectors such as a transition edge sensor (TES), which measures the change in resistance in a superconducting film due to the temperature rise that accompanies absorption of photons. In chapter 4 we report results using a TES to study how photon number resolution can be used in imaging and metrology applications [39].

We also report in this thesis theoretical and experimental work showing that photon number resolved detection can be a useful tool for characterizing light. In particular, we study the relationship between the photon number statistics of a light field and the properties of its source in chapter 2 and show that we can use

multiplexed single photon detectors to reconstruct the underlying mode spectrum of various light fields in chapter 5, an important task for engineering and diagnosing many sources of non-classical light [25].

## Chapter 2: Photon statistics

Throughout this thesis we will frequently use photon number statistics to characterize various light fields. That light is composed of discrete particles (photons) is an inherently quantum concept, and thus photon number statistics provide an inherently quantum description of light. We will show that such a description is useful for discussing light in the context of many quantum information applications. In addition, modern photodetection makes it possible to directly access the photon number statistics of many fields and we will discuss experiments that take advantage of photon number resolved detection. In this chapter we introduce the language for discussing photon number statistical properties and introduce some specific scenarios in which we can use photon number statistical measurements to learn more about a light field.

### 2.1 Quantized electromagnetic field

Following is a brief review of the well-known quantization of the electromagnetic field that can be found in many books [13, 40, 41]. Classically, light is described by propagating electromagnetic waves obeying Maxwell's equations in free space. We write the transverse electric ( $\mathbf{E}$ ) and magnetic ( $\mathbf{B}$ ) fields in terms of a vector

potential ( $\mathbf{A}$ ):

$$\begin{aligned}\nabla \times \mathbf{E} &= -\frac{\partial \mathbf{B}}{\partial t} & \nabla \cdot \mathbf{E} &= 0 \\ \nabla \times \mathbf{B} &= \frac{1}{c^2} \frac{\partial \mathbf{E}}{\partial t} & \nabla \cdot \mathbf{B} &= 0 \\ \mathbf{B} &= \nabla \times \mathbf{A} & \mathbf{E} &= -\frac{\partial \mathbf{A}}{\partial t}.\end{aligned}$$

Working in the coulomb gauge ( $\nabla \cdot \mathbf{A} = 0$ ) we can solve the wave equation for the vector potential ( $-\nabla^2 \mathbf{A} + \frac{1}{c^2} \frac{\partial^2 \mathbf{A}}{t^2} = 0$ ) to obtain:

$$\mathbf{A}(\mathbf{r}, t) = \sum_{\mathbf{k}, \epsilon} \mathbf{e}_{\mathbf{k}\epsilon} \left( A_{\mathbf{k}\epsilon} e^{-i(\omega_k t - \mathbf{k} \cdot \mathbf{r})} + A_{\mathbf{k}\epsilon}^* e^{i(\omega_k t - \mathbf{k} \cdot \mathbf{r})} \right) \quad (2.1)$$

where we have decomposed  $\mathbf{A}$  into modes of particular wavevector components  $\mathbf{k}$  ( $\omega_k = c|\mathbf{k}|$ ) and polarizations  $\epsilon$ . We can now write the transverse electric field for a propagating electromagnetic wave as

$$\begin{aligned}\mathbf{E}(\mathbf{r}, t) &= \mathbf{E}^{(+)}(\mathbf{r}, t) - \mathbf{E}^{(-)}(\mathbf{r}, t) \\ \mathbf{E}^{(+)}(\mathbf{r}, t) &= \sum_{\mathbf{k}, \epsilon} \mathbf{e}_{\mathbf{k}\epsilon} (i\omega_k) A_{\mathbf{k}\epsilon} e^{-i(\omega_k t - \mathbf{k} \cdot \mathbf{r})} \\ \mathbf{E}^{(-)}(\mathbf{r}, t) &= \sum_{\mathbf{k}, \epsilon} \mathbf{e}_{\mathbf{k}\epsilon} (i\omega_k) A_{\mathbf{k}\epsilon}^* e^{i(\omega_k t - \mathbf{k} \cdot \mathbf{r})}\end{aligned} \quad (2.2)$$

where  $\mathbf{e}_{\mathbf{k}\epsilon}$  is a unit polarization vector and the energy contained in the field in a volume  $V$  is

$$\mathcal{E} = \sum_{\mathbf{k}, \epsilon} \epsilon_0 V \omega_k^2 (A_{\mathbf{k}\epsilon} A_{\mathbf{k}\epsilon}^* + A_{\mathbf{k}\epsilon}^* A_{\mathbf{k}\epsilon}). \quad (2.3)$$

We notice that under the following transformation each mode acts as an independent quantum harmonic oscillator with frequency  $\omega_k$ :

$$A_{\mathbf{k}\epsilon} \rightarrow -i\sqrt{\frac{\hbar}{2\epsilon_0 V \omega_k}} \hat{a}_{\mathbf{k}\epsilon} \quad A_{\mathbf{k}\epsilon}^* \rightarrow i\sqrt{\frac{\hbar}{2\epsilon_0 V \omega_k}} \hat{a}_{\mathbf{k}\epsilon}^\dagger$$

in which  $\hat{a}$  and  $\hat{a}^\dagger$  are the bosonic creation and annihilation operators for a single mode of the quantized electromagnetic field and the quantum hamiltonian is

$$H = \sum_{\mathbf{k}, \epsilon} \frac{1}{2} \hbar \omega_k \left( \hat{a}_{\mathbf{k}\epsilon}^\dagger \hat{a}_{\mathbf{k}\epsilon} + \hat{a}_{\mathbf{k}\epsilon} \hat{a}_{\mathbf{k}\epsilon}^\dagger \right). \quad (2.4)$$

We can write the quantum mechanical electric field operator for a single mode  $\mathbf{k}, \epsilon$  in units of  $\sqrt{\frac{\hbar \omega_k}{2\epsilon_0 V}}$  and define the phase of the field  $\theta = \omega_k t - \mathbf{k} \cdot \mathbf{r}$ :

$$\hat{\mathbf{E}}(\theta) = \hat{\mathbf{E}}^{(+)}(\theta) + \hat{\mathbf{E}}^{(-)}(\theta) = \hat{a} e^{-i\theta} + \hat{a}^\dagger e^{i\theta}. \quad (2.5)$$

Unless otherwise noted, we will assume we have a single mode of the quantized electromagnetic field and drop the  $\mathbf{k}\epsilon$  subscripts. It is often useful to write the quantum state of a light field in the photon number, or Fock, basis where a photon is defined as a single excitation in a single mode of the field and an  $n$  photon state is written as  $|n\rangle$ . We recall some of the properties of the bosonic creation and annihilation operators in the Fock basis:

$$\hat{a}^\dagger \hat{a} = \hat{n}, \quad \hat{a}^\dagger |n\rangle = \sqrt{n+1} |n+1\rangle, \quad \hat{a} |n\rangle = \sqrt{n} |n-1\rangle, \quad [\hat{a}, \hat{a}^\dagger] = 1.$$

In the next section we will show some implications of the quantum description of light.

## 2.2 Correlation functions

We discuss here how to describe light in terms of its intensity fluctuations and the real implications on those fluctuations due to the quantized nature of the field. In particular, we discuss the normalized correlation functions of a light field, where the  $j^{\text{th}}$  order correlation function is the (normalized)  $j^{\text{th}}$  moment of the intensity of the field. We see that the limits placed on these quantities are different under the classical and quantum descriptions of light, giving rise to the well known Cauchy-Schwarz inequality for classical light  $g^{(2)}(0) \geq 1$  which we discuss in detail below [40, 41].

The second-order auto-correlation in this inequality,  $g^{(2)}$ , is a special case of the  $j^{\text{th}}$  normalized correlation function that describes the correlation between the electric field at up to  $2j$  positions in space and time. We can write the general form of these functions in terms of the electric field operators introduced in the previous section. We use subscripts to denote the points in space ( $\mathbf{r}_j$ ) and write the field operators as functions of time.

$$\begin{aligned}
 &g^{(j)}(t_1, \dots, t_j, t'_1, \dots, t'_j; \mathbf{r}_1, \dots, \mathbf{r}_j, \mathbf{r}'_1, \dots, \mathbf{r}'_j) \\
 &= \frac{\langle \hat{E}_1^{(-)}(t_1) \cdots \hat{E}_j^{(-)}(t_j) \hat{E}_j'^{(+)}(t'_j) \cdots \hat{E}_1'^{(+)}(t'_1) \rangle}{\langle \hat{E}_1^{(-)}(t_1) \hat{E}_1^{(+)}(t_1) \rangle^{1/2} \cdots \langle \hat{E}_j'^{(-)}(t'_j) \hat{E}_j'^{(+)}(t'_j) \rangle^{1/2}} \quad (2.6)
 \end{aligned}$$

Classically, we measure the energy contained in a light field to obtain the classical intensity  $I = E^{(-)}E^{(+)}$ . Thus, with classical detection schemes we have

straightforward access to the  $j^{\text{th}}$  order **intensity** correlation functions between  $j$  points in space and time. Classically, the electric field is described by complex numbers and we can regroup terms to obtain:

$$g_{\text{classical}}^{(j)}(t_1, \dots, t_j; \mathbf{r}_1, \dots, \mathbf{r}_j) = \frac{\langle I_1(t_1) \cdots I_j(t_j) \rangle}{\langle I_1(t_1) \rangle \cdots \langle I_j(t_j) \rangle}. \quad (2.7)$$

The quantum mechanical formalism tells us that the electric field should actually be described with quantum mechanical operators. In this case, photodetection involves measuring the photon number operator  $\hat{a}^\dagger \hat{a}$ , which gives us access to the same set of correlation functions, written with care taken to preserve the normal and time ordering of the quantum mechanical operators [42]:

$$g_{\text{quantum}}^{(j)}(t_1, \dots, t_j; \mathbf{r}_1, \dots, \mathbf{r}_j) = \frac{\langle \hat{a}_1^\dagger(t_1) \cdots \hat{a}_j^\dagger(t_j) \hat{a}_j(t_j) \cdots \hat{a}_1(t_1) \rangle}{\langle \hat{n}_1(t_1) \rangle \cdots \langle \hat{n}_j(t_j) \rangle}. \quad (2.8)$$

We will focus on some special cases of these correlation functions that give us intuition into the statistical properties of light. The second-order intensity correlation function in particular provides a framework for describing light that is very useful. We are interested in particular in the second-order intensity auto-correlation of a stationary field with itself at some time delay as well as in the second-order intensity cross-correlation between two fields. For stationary light fields, where the average intensity is constant in time, we only need to identify a time delay between and the averaging denoted by  $\langle \rangle$  is over time. We write the intensity auto-correlation

as a function of time delay  $\tau$  as:

$$g^{(2)}(\tau) = \frac{\langle \hat{a}^\dagger(t - \tau) \hat{a}^\dagger(t) \hat{a}(t) \hat{a}(t - \tau) \rangle}{\langle \hat{a}^\dagger \hat{a} \rangle^2}. \quad (2.9)$$

The auto-correlation function tells us about the statistical properties of a single stationary field. At long enough time delays  $g^{(2)}(\tau)$  always approaches 1 because the field loses its memory of previous times and can thus have no correlation with its past self. The value at zero time delay tells us about the “bunching” of a light field. A field with  $g^{(2)}(0) > 1$  is termed “bunched” and a field with  $g^{(2)}(0) < 1$  “anti-bunched”. These terms refer to the photons arriving together more or less frequently than they would for a random distribution. The dynamics in time of the auto-correlation function, in particular the time scale over which it approaches 1, provides information about the coherence and bandwidth of the light.

We can write a more general form of the second-order correlation function for any two fields, labeled 1 and 2, assuming that those labels refer to well-defined regions of space-time over which we integrate the total intensity, or photon number, of the field.  $g_{1,1}^{(2)}$  refers to the auto-correlation at zero time difference, which we will see below holds a special position. The auto-correlation at non-zero time difference  $g^{(2)}(\tau)$  is obtained by defining the fields 1 and 2 as the same field at different times. We write the correlation functions in terms of photon creation and annihilation operators and in terms of photon number operators using the notation  $\langle :: \rangle$  to denote normal ordering of operators (all  $\hat{a}$  operators following all  $\hat{a}^\dagger$  operators).



$$g_{1,2}^{(2)} = \frac{\langle \hat{a}_1^\dagger \hat{a}_2^\dagger \hat{a}_2 \hat{a}_1 \rangle}{\langle \hat{a}_1^\dagger \hat{a}_1 \rangle \langle \hat{a}_2^\dagger \hat{a}_2 \rangle} = \frac{\langle : \hat{n}_1 \hat{n}_2 : \rangle}{\langle \hat{n}_1 \rangle \langle \hat{n}_2 \rangle} \quad (2.10)$$

The cross-correlation between two different fields tells us about whether the fluctuations in two different fields are correlated, however we still require the individual auto-correlation functions to learn about the nature of the fluctuations themselves. For the cross-correlation we can assume that the photon creation and annihilation operators for the two different fields commute and remove the normal ordering.

Other correlation functions that we will discuss in this chapter are the zero time difference auto-correlation functions of arbitrary order:

$$g^{(j)} = \frac{\langle (\hat{a}^\dagger)^j (\hat{a})^j \rangle}{\langle n \rangle^j} \quad (2.11)$$

### 2.2.1 Cauchy-Schwarz inequality

We can use quantum formalism to write states of light which are not possible using the classical description of light. Under the classical formulation, there are no non-commuting operators. We use 2.7 to write the second-order classical correlation function:

$$g_{1,2}^{(2)} = \frac{\langle I_1 I_2 \rangle}{\langle I_1 \rangle \langle I_2 \rangle}. \quad (2.12)$$

Next we note that all real variables obey the Cauchy-Schwarz inequality:

$$\langle XY \rangle^2 \leq \langle X^2 \rangle \langle Y^2 \rangle \quad (2.13)$$

We can apply this to the classical statement of the correlation function to obtain constraints on the statistical distributions that are possible in the classical realm.

$$g_{1,1}^{(2)} \geq 1 \rightarrow g^{(2)}(0) \geq 1 \quad (2.14)$$

$$g_{1,2}^{(2)} \leq \sqrt{g_{1,1}^{(2)} \times g_{2,2}^{(2)}} \rightarrow g^{(2)}(\tau) \leq g^{(2)}(0), \quad g_{\text{cross}}^{(2)} \leq \sqrt{g_{\text{auto},1}^{(2)}(0) \times g_{\text{auto},2}^{(2)}(0)}$$

In particular, we see that anti-bunched light is not possible under the classical description of light, nor are two fields with cross-correlation greater than the geometric mean of their auto-correlations.

However, with the quantum description of light (eq. 2.10), the auto-correlation function is affected by measurement on the state. In particular, rather than the classical  $g_{1,1}^{(2)} = \langle n^2 \rangle / \langle n \rangle^2$  we obtain the quantum version:

$$g_{1,1}^{(2)} = \frac{\langle n^2 \rangle - \langle n \rangle}{\langle n \rangle^2} \quad (2.15)$$

This changes the constraints on the correlation functions due to the Cauchy-

Schwarz inequality. The new limits are (with the new terms in bold):

$$\begin{aligned}
 g_{1,1}^{(2)} &\geq 1 - \frac{\mathbf{1}}{\langle \mathbf{n}_1 \rangle} \\
 g_{1,2}^{(2)} &\leq \sqrt{\left( g_{1,1}^{(2)} + \frac{\mathbf{1}}{\langle \mathbf{n}_1 \rangle} \right) \left( g_{2,2}^{(2)} + \frac{\mathbf{1}}{\langle \mathbf{n}_2 \rangle} \right)}
 \end{aligned}
 \tag{2.16}$$

We can see that these new limits allow states that violate the classical inequalities, including anti-bunched light. We refer to such light as non-classical light because it must be described with the quantum formalism. We discuss below various types of classical and non-classical light. Finally, we note that for bright states of light ( $\langle n \rangle \gg 1$ ) the quantum limits approach the classical limits, and there is only a narrow range of non-classical light in this regime. At higher powers, other signatures of non-classicality, such as squeezing, are typically used to verify the quantum nature of light [43, 44].

It turns out that there exists a whole class of inequalities for the higher order auto-correlation functions as well [45]. The general form, as well as some more useful formulations are below.

$$\begin{aligned}
 g^{(k+l)} g^{(m-l)} &\geq g^{(k)} g^{(m)}, \quad k \geq m > l \\
 g^{(k+1)} &\geq g^{(k)} \\
 \sqrt{g^{(k+l)} g^{(k-l)}} &\geq g^{(k)}
 \end{aligned}
 \tag{2.17}$$

As the higher order correlation functions are in general more difficult to measure (see below), the second-order inequalities are in significantly more common use

age, however there are some examples of demonstrating non-classicality with these quantities [46, 47].

We take a brief moment to discuss the relationship between squeezing and photon number statistical fluctuations. Quantum mechanics, and in particular the quantum noise required by the Heisenberg uncertainty principle, ensures that light has naturally occurring fluctuations. In addition to the uncertainty relation for the electric field  $((\Delta\hat{E}(\theta))(\Delta\hat{E}(\theta + \pi/2)) \geq 1)$  we can introduce a phase operator  $\hat{\phi}$  and write a similar uncertainty relation for the phase and photon number of a field. There are many versions of such a phase operator, and using the Hermitian operator introduced in [48] we obtain  $(\Delta\hat{n})^2(\Delta\hat{\phi})^2 \geq 1/4$  [49]. For these uncertainty relations we term a light field “squeezed” if the the noise in one quadrature is reduced below its value for a minimum uncertainty state (the standard quantum limit), with a corresponding increase of noise in the other quadrature to satisfy the uncertainty relation [50]. The standard quantum limit for photon number variance is the same as the limit set by the Cauchy-Schwarz inequality on the classical formulation of  $g^{(2)}$ :  $(\Delta\hat{n})^2 = \langle\hat{n}^2\rangle - \langle\hat{n}\rangle^2 \geq \langle\hat{n}\rangle$ . So light that violates the classical Cauchy-Schwarz inequality can also be termed number-squeezed. However, light that is quadrature squeezed, in which the noise on the electric field is reduced below the standard quantum limit at some phase, does not necessarily violate the classical Cauchy-Schwarz inequality.

### 2.2.2 Measuring correlation

The first thing we note is the classical and quantum definitions of the second-order cross-correlation are identical, as the creation and annihilation operators commute with one another. As a result, we can measure the two fields with either classical intensity detectors or single photon counters. In the former case we simply take the time average of the product of the two detectors divided by the product of the time averages of the two detectors. In the latter we take the probability of joint detection divided by the product of the individual detection probabilities.

Measuring the zero time auto-correlation using either classical intensity detection or single photon counters (click/no-click detectors) requires inserting a 50/50 beamsplitter into the field and measuring the cross-correlation between two detectors at the output ports of the beamsplitter in a Hanbury Brown-Twiss geometry (see fig. 2.1) [51]. Assuming the two detectors are single photon counters that we label  $a$  and  $b$ , we denote the probability of a count in detector  $a$  ( $b$ ) as  $p_a$  ( $p_b$ ) and the probability of a joint detection  $p_{ab}$ . We then have  $g^{(2)} = p_{ab}/(p_a p_b)$  as long as  $1 \gg p_a, p_b \gg p_{ab}$ . Attenuation of the field does not affect the auto-correlation, so if this last assumption does not hold it is always possible to attenuate the field and obtain a more accurate measurement of  $g^{(2)}$  (until detector dark counts begin to affect the measurement).

To measure higher order correlation functions we must continue to split the field onto more and more detectors, making such measurements increasingly difficult. If we have classical intensity detection that is absolutely calibrated to the real

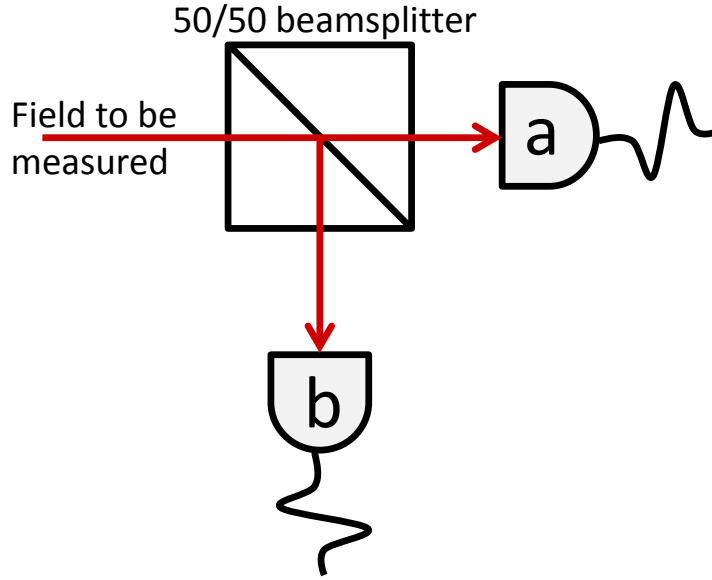


Figure 2.1: Hanbury Brown-Twiss interferometer. A field is incident on a 50/50 beamsplitter and detectors  $a$  and  $b$  at the output ports measure the photon counts. The auto-correlation of the incident field is  $g^{(2)} = p_{ab}/(p_a p_b)$  where  $p_i$  denotes the probability of a photodetection at detector(s)  $i$ .

photon number, we can measure the classical versions of the higher order correlation functions ( $g^{(k)} = \langle I^k \rangle / \langle I \rangle^k$ ) and then correct with terms that are functions of the mean photon number of the field. (e.g.  $g_{\text{quantum}}^{(2)} = g_{\text{classical}}^{(2)} - 1/\langle n \rangle$ ). The uncertainties of the intensity measurement and calibration lead to increasing uncertainty on the value of the correlation function for higher and higher order.

Photon number resolved detection, in which we obtain the photon number distribution of a field up to some maximum number  $k$ , allows direct measurement of the correlation functions up to the  $k^{\text{th}}$  order. We can convert from a photon number distribution to the auto-correlation functions as:

$$g^{(k)} = \frac{\sum_{n=0}^{\infty} \frac{n!}{(n-k)!} p(n)}{(\sum_{n=0}^{\infty} n p(n))^k} = \frac{\sum_{n=0}^{\infty} \frac{n!}{(n-k)!} p(n)}{\langle n \rangle^k}. \quad (2.18)$$

This final method has the benefit of allowing direct detection of the correlation functions with a single detector, however such photon number resolving detectors are relatively rare.

## 2.3 Types of light

We discuss here several types of light that are common in nature and/or relevant for quantum information science. We start by discussing classical states for which the classical versions of the Cauchy-Schwarz inequality (eq. 2.14) hold. We then discuss non-classical light and list some particular non-classical states and their corresponding statistical properties.

### 2.3.1 Coherent states

Optical coherent states, first described in 1963 by Roy Glauber, are a cornerstone of quantum optics and are the states produced by ideal single mode lasers operated well above threshold [42]. Coherent states are denoted by a complex value  $\alpha$  which is the eigenvalue of the state with respect to the annihilation operator ( $\hat{a}|\alpha\rangle = \alpha|\alpha\rangle$ ) and related to the mean photon number of the state as  $\langle\hat{n}\rangle = |\alpha|^2$ . Coherent states can be written in the number state basis and form a non-orthogonal, over-complete set of basis states:

$$|\alpha\rangle = e^{-|\alpha|^2/2} \sum_{n=0}^{\infty} \frac{\alpha^n}{\sqrt{n!}} |n\rangle. \quad (2.19)$$

We see that the probabilities of finding  $n$  photons in a coherent state  $|\alpha\rangle$  fall

along a Poisson distribution with mean photon number  $|\alpha|^2$  ( $p(n) = e^{-|\alpha|^2} \frac{|\alpha|^{2n}}{n!}$ ). The Poisson distribution governs uncorrelated, or random, events and thus coherent light exhibits auto-correlation functions  $g^{(k)}(0) = 1$  and minimally satisfies the classical Cauchy-Schwarz inequality (eq. 2.14). In fact we often refer to light with  $g^{(2)}(0) > 1$  as super-Poissonian and  $g^{(2)}(0) < 1$  as sub-Poissonian.

Coherent states have important similarities to classical, stable light waves. The quantum noise on the electric field quadratures of a coherent state is the minimum possible given the requirements of the Heisenberg uncertainty relation, and coherent states are termed minimum uncertainty states for this reason. Because they have a well-defined phase they are used in phase sensitive detection schemes such as homodyne and heterodyne detection that provide access to the complex field values of light rather than just the intensity.

### 2.3.2 Thermal light

Another type of classical light common in nature is thermal light, also called chaotic light [40, 41]. Sources in which many atoms or other discrete systems emit radiation independently of each other produce light with thermal number statistics. Thermal photon number statistics are what one expects from a harmonic oscillator in equilibrium at some temperature  $T$ . The probability that a harmonic oscillator (frequency  $\omega$ ) is in the  $n^{\text{th}}$  excited state is  $p(n) = e^{-n\hbar\omega/k_B T} / \sum_n e^{-n\hbar\omega/k_B T} = (1 - e^{-\hbar\omega/k_B T}) e^{-n\hbar\omega/k_B T}$ . The mean number of excitations of this probability distribution is  $\langle n \rangle = 1 / (e^{\hbar\omega/k_B T} - 1)$  and the probability distribution can be rewritten as  $p(n) =$



$\left(\frac{\langle n \rangle}{1+\langle n \rangle}\right)^n \frac{1}{1+\langle n \rangle}$ . Here, the harmonic oscillator is a particular mode of the quantized electromagnetic field and a thermal state is light with photon number distribution  $p(n) = \left(\frac{\langle n \rangle}{1+\langle n \rangle}\right)^n \frac{1}{1+\langle n \rangle}$ .

This distribution gives a zero-time auto-correlation  $g^{(2)}(0) = 2$ , denoting positive intensity correlation, or bunching. This intensity correlation occurs within some characteristic coherence time determined by the properties of the system. The bunched statistics apply to a single mode of thermal light. Many sources of chaotic light emit multiple independent spectral and/or spatial modes simultaneously. Because these modes are independent, they add together randomly, reducing the bunching, and the photon number statistics of the multi-mode field approaches Poissonian for many modes. Processes that produce chaotic light include blackbody radiation, fluorescence and luminescence, and spontaneous emission from a system of many emitters. In addition, many sources of twin beams or photon pairs that are based on spontaneous parametric processes in nonlinear media exhibit thermal number statistics in the number of pairs produced. We discuss the statistics of such a pair source later in this chapter.

### 2.3.3 Single photon states

Pure photon number states, and in particular single photons, have an important place in quantum information. Many quantum information schemes rely on single photons as flying qubits and exhibit degradation of security and/or fidelity in the presence of multi-photon states. To this end, much work has been done in

the last thirty years developing single photon sources based on a variety of physical systems. We note that higher order photon number states are also useful in some quantum information protocols, but are in general much more difficult to produce and much more sensitive to loss than single photons. We thus focus in this chapter solely on single photon sources.

Coherent and thermal states of light are insensitive to loss, in the sense that attenuation reduces the mean photon number of the light, but does not change the form of the statistics or the values of the auto-correlation functions  $g^{(k)}$ . Analogously, we discuss in this section **attenuated** single photon states ( $p(1) = \wp$ ,  $p(0) = 1 - \wp$ , and  $p(n > 1) = 0$ ) which exhibit loss-insensitive auto-correlation functions  $g^{(k)}(0) = 0$ , clearly violating the classical Cauchy-Schwarz inequality  $g^{(2)}(0) \geq 1$ . Pure one-photon Fock states, in which the vacuum component is zero, become attenuated single photon states under loss. And so we will refer to the mean photon number of a single photon state, which is simply  $\langle n \rangle = p(1) = \wp$ . Also, for any real single photon source, it is likely that the multi-photon component will not be completely suppressed. To this end, we use the second order correlation function  $g^{(2)}(0)$  to characterize the multi-photon emission from a single photon source. The closer  $g^{(2)}(0)$  is to zero, the closer the field is to a perfect attenuated single photon state.

There are two primary ways to generate single photons, collecting emission from a single two level system or producing photons in pairs and detecting one photon to herald the other. In this thesis we discuss the latter process in two different physical systems, four-wave mixing in microstructure optical fiber in chapter 5 and Raman transitions in an atomic ensemble with quantum memory in chapter 3. For

any real application, there are requirements on the properties of a single photon source including photon rate, heralding efficiency, spectral and temporal shape, indistinguishability, and multi-photon emission. For a comprehensive review of single photon sources and their properties see [17].

## 2.4 Characterizing light

### 2.4.1 Heralded single photon sources

Rather than reducing the photon number fluctuations of a single field, for instance by interacting with a single emitter, it is often easier to reduce the fluctuations in the number difference between two fields. Many systems produce photons in pairs such that the members of the pair can be separated into two arms by differences in emission direction, emission time, frequency, or polarization. Even though the number of pairs may fluctuate (often with thermal statistics, as we will see), there are always the same number of photons in the two arms of the source. At low mean photon number, such a system can be used as a heralded single photon source. At high mean photon number such a system is typically referred to as two-mode squeezed because noise on the amplitude difference of the two fields is reduced below the standard quantum limit [43].

A perfect single photon source exhibits  $g^{(k)} = 0$  as there is never more than one photon present in the field (we drop the time argument in the correlation functions, which is zero throughout this section, for simplicity). Typical heralded single photon sources are based on physical systems that produce pairs with a classical number

distribution. We denote the statistics of pair production, and thus the unconditional statistics of either arm, with  $p_{\text{unc}}(n)$  and  $g_{\text{unc}}^{(2)}$ . In general, either arm of the pair source, unconditioned by detection in the other arm, exhibits Poissonian or super-Poissonian statistics that do not violate the classical Cauchy-Schwarz inequality ( $g_{\text{unc}}^{(2)} \geq 1$ ). We can measure the conditional statistics ( $g_{\text{cond}}^{(2)}$ ) of one arm (the signal arm) by only considering pulses or time bins during which a photon is detected in the other arm (heralding arm). This conditioning suppresses the instances in which there is no photon in the signal field, increasing the effective mean photon number of the signal field. However, since the conditioning does not substantially alter the relative probabilities of the non-zero number states, the conditional normalized correlation  $g_{\text{cond}}^{(2)}$  can be extremely small (for weak fields  $g^{(2)} \approx 2p(2)/p(1)^2$  so increasing  $p(1)$  while maintaining  $p(2)/p(1)$  decreases  $g^{(2)}$ ). We see below that in the regime of a weak pair source ( $p_{\text{unc}}(1) \ll 1$ ) we can achieve  $g_{\text{cond}}^{(2)}$  approaching zero.

We can calculate directly how heralding alters the statistics of the signal field. We note that while losses in either arm reduce the overall rate of photons, only losses in the heralding arm reduce the multi-photon suppression and increase  $g^{(2)}$ . This is because  $g^{(2)}$  is insensitive to loss in the field being measured, and thus insensitive to loss in the signal arm. We can calculate the  $g_{\text{cond}}^{(2)}$  expected for a heralded source with arbitrary, but known, statistics of pair production and noise in the heralding and signal fields and loss in the heralding arm. We denote the statistics of pair production, heralding field noise, and signal field noise as  $p_p$ ,  $p_h$ ,  $p_s$  respectively and use the same subscripts for  $g^{(2)}$  and  $\mu$  as well. We also define the quantity  $E(n)$  as the probability of getting a heralding click given  $n$  incident heralding photons.

We can write general expressions for the conditional photon statistics and  $g_{\text{cond}}^{(2)}$ :

$$\begin{aligned}
p_{\text{cond}}(n) &= \frac{\sum_{i,j} p_p(i) p_s(n-i) p_h(j) E(i+j)}{\sum_{i,j} p_p(i) p_h(j) E(i+j)} \\
g_{\text{cond}}^{(2)} &= \frac{\left( \sum_{i,j,k} p_p(i) p_h(j) p_s(k) (i+k)(i+k-1) E(i+j) \right) \left( \sum_{i,j} p_p(i) p_h(j) E(i+j) \right)}{\left( \sum_{i,j,k} p_p(i) p_h(j) p_s(k) (i+k) E(i+j) \right)^2} \\
&= \frac{\left( \sum_{i,j} p_p(i) p_h(j) \left( i(i-1) + 2i\mu_s + \mu_s^2 g_s^{(2)} \right) E(i+j) \right) \left( \sum_{i,j} p_p(i) p_h(j) E(i+j) \right)}{\left( \sum_{i,j} p_p(i) p_h(j) (i + \mu_s) E(i+j) \right)^2}.
\end{aligned} \tag{2.20}$$

These expressions are general and can be used for any implementation of a heralded single photon source. We apply them to the most common case, single photon counting in the heralding arm (with collection efficiency  $\eta$ ) and mean photon numbers much less than one. Under these assumptions we obtain:

$$\begin{aligned}
g_{\text{cond}}^{(2)} &= (\mu_p + \mu_h) (2 - \eta) g_p^{(2)} + 2\mu_s \left( 1 + \frac{\mu_h}{\mu_p} \right) \\
g_{\text{cond}}^{(2)} &= \mu_{\text{unc}} (2 - \eta) g_{\text{unc}}^{(2)} \text{ for } \mu_h = \mu_s = 0.
\end{aligned} \tag{2.21}$$

The conditional intensity auto-correlation function is approximately the unconditional correlation function scaled by the mean number of pairs produced (which we assumed was much less than one).  $g_{\text{cond}}^{(2)}$  is increased by any loss in the heralding arm ( $\eta < 1$ ) or noise in either arm ( $\mu_h, \mu_s \neq 0$ ). In the limit of no noise, we find that  $g_{\text{cond}}^{(2)}$  approaches zero as the pair production approaches zero. Thus we can obtain significant suppression of multi-photon states over the unconditioned field. However, reducing the rate of pair production also reduces the singles rate (the real time rate of photons in the signal field), often an important metric for characterizing

a single photons source.

This analysis also makes clear the impact of unpaired emission in either arm on  $g_{\text{cond}}^{(2)}$ . It is extremely important for obtaining a pure source of heralded single photons to minimize the unpaired photons collected from a pair source. We discuss in the next section a method for reconstructing the underlying modes of a light field, which can be used to improve the mode-matching in collection from pair sources, reducing unpaired photons.

We can see graphically how the photon number distribution of one arm of a pair source is altered by heralding and varies depending the losses in the system. For all of the processes we discuss in this thesis, including four wave mixing in optical fiber, parametric down conversion in nonlinear crystal, and Raman scattering in atomic ensembles, each mode of pair production exhibits thermal number statistics with  $g_p^{(2)} = 2$  so we use these pair statistics in this example [40, 41]. We look at the conditional photon number distribution in four cases, all assuming no noise. The four different assumptions are no heralding (Fig. 2.2a), heralding with perfect efficiency in both arms (Fig. 2.2b), and heralding with reduced ( $\eta=20\%$ ) efficiency in each of the arms (Fig. 2.2cd).

Using photon pair sources to generate heralded single photons has been the primary method for obtaining single photons for a number of years, even though there is a trade off between the real time rate of photons and the multi-photon suppression [17]. We can make some progress overcoming this trade-off between single photon purity and rate by using a multiplexed or photon number resolving detector in the heralding arm. With such a detection scheme we are able to throw

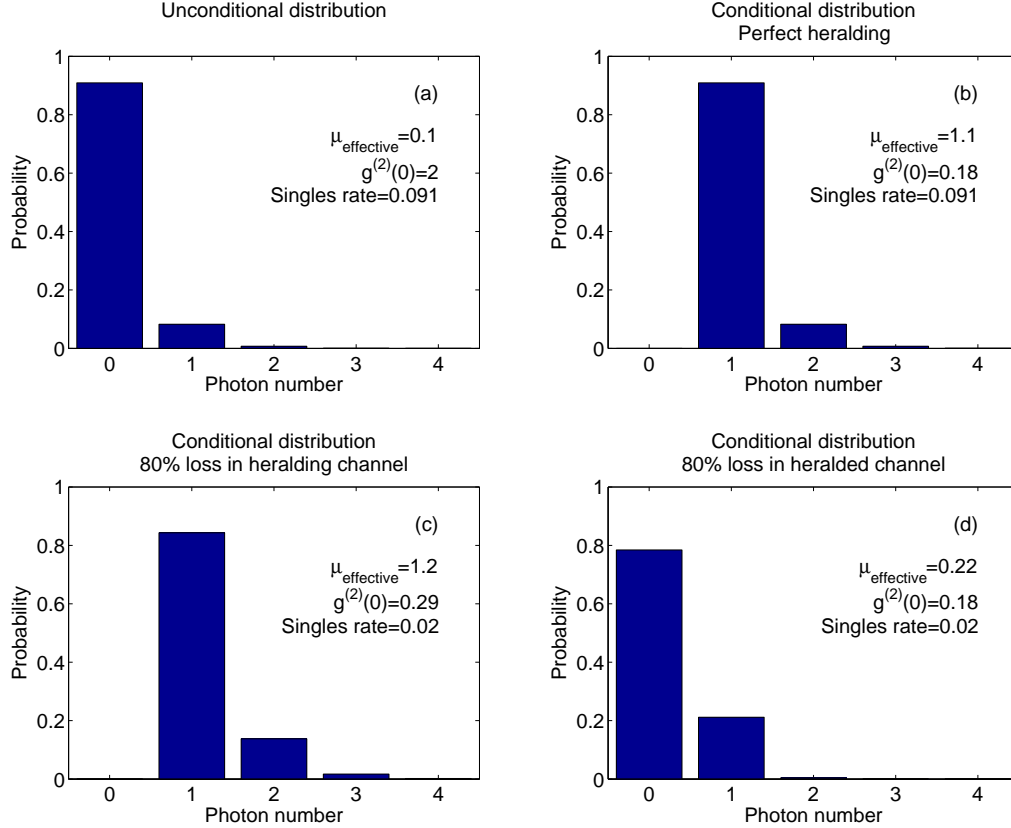


Figure 2.2: (a): Unconditional number distribution of one arm of a pair source with. (b-d): Conditional photon number distribution of one arm of a pair source with (b) no loss, (c) loss only in the heralding field, and (d) loss only in the heralded field.  $\mu_{\text{effective}}$  is the conditional mean photon number and the singles rate is the unconditional rate of photo-detection events.

away time bins containing higher order photon numbers in addition to time bins that contain no photons, thus potentially engineering a source with a high rate of pure single photons. In this case we do not want to make the assumption of a weak field and must go back to eq. 2.20. We can make some progress by assuming thermal number statistics ( $g_p^{(2)} = 2$ ) for the pair source and no noise in either arm. For a photon number resolving detector in the heralding arm with transmission  $\eta$  we find

that

$$g_{\text{cond}}^{(2)} = \frac{2\mu_p(1-\eta)(2+\mu_p(3-\eta))}{(1+\mu_p(2-\eta))^2} \quad (2.22)$$

$$g_{\text{cond}}^{(2)} \approx \frac{4\mu_p(1-\eta)}{1+\mu_p} \text{ for } 1-\eta \ll 1.$$

For perfect efficiency, this goes all the way to zero for any pair rate. However, as the efficiency  $\eta$  drops from unity we see a non-zero multi-photon component in the signal field, though  $g_{\text{cond}}^{(2)}$  is smaller with a number resolving heralding detector than without.

## 2.4.2 Cross-correlation

In addition to being the basis for many single photon sources, photon pair sources are useful in quantum information for the non-classical correlations they exhibit [43, 52]. We can go through a similar process to write the cross-correlation between the two arms in terms of the statistics of the pair production and unpaired photon production in the arms. In this case, we may be interested in fields that are not operated in the weak pair regime. In fact, whereas the conditional auto-correlation only violates the classical Cauchy-Schwarz inequality for a weak pair source (assuming single photon counters in the heralding arm) the cross-correlation can violate the classical Cauchy-Schwarz inequality for any mean photon number, though we will see that the violation becomes smaller for brighter sources. Pair sources are often characterized in terms of the degree of squeezing they exhibit, rather than the degree of correlation. The quantum noise on the intensity difference



of the two arms can be below the standard quantum limit (squeezed), however these two hallmarks of nonclassicality, squeezing and violation of the Cauchy-Schwarz inequality, are not equivalent [53].

We assume a source with two arms,  $a$  and  $b$  (collection efficiencies  $\eta_a$  and  $\eta_b$ ), that produces photons in pairs (with underlying statistical properties  $p_{\text{pairs}}(n)$ ,  $\mu_{\text{pairs}}$ ,  $g_{\text{pairs}}^{(2)}$ ) as well as unpaired photons in each arm ( $p_a(n)$ ,  $\mu_a$ ,  $g_a^{(2)}$  and  $p_b(n)$ ,  $\mu_b$ ,  $g_b^{(2)}$ ). We can write the auto-correlation of each arm as well as the cross-correlation between the two arms in terms of the statistics of the three underlying processes. We define  $p(n_1, n_2)$  as the probability of collecting  $n_1$  photons in arm  $a$  and  $n_2$  photons in arm  $b$ , which is straightforward to write down in terms of  $p_{\text{pairs}}(n)$ ,  $p_a(n)$ ,  $p_b(n)$ ,  $\eta_a$ , and  $\eta_b$  with the appropriate binomial factors. We write the auto-correlation only for arm  $a$  but we note that it is fully symmetric for arm  $b$ .

$$\begin{aligned}
p(n_1, n_2) &= \\
\sum_{i,j,k} p_a(i)p_b(j)p_{\text{pairs}}(k)\eta_a^{n_1}\eta_b^{n_2}(1-\eta_a)^{i+k-n_1}(1-\eta_b)^{j+k-n_2} \binom{i+k}{n_1} \binom{j+k}{n_2} \\
g_{\text{auto}}^{(2)} &= \frac{\langle \hat{n}_a \hat{n}_a \rangle}{\langle \hat{n}_a \rangle^2} = \frac{\sum_{n_1, n_2} n_1(n_1-1)p(n_1, n_2)}{\left(\sum_{n_1, n_2} n_1 p(n_1, n_2)\right)^2} \\
&= 1 + \frac{\mu_{\text{pairs}}^2 \left(g_{\text{pairs}}^{(2)} - 1\right) + \mu_a^2 \left(g_a^{(2)} - 1\right)}{(\mu_{\text{pairs}} + \mu_a)^2} \\
g_{\text{cross}}^{(2)} &= \frac{\langle \hat{n}_a \hat{n}_b \rangle}{\langle \hat{n}_a \rangle \langle \hat{n}_b \rangle} = \frac{\sum_{n_1, n_2} n_1 n_2 p(n_1, n_2)}{\left(\sum_{n_1, n_2} n_1 p(n_1, n_2)\right) \left(\sum_{n_1, n_2} n_2 p(n_1, n_2)\right)} \\
&= 1 + \frac{\mu_{\text{pairs}}^2 \left(g_{\text{pairs}}^{(2)} - 1\right) + \mu_{\text{pairs}}}{(\mu_{\text{pairs}} + \mu_a)(\mu_{\text{pairs}} + \mu_b)}
\end{aligned} \tag{2.23}$$

We see that the auto correlation has the form of a weighted average of the auto-

correlations of the paired and unpaired emission in that arm. The statistics of pair production and of any noise processes in the system are typically classical ( $g^{(2)} \geq 1$ ), which means the cross-correlation is greater than the uncorrelated limit of unity for any amount of pair production and equal to one for no pair production.

In the case of no unpaired photons ( $\mu_a = \mu_b = 0$ ) this system clearly violates the classical Cauchy-Schwarz inequality ( $g_{\text{cross}}^{(2)} \leq \sqrt{g_{\text{auto},a}^{(2)} g_{\text{auto},b}^{(2)}}$ ), though the violation falls off as  $1/\mu_{\text{pairs}}$ :

$$g_{\text{cross}}^{(2)} = g_{\text{pairs}}^{(2)} + \frac{1}{\mu_{\text{pairs}}} \tag{2.24}$$

$$g_{\text{auto}}^{(2)} = g_{\text{pairs}}^{(2)}$$

In the presence of unpaired photons the system may or may not violate the classical Cauchy-Schwarz inequality depending on the fraction of light that is paired, the overall rate of pairs, and the statistics of the processes. We revisit this analysis in chapter 3 in the context of an atomic ensemble-based pair source.

### 2.4.3 Mode reconstruction

Characterizing the underlying mode spectrum of a light field has wide ranging applications throughout physics. For instance, knowledge of the mode structure is vital for engineering sources of nonclassical light that minimize loss and decoherence of quantum information due to coupling to unwanted modes. Such applications include mode-matching biphoton collection [54], producing factorizable states of photon pairs [23], minimizing classical background emission from single-emitter

sources [55], and characterizing the number and degree of squeezing in multimode continuous variable entangled states [52, 54, 56–59]. Also, full mode reconstruction allows a more subtle distinction between classical and nonclassical fields. We show how a full reconstruction of the underlying mode structure of a field can provide information about nonclassical components of a nominally classical field [25].

First- and second-order photon-number statistics are used to characterize a variety of optical systems including single-photon sources [60–62], photon pair sources [18, 63, 64], cavity quantum electrodynamics [65, 66], and lasers [67, 68]. However, in terms of understanding the underlying processes contributing to the light field, one- and two-fold photodetection can provide only limited information. Recent developments in photon number resolving (PNR) detectors [37, 69–71] allow simpler measurement of higher-order correlations, and such measurements should continue to become more routine [72–74]. We show that this additional information can allow a full characterization of the various quantum and classical modes present in a light field.

Typically, full characterization of the mode structure involves a series of separate measurements in spatial, temporal, frequency, and polarization domains, requiring a range of instrumentation. However, our method can be easily integrated into existing optical systems as it uses only a single measurement of the photon number distribution of a field. We consider multimode light from a single source, such as multimode thermal light from spontaneous parametric down conversion (SPDC), as well as from multiple sources, each producing light in one or more modes, such as attenuated single photons from a single emitter and coherent light from a laser.

We note, however, that this method is extremely general and can be used for any combination of sources, though only the total fraction of the power with underlying Poissonian statistics can be determined. We also theoretically study the robustness and prospects of our method in experimentally accessible regimes.

It is straightforward to write down the full photon-number probability distribution for a given mode structure with mean photon numbers  $\mu_i$  in the modes. For thermal and Poissonian statistics  $\mu = \langle n \rangle$  is the mean photon number and for attenuated single-photon statistics  $\mu$  is the probability of finding a single photon. The photon number probability distribution is uniquely described by a probability generating function  $G(s)$  with  $g^{(k)} = G^{(k)}(s = 1) / (\mu_{\text{total}})^k$ , where  $G^{(k)}(s = 1)$  is the  $k^{\text{th}}$  derivative of  $G(s)$  evaluated at  $s = 1$ . The generating function for a multi-mode field is the product of the generating functions for all the underlying modes. For the statistical distributions we consider here  $G_{\text{thermal}}(s) = (1 + \mu(1 - s))^{-1}$ ,  $G_{\text{single photon}}(s) = (1 - \mu(1 - s))$ , and  $G_{\text{Poissonian}}(s) = e^{-\mu(1-s)}$  [41]. For any other mode with arbitrary photon number statistics we could write down a generating function and use the same method.

This gives us a set of non-linear relations between the  $g^{(k)}$  and the  $\mu_i$ . By measuring the photon number statistics (which gives us the  $g^{(k)}$ ) we can find the full mode distribution in the form of a set of  $\mu_i$ . For the mixed states considered here,  $N$  orders of correlation functions are required to fully determine the mode occupation for light with contributions from  $N$  modes. For  $\mu_{\text{total}} \ll k$ , photon number resolution up to  $k$  photons is required to accurately measure  $g^{(k)}$  (recall that  $g^{(k)}$  is loss-insensitive, so we can always attenuate the light until  $\mu_{\text{total}} \ll k$  for

any  $k$ ). Overdetermining the system, by using more than  $N$  correlation functions to reconstruct  $N$  modes, can improve the accuracy of reconstruction. It is important to note that we must guess what types of modes could be contributing to the field, though we see in chapter 5 that there is no penalty for assuming potential modes that are not, in fact, present.

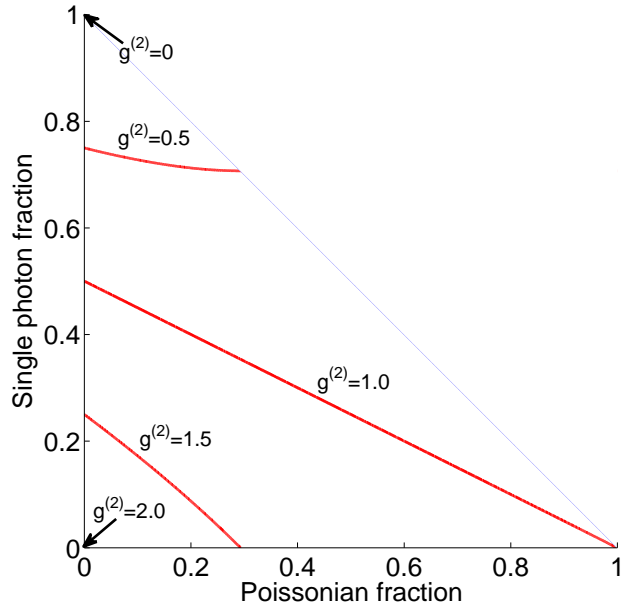


Figure 2.3: Example case of one thermal mode, one single photon mode, one Poissonian mode and fixed  $\mu_{\text{total}}$ . Lines of constant  $g^{(2)}$  are drawn for  $g^{(2)} = 0.5, 1.0, 1.5$  and the corners of the figure where  $g^{(2)}$  reaches its extreme values of 0 and 2 are noted.

As an example, we consider a field that is a mixed state with contributions from one thermal mode, one single-photon mode, one Poissonian mode and a fixed  $\mu_{\text{total}}$ . By varying the fraction of power contributed by each mode, such a mixed state can exhibit  $g^{(2)}$  between 0 (all single photon) and 2 (all thermal). For any  $g^{(2)}$  between these extremes, there is a family of possible mode distributions. Figure 2.3 shows lines of constant  $g^{(2)}$  as a function of the fraction of light from the Poissonian

and single photon modes. The corners of the figure where  $g^{(2)}$  reaches its extreme values of 0 (all single photon) and 2 (all thermal) are noted. In order to determine the actual mode distribution of a given mixture of these three modes we clearly require more information. Figure 2.4 adds lines of constant  $g^{(3)}$  that intersect the

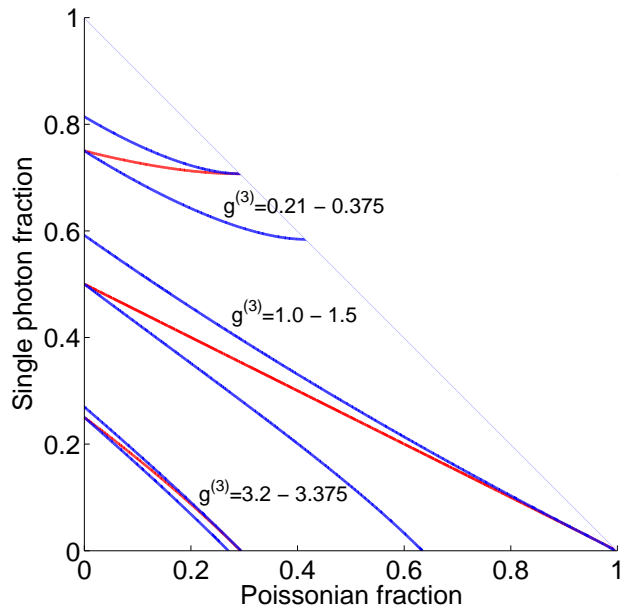


Figure 2.4: Example case of one thermal mode, one single photon mode, one Poissonian mode and fixed  $\mu_{\text{total}}$ . We have added lines of constant  $g^{(3)}$  that intersect the lines of constant  $g^{(2)}$  at their extrema. Noted are the range of values of  $g^{(3)}$  that a field with that  $g^{(2)}$  can take.

lines of constant  $g^{(2)}$  at their extrema. We note on the figure the range of values of  $g^{(3)}$  that a field with that  $g^{(2)}$  can take. Together,  $g^{(2)}$  and  $g^{(3)}$  intersect at a single point in the parameter space and uniquely identify any mixture of three modes (with fixed total mean photon number). For a field with more underlying modes, we would require additional orders of the correlation function for each additional mode.

Including additional orders of correlations (more  $g^{(k)}$  than the number of modes in the field) will further distinguish different sets of modes. We study the expected

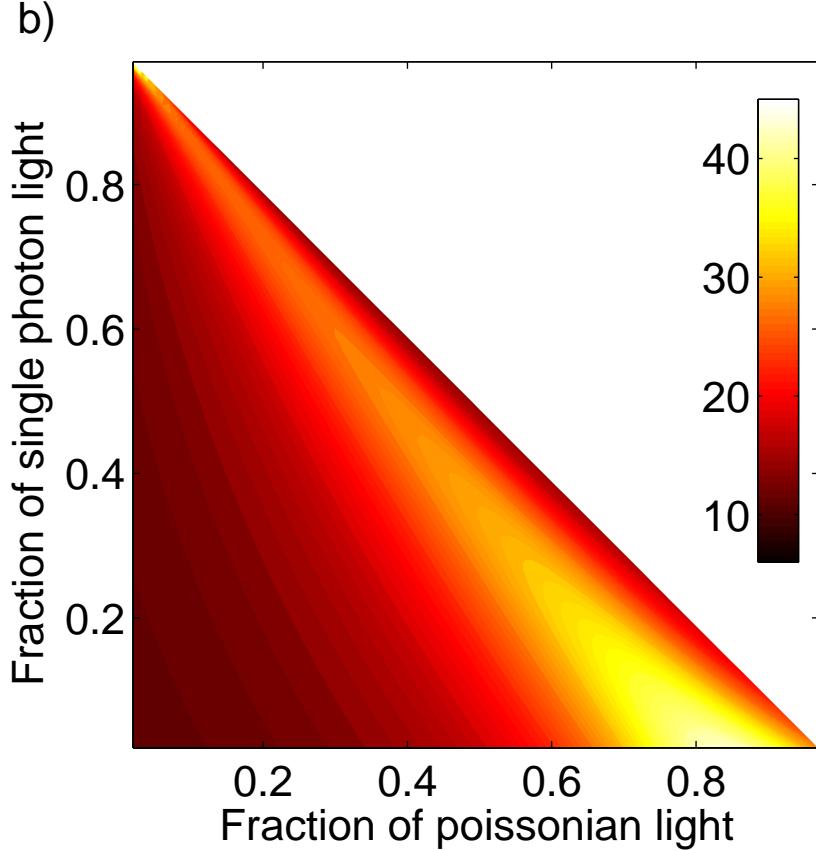


Figure 2.5: Sensitivity gained by using an overdetermined set of six correlation functions compared to three for an example case of one thermal mode, one single photon mode, one Poissonian mode and fixed  $\mu_{\text{total}}$ . Color represents the ratio of the figure of merit for six- to three-fold detection at each point in the space. Figure of merit is a function of the gradients of the correlation functions,  $\sum_k (\nabla_{\vec{\mu}} g^{(k)}[\vec{\mu}] / g^{(k)}[\vec{\mu}])^2$ , where  $\vec{\mu}$  is the set of  $\mu_i$ .

improvement gained by using higher order correlations in terms of the sensitivity of the photon number distribution to the mode structure. The particular figure of merit we consider is a function of the gradients of the correlation functions,  $\sum_k (\nabla_{\vec{\mu}} g^{(k)}[\vec{\mu}] / g^{(k)}[\vec{\mu}])^2$ , where  $\vec{\mu}$  is the set of  $\mu_i$ . In Fig. 2.5 we show the ratio of this figure of merit using six orders of the correlation function compared to three. We see a gain in sensitivity for all mode configurations and the gain is largest near the fully Poissonian configuration. Higher order photon number resolution, up to

ten photons or more, is becoming possible with new PNR detectors. With such detectors, one can trade off including additional modes in the reconstruction for increasing the fidelity of reconstruction. We describe in chapter 5 an experimental demonstration of this reconstruction method.



## Chapter 3: Quantum optics in rare-earth systems

Most quantum information protocols are based on interactions between light and matter. In particular, atoms with narrow optical transitions and long-lived microwave or rf transitions are excellent candidates for processing and storing quantum information [28, 75]. A common way to achieve strong coupling between atoms and light is to use an optically dense ensemble of atoms in which a single photon is likely to interact with the atomic system during a single pass through the ensemble. This approach is typically technically simpler than the alternative of coupling a single atom to an optical cavity that ensures a single photon has many chances to interact with the single atom. The quantum information stored in the ensemble is generally stored in collective atomic states in which the information is spread among all the atoms in the ensemble. As a result dephasing, decoherence, or loss of any single atom reduces the fidelity of the full state by only a small amount. Atomic ensembles have become a workhorse platform throughout quantum optics for quantum memory, quantum information processing, generation of non-classical light, and many more applications.

Gases of alkali atoms have been the primary systems for quantum optics in atomic ensembles to date. However, there is much interest in finding a solid state al-

ternative that can be integrated with existing solid state infrastructure and devices. In addition, in order to achieve second-scale coherence times, which are required for long-lived quantum memory, alkali atoms must be cooled and loaded into optical lattices, which has a large experimental overhead cost [76]. Rare-earth ion-doped crystals (REIC) are solid state materials containing a “frozen gas” of rare-earth ions with narrow optical transitions (at liquid helium temperatures) and rf transitions with demonstrated coherence times of many seconds, which makes them promising candidates for quantum information applications [77]. In this chapter we will discuss the properties of REIC, the challenges of working with these systems, the state of the art of the field, and finally we report experimental progress toward implementing quantum memory in a REIC, praseodymium doped yttrium orthosilicate ( $\text{Pr}^{3+}:\text{Y}_2\text{SiO}_5$ ).

### 3.1 Basic properties

The rare-earth elements, or lanthanides, are the elements from atomic number 57 (lanthanum) to atomic number 71 (lutetium). These elements are used in a wide variety of applications from lasers and optical amplifiers to optical data storage and processing. In this chapter we discuss implementing quantum memory in REIC at cryogenic temperatures. The relative insensitivity of rare-earth ions to the surrounding crystal environment results in sharp optical transitions with high spectral densities and long coherence times. For instance, the hyperfine coherence time in  $\text{Pr}^{3+}:\text{Y}_2\text{SiO}_5$  has been measured in excess of 30 s [78], which is among the

longest coherence times observed in a candidate material for quantum memory. Isolation from the surrounding environment and accompanying long coherence times are important to reduce loss of stored quantum information.

The different rare-earth elements have very similar chemical properties. The 3+ oxidation state is the most common, and in this state they have partially filled 4*f* orbitals with electronic configurations [Xe]4*f*<sup>*n*</sup> for *n* = 0 to 14. The electrons in the partially occupied 4*f* shell are shielded from their environment by the full 5*s* and 5*p* shells whose spatial extent extends farther than the 4*f* shell (see Fig. 3.1) [79]. This shielding contributes both to the ions' insensitivity to the crystal environment and the chemical similarity of the different elements.

For quantum memory applications, the important transitions in REIC are within the 4*f* orbital and have optical frequencies in the visible and infrared. For the free ion, electric dipole transitions between 4*f* levels are forbidden due to parity. However, these transitions do occur when the ions are doped in low symmetry crystal hosts, albeit with relatively weak transition strengths [80, 81]. We point out here that there are bright, strongly allowed 4*f* → 5*d* transitions in the ultraviolet, but these processes are outside the scope of this work as they do not have the coherence properties that make the 4*f* → 4*f* transitions of interest for quantum memory [80]. Because of the shielding of the 4*f* electrons, the crystal field can be treated as a perturbation to the free ion energy levels. The free ion energy levels are determined mainly by the coulomb and spin-orbit interactions. The spin-orbit interaction mixes states with different orbital angular momentum *L* and spin *S* (maintaining total *J*). The resulting (2*J* + 1)-degenerate energy manifolds are labeled according to *J* and

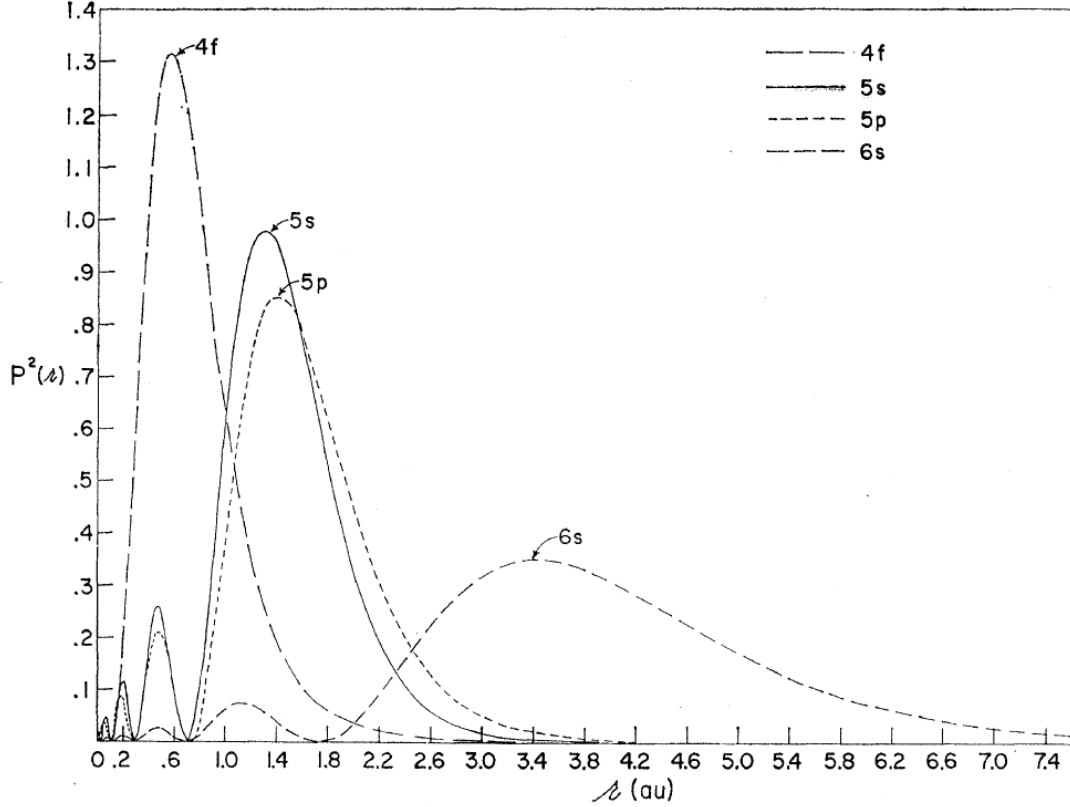


Figure 3.1: Hartree-Fock calculation of the radial charge densities for the  $4f$ ,  $5s$ ,  $5p$ , and  $6s$  orbitals for  $\text{Gd}^+$ . The shielding of the  $4f$  shell by the full  $5s$  and  $5p$  shells is common to the rare-earths (the trivalent ions have empty  $6s$  orbitals). From [79].

the dominant  $L$  and  $S$  values with Russell-Sanders notation  $^{2S+1}L_J$ . The crystal field of a low symmetry host fully lifts this  $2J + 1$  degeneracy for ions with an even number of electrons (non-Kramers ions) such as  $\text{Pr}^{3+}:\text{Y}_2\text{SiO}_5$  [80]. For ions with an odd number of electrons (Kramers ions) the  $2J + 1$  degenerate manifolds are split into at most a set of doublets. Figure 3.2 shows the rare-earth energy levels in the crystal host  $\text{LaCl}_3$  where the width of the line represents the splitting due to the crystal field. These energy level structures are similar for other low symmetry hosts such as  $\text{Y}_2\text{SiO}_5$  [82].

We are interested in the transition between the lowest energy, zero angular

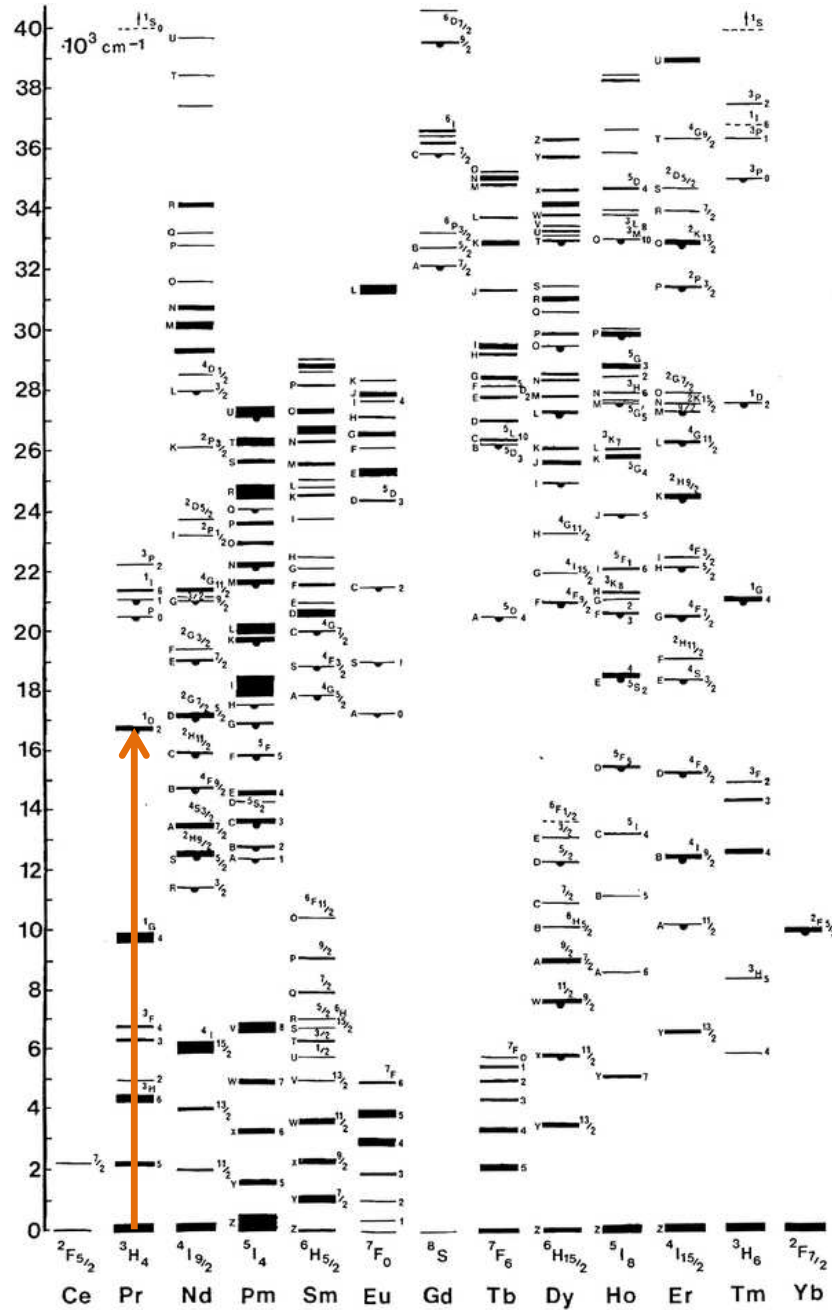


Figure 3.2: Dieke diagram of the rare-earth energy levels in the crystal host  $\text{LaCl}_3$ . The width of the line represents the splitting due to the crystal field. Energy levels are qualitatively similar in other low-symmetry hosts. From [82]. The  ${}^3H_4 \rightarrow {}^1D_2$  transition in praseodymium is highlighted.

momentum levels of the  ${}^3H_4$  and  ${}^1D_2$  manifolds in  $\text{Pr}^{3+}:\text{Y}_2\text{SiO}_5$  at 605.977 nm ( $16502 \text{ cm}^{-1}$ ). Praseodymium has one naturally occurring stable isotope ( ${}^{141}\text{Pr}$ )

with nuclear spin  $5/2$ . The hyperfine structure of the ground and excited manifolds is determined by the hyperfine, nuclear quadrupole, electronic Zeeman, and nuclear Zeeman interactions, which are many orders of magnitude smaller than the free ion and crystal field interactions [83]. In zero magnetic field, the ground and excited levels split into 3 doubly degenerate states, which we label with the nuclear quantum numbers, though these states are highly mixed and far from angular momentum eigenstates. The hyperfine structure (in zero magnetic field) is shown in fig. 3.3. All nine transitions between these two manifolds are allowed with known transition strengths [83]. In  $\text{Pr}^{3+}:\text{Y}_2\text{SiO}_5$  at liquid helium temperatures (4 K), the lifetime ( $T_1$ ) of the optical transition is  $\approx 160 \mu\text{s}$  and the coherence time ( $T_2$ ) of the optical transition is  $\approx 150 \mu\text{s}$  with the extra non-radiative decoherence ( $T_2 < 2T_1$ ) resulting from nuclear spin fluctuations in the crystal host [84]. The ground hyperfine transitions exhibit lifetimes of  $\approx 100 \text{ s}$  though the coherence time is only  $\approx 500 \mu\text{s}$  [85]. However, this coherence time has been extended to nearly 1 s with a static magnetic field [86] and to tens of seconds with dynamic decoherence techniques [33, 34].

Many different REIC systems have been used to date in quantum optics schemes. As of this writing, we are aware of experimental schemes using praseodymium, neodymium, europium, erbium, and thulium systems. Typically Kramer's ions are avoided because large magnetic fields are needed to lift the  $J$  degeneracy. Erbium and neodymium are the only Kramer's ions on the above list. Erbium is of particular interest because of its telecommunications band transition wavelength. In addition to low site symmetry, typical hosts have small nuclear magnetic moments as nuclear spin flips in the host are a primary source of decoherence

Hyperfine structure of  $\text{Pr}^{3+}:\text{Y}_2\text{SiO}_5$

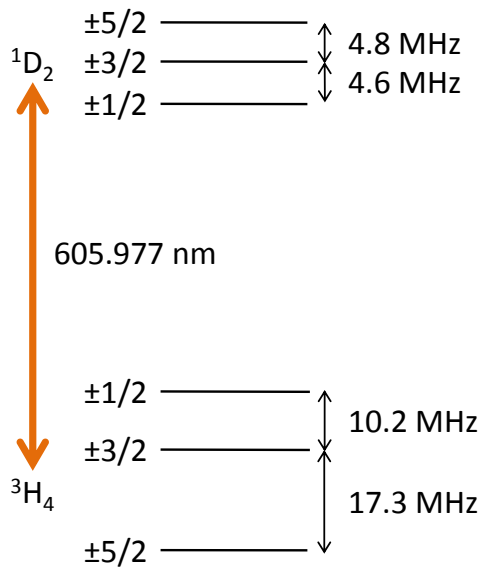


Figure 3.3: Hyperfine structure of the lowest-to-lowest  ${}^3H_4 \rightarrow {}^1D_2$  transition in  $\text{Pr}^{3+}:\text{Y}_2\text{SiO}_5$ . Levels are labeled with nuclear quantum numbers, however there are no true good quantum numbers for these states and all ground to excited transitions are allowed with various transition strengths for linearly polarized light [81].

for the rare-earth ion dopants. For an extensive review of quantum optics in REIC see [77].

### 3.2 Spectral hole burning

A major challenge of working with REIC is the substantial inhomogeneous broadening of the optical transition. Crystal field variations and ion-ion interactions result in variation of the optical transition frequencies of different dopant ions. The inhomogeneous width (typically 1-100 GHz in  $\text{Pr}^{3+}:\text{Y}_2\text{SiO}_5$ ) depends on the doping concentration. In all REIC systems used in quantum optics schemes to date, the inhomogeneous broadening is larger than the hyperfine splitting and prevents resolution of this splitting without special state preparation discussed below. Work toward growing REIC with reduced inhomogeneous broadening is ongoing and would be a major boon to implementing quantum information protocols in these materials [77, 87].

We think of this broadening as a spectrum of homogeneously broadened lines for the many frequency classes of ions present in the system (see fig. 3.4). At 4 K, the homogeneous linewidth of the optical transition can be very narrow ( $< 1$  kHz in  $\text{Pr}^{3+}:\text{Y}_2\text{SiO}_5$ ) and there are a million or more lines in the broadened profile [84]. This broad absorption feature can be shaped via a process called spectral hole burning. In REIC, the large ratio of the hyperfine state lifetime to the optical state lifetime ( $10^6$  or more) and the non-zero matrix elements of most ground  $\rightarrow$  excited transitions allow optical pumping with narrowband laser fields. In particular, a laser applied



somewhere in the inhomogeneous profile will pump ions out of states resonant at the laser frequency and into “dark” ground states that are not resonant. This opens up a transparent spectral region, or hole, that persists for the ground state lifetime of the system (see fig. 3.4). In general, the absorption spectrum in the region around the hole burning laser frequency will exhibit a set of side holes and anti-holes, regions of lower and higher absorption respectively, whose positions and depths depend on the hyperfine splittings and transition matrix elements of the particular system (not shown in fig. 3.4).

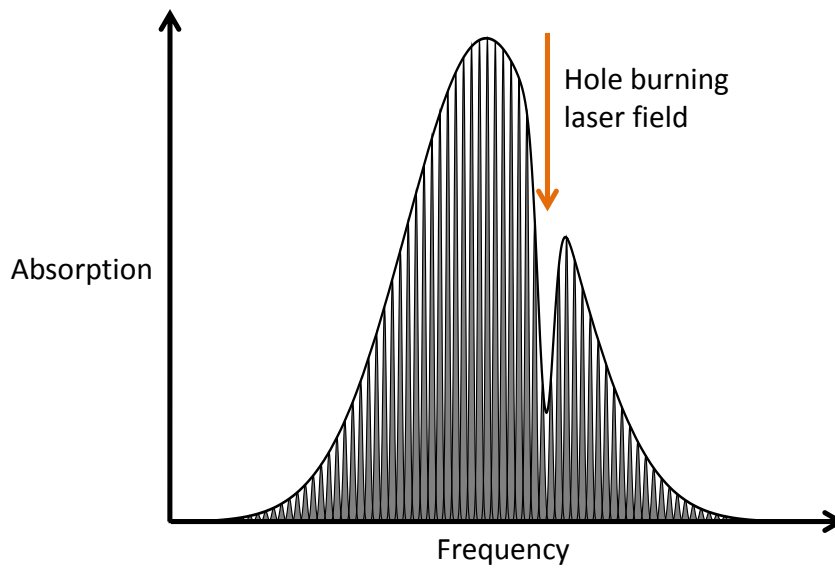


Figure 3.4: The inhomogeneous broadening in REIC can be thought of as a series of homogeneous lines. Applying a laser field somewhere in the inhomogeneous profile optically pumps ions into states that are not resonant with the laser, opening up a transparent window at the laser frequency.

The absorption profile can be shaped arbitrarily via spectral hole-burning by appropriately modulating the frequency and amplitude of the hole-burning laser field or fields (with limits on maximum and minimum hole width set by the hyper-

fine level structure, laser linewidth, and homogenous optical linewidth). One such scheme that is important for many quantum information applications is isolating a narrow frequency class of ions in order to optically address a particular ground hyperfine transition. Such isolation is necessary to take advantage of the seconds-scale coherence times of the ground states for quantum storage. This requires a spectral hole-burning procedure that empties a wide spectral region around the optical transitions involving the two ground states of interest and populates one ground state in a narrow spectral region. The result of such a procedure is to obtain an ensemble of ions with a  $\Lambda$ -type energy level scheme, two ground states that can be optically coupled to an excited state, initialized into one of the ground states.

A particular implementation of such a scheme modified from [81] is shown in Fig. 3.5 for a system such as  $\text{Pr}^{3+}:\text{Y}_2\text{SiO}_5$  with three ground and three excited states. The result is a narrow absorbing feature of atoms in a particular ground state on a background emptied of absorbers in the surrounding spectral region. At least one additional auxiliary ground state must be present in the system to hold the population in the spectral region around the narrow feature. And it is important to note that the width of the transparent region surrounding the narrow feature is limited by the hyperfine structure of the system.

In this hole-burning sequence, two fields that are either spectrally broadened or swept back and forth in frequency burn out spectral trenches around the transitions from the upper two ground states to the lower two excited states, while a narrow field connects the lowest ground state to the upper state manifold. Together these fields select one particular frequency class of ions that has no dark ground state,

ions that are resonant with one of the fields in any ground state. The fields pump away all ions in other frequency classes to dark ground states such that they will no longer be excited by any of these fields. We choose the upper two ground states and lower two excited states because in  $\text{Pr}^{3+}:\text{Y}_2\text{SiO}_5$  the four transitions involving these states have similar transition strengths, while the  $\pm 5/2$  ground and excited states couple strongly to each other and weakly on all other optical transitions. Once all ions in other frequency classes are pumped away, one of the broadened fields is turned off so that atoms can populate a narrow region inside that trench. Finally, the narrow field is turned off to ensure that the trench in the second ground state is fully emptied, a step that is not strictly necessary, but we show here because we required this step given the specific hole-burning fields used in our experiment. The width of the feature is in general determined by a combination of the homogeneous linewidth of the transition and the linewidth and intensity of the hole burning laser.

### 3.3 Quantum memory

Photons are excellent carriers of quantum information. However it is often necessary to locally store qubits for tasks including synchronizing operations, performing quantum gates, and generating single photons on demand [28]. In addition, a major application of quantum memory is for quantum repeaters that allow long distance quantum communication over a lossy optical channel [30]. Loss in optical fiber increases exponentially with distance. Unlike classical communication, where we can use bright states and amplifiers to overcome this loss, quantum communica-

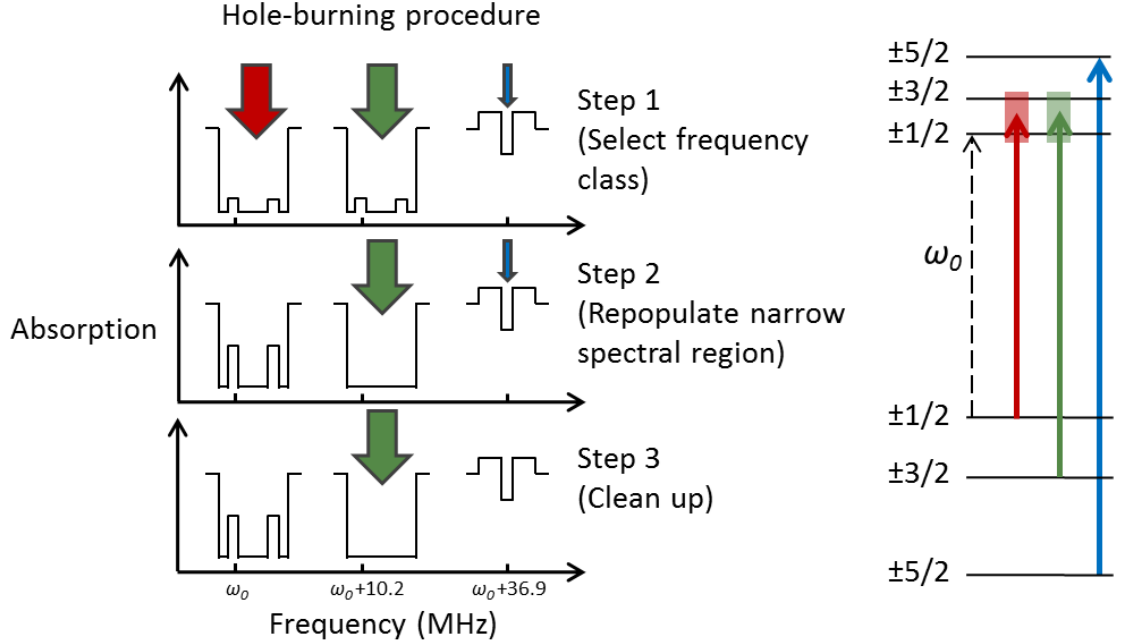


Figure 3.5: Process for generating a narrow absorbing feature in a particular ground state on a background emptied of absorbers while also emptying another ground state. Two fields that are either spectrally broadened or swept back and forth in frequency burn out spectral trenches around the transitions from the upper two ground states to the lower two excited states. Along with a narrow field connecting the lowest ground state to the upper state manifold these fields select a particular frequency class of ions. Ions in other frequency classes will all be pumped to “dark” states by these fields such that they will no longer be excited by any of these fields. In step two, one of the broadened fields is turned off so that atoms can populate a narrow region inside that trench. Finally, the narrow field is turned off to ensure that the trench in the second ground state is fully emptied.

tion requires transmission of single photons (or other similarly loss-intolerant states).

Thus, the loss in optical fiber means that the time to directly transmit quantum information over a fiber link scales exponentially with distance and long-distance communication in this manner is unfeasible. Quantum repeaters overcome this loss and allow quantum communication in a time that scales polynomially, rather than exponentially, with distance. A quantum repeater relies on generating and storing entanglement in quantum memory nodes spaced along the communication channel.

These nodes break the entire communication length into a series of shorter segments. Entanglement is heralded by transmission of single photons over the shorter segments between quantum memory nodes. If a heralding photon is lost in one or more of the segments, entanglement generation only has to be retried on the segments where it failed. The other quantum memory nodes store the entanglement on the segments that succeeded. The beneficial scaling is a result of the fact that unlike with direct communication, in which a single photon must traverse the entire distance, with a quantum repeater, loss in one part of the link does not negate successful transmission in another. Once entanglement is established over the entire channel, quantum teleportation allows transmission of quantum information over the full distance [31].

Simple delay lines or switchable optical cavities can be used as quantum memory to some extent, but they can suffer from high loss for even moderate storage times because the light propagates in lossy optical fiber or undergoes many imperfect reflections off the cavity mirrors. To this end, there has been substantial research into using atomic ensembles as the basis for quantum memories. The strong coupling possible between atomic ensembles and single photons can allow qubits to be read in and out of an ensemble-based quantum memory with high fidelity. In addition, atoms often have rf or microwave spin transitions with coherence times of seconds or longer. The maximum storage time for a quantum memory is set by the coherence time of the qubit transition. It is important to note that in atomic ensembles, dephasing of the qubit will occur on a time scale set by the inhomogeneous broadening of the qubit transition, but this dephasing can be mitigated with dynamic

decoherence control techniques that involve a sequence of rephasing  $\pi$ -pulses on the qubit transition [78,88]. In general a  $\Lambda$ -type energy level system is used to optically manipulate the long-lived spin transition via an excited state, whose coherence time may be substantially shorter than the spin coherence time. REIC have a number of properties that make them promising candidates for quantum memory protocols as solid-state systems with narrow optical transitions and long coherence times.

There are many different physical processes by which light may be stored in an atomic ensemble. Many quantum memory protocols have been demonstrated in rare-earth systems in the last several years [33–35, 89–91]. Many of the quantum memory schemes in REIC are based on photon echo-type techniques in which dephasing due to the inhomogeneous profile of the absorption is rephased, producing a coherent echo of the input light [92]. These protocols have shown great promise, particularly in memory efficiency and fidelity. The rephasing can be due to an initial periodic structure of the inhomogeneous profile as in the atomic frequency comb (AFC) protocol or by switching electric fields to flip the inhomogeneous profile by the dc stark effect as in the gradient echo memory (GEM) and controlled reversible inhomogeneous broadening (CRIB) protocols [35, 89, 90]. In these cases, the light is stored directly in the optical transition of the material, and in order to take advantage of the seconds-scale ground coherence times in REIC the coherence must be transferred to and from another ground state via optical  $\pi$ -pulses. Any deviation from ideal  $\pi$ -pulses will reduce the fidelity of retrieval. In addition, these protocols require hole-burning sequences that generate sharp and narrow absorbing features. Thus, exquisite control over the frequency and intensity of the optical

fields is required.

Another set of quantum memory protocols store the coherence directly on the long-lived ground state via Raman transitions. These include electromagnetically induced transparency (EIT) and rephased amplified spontaneous emission (RASE), which have both been demonstrated in REIC and have shown great promise, particularly in achieving long memory times [33,34,91]. These protocols do not require particularly stringent hole-burning schemes, though the RASE scheme does employ optical  $\pi$ -pulses to transfer coherence between states. Here we describe our work implementing a variation of the scheme introduced in ref. [93] (DLCZ scheme) storing collective excitations directly on a ground state transition via spontaneous Raman transitions, closely related to both EIT and RASE [22]. This protocol involves probabilistically generating and storing, and deterministically retrieving, a single collective excitation directly on the long-lived ground transition. While this process cannot store an arbitrary qubit state, it lends itself directly to the task of building a quantum repeater [93] and does not require precise optical pulses or particularly narrow absorbing features.

### 3.3.1 Experimental methods

We first describe the ideal case for our protocol, and then detail the modifications made to perform our initial demonstration. An ensemble of atoms with a  $\Lambda$ -type energy level scheme is prepared with all atoms in one of the metastable ground states  $|g\rangle$ . A write pulse weakly couples the occupied state  $|g\rangle$  to an ex-

cited state  $|e_w\rangle$  (Fig. 3.6). With small probability, this write field scatters a single atom from state  $|g\rangle$  to state  $|s\rangle$ , accompanied by a single photon detuned from the write field by the  $|g\rangle \rightarrow |s\rangle$  splitting. Detection of this single heralding photon in a particular direction projects the  $N$  atoms in the ensemble into the superposition state:

$$\psi = \sum_{j=1}^N e^{i\Delta\mathbf{k}\cdot\mathbf{r}_j} |g_1 g_2 \cdots s_j \cdots g_N\rangle \quad (3.1)$$

where  $\Delta\mathbf{k}$  is the difference between the wavevectors of the write field and heralding photon  $\Delta\mathbf{k} = \mathbf{k}_{\text{write}} - \mathbf{k}_{\text{heralding}}$  and  $\mathbf{r}_j$  is the position of the  $j^{\text{th}}$  atom. This state evolves coherently for the coherence time of the  $|g\rangle \rightarrow |s\rangle$  transition. We note that if the  $|g\rangle \rightarrow |s\rangle$  transition is inhomogeneously broadened, that broadening sets a dephasing time for the collective excitation, but one or more rephasing  $\pi$ -pulses on the  $|g\rangle \rightarrow |s\rangle$  transition allow storage of the collective excitation for the full coherence time [88]. As long as we have maintained the  $|g\rangle \rightarrow |s\rangle$  coherence, a bright read pulse that couples state  $|s\rangle$  to an excited state  $|e_r\rangle$  will return the single scattered atom to state  $|g\rangle$  and convert the collective excitation into a phase-matched single photon, detuned from the read field by the  $|g\rangle \rightarrow |s\rangle$  splitting. The single retrieved photon will be emitted in a direction set by the  $\mathbf{k}$ -vectors of the write, heralding, and read fields  $\mathbf{k}_{\text{ret}} = \mathbf{k}_{\text{write}} + \mathbf{k}_{\text{read}} - \mathbf{k}_{\text{her}}$ .

This basic process can be used as a source of single photons in a well defined spatial and spectral mode (the retrieved photon). In particular, single photons generated in this way are perfectly suited for use with the atomic system from which they are generated. This is important, as many common single photon sources



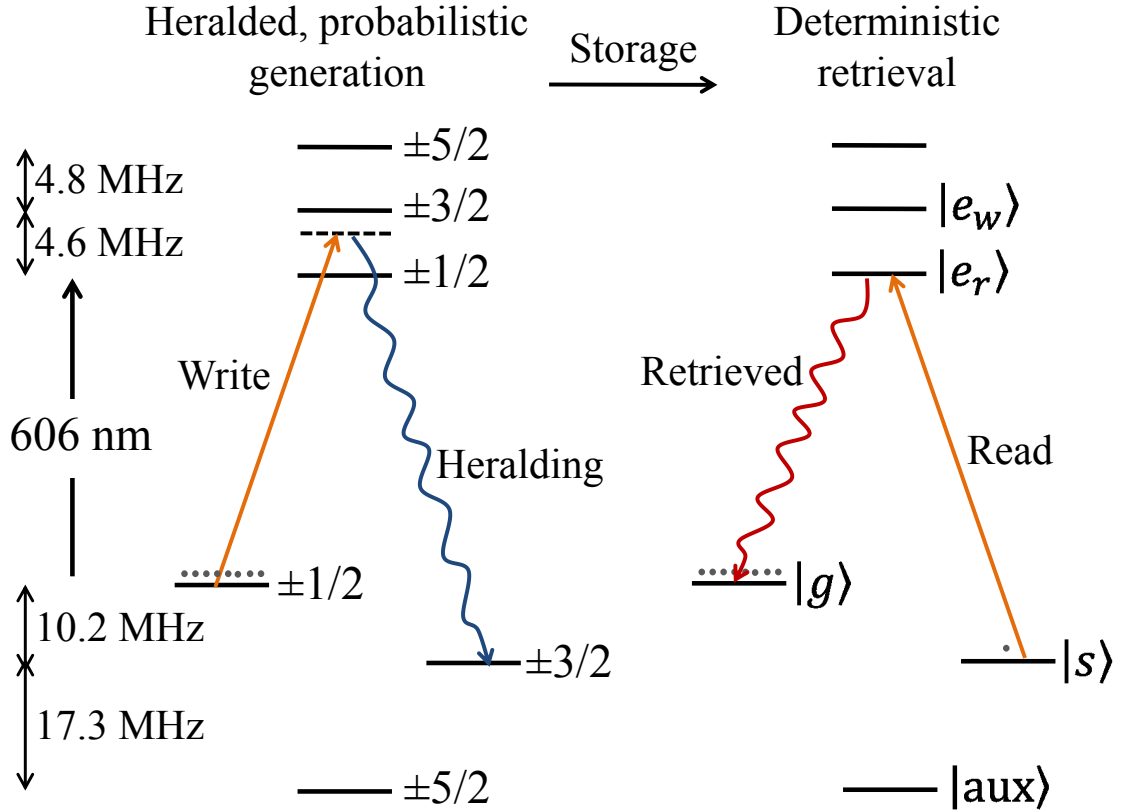


Figure 3.6: Level structure for generation and retrieval of collective excitations in  $\text{Pr}^{3+}:\text{Y}_2\text{SiO}_5$ . Doubly degenerate ground and excited hyperfine states are labeled as are the states of the double- $\Lambda$  system. The third ground state is used as an auxiliary state for unwanted ions during the spectral hole-burning process.

produce single photons with spectral properties that are incompatible with atomic systems. In addition, by sending identical write pulses to identically prepared ensembles and erasing the which-way path information of the heralding photons we can entangle two ensembles in such a way that we have a superposition of a single collective excitation in one ensemble and no excitations in the other and vice-versa. Generating and swapping this entanglement among many ensembles can be used to build up a quantum repeater in which entanglement is distributed over a long distance.

For both of these applications, it is important to limit the probability of generating multiple collective excitations [93]. The excitations, and the corresponding heralding photons, exhibit classical, thermal number statistics. In the limit of weak excitation probability, this means that the probability of a double excitation is the square of the single excitation probability. Thus, suppressing higher order excitations is a matter of reducing the rate of single excitations. Typically, the write pulse is detuned from the  $|g\rangle \rightarrow |e\rangle$  transition to reduce the probability of generating multiple excitations at the expense of reducing the rate of single excitations. Clearly, there is a trade off between suppressing multiple excitations and speed, which can be mitigated by the use of photon number resolving detectors or multiplexed memory nodes.

The signature of generating and retrieving collective excitations is a cross-correlation function between the heralding and retrieved fields that is larger than unity. The quantum nature of the protocol can be confirmed by violating the classical Cauchy-Schwarz inequality  $g_{\text{her,ret}}^{(2)}(\tau) \leq \sqrt{g_{\text{her,her}}^{(2)}(0) \times g_{\text{ret,ret}}^{(2)}(0)}$  (see eq. 2.14). Assuming thermal number statistics of the excitations, the classical limit becomes  $g_{\text{her,ret}}^{(2)}(\tau) \leq 2$ .

Resolving the weak heralding and retrieved fields in the presence of the bright write and read fields requires either strong, narrowband spectral filtering or a detection scheme with spectral resolution. We opt for the latter, which is straightforward using heterodyne detection in which the heralding and retrieved fields are mixed with a local oscillator detuned by some rf frequency. However the silicon PIN diodes we use in our detection are not sensitive at the level of single photons. We thus operate

in a high gain regime with many excitations per write pulse (exactly the scenario we noted earlier was to be avoided). While this regime is not useful for real quantum information applications, we are able to demonstrate the feasibility of storing and retrieving collective excitations while working toward implementing narrowband spectral filtering. We discuss at the end of this chapter progress toward demonstrating such a spectral filter. We also note that violating the Cauchy-Schwarz inequality in such a regime is challenging as the maximum violation goes as  $1/\langle n \rangle$  where  $\langle n \rangle$  is the mean number of excitations (see eq. 2.16).

The hyperfine level structure is shown in Fig. 3.6 and we store excitations on the  $\pm 1/2 \rightarrow \pm 3/2$  ground transition at 10.2 MHz. We use a double- $\Lambda$  configuration to ensure that the four fields present in the system (write, heralding, read, and retrieved) are at four distinct frequencies and a small write detuning (600 kHz) leads to multiple excitations generated by each write pulse, though without full depletion of the population in the initial state (Fig. 3.6). We implement a spectral hole-burning procedure similar to that of ref. [81] to isolate a narrow frequency class of ions in a particular ground state (Fig. 3.5). The final spectral profile consists of two 6 MHz-wide transmissive spectral trenches, one covering the write and retrieved transitions and the other the read and heralding transitions, with a 100 kHz-wide absorbing feature in the write trench.

We use a 4 mm x 4 mm x 20 mm  $\text{Pr}^{3+}:\text{Y}_2\text{SiO}_5$  crystal with 0.005 % Pr doping concentration. The optical transition we use is the  ${}^3H_4 \rightarrow {}^1D_2$  transition at 605.977 nm. This is the transition wavelength only for ions substituting for one of the two yttrium sites and is detuned by  $\approx 2$  nm from ions in the other dopant

site. The unit cell of  $\text{Y}_2\text{SiO}_5$  contains 8 molecules and has dimensions  $a=1.44$  nm,  $b=0.671$  nm,  $c=1.04$  nm and  $\beta=122.17^\circ$  [80]. Our hole burning and excitation fields propagate along the 2 cm length of the sample and have beam waists  $\approx 300$   $\mu\text{m}$ . Using the width of our absorbing feature ( $\approx 100$  kHz) and the full inhomogeneous broadening of the sample ( $\approx 1$  GHz) we estimate that we interact with an ensemble of  $\approx 10^{10}$  praseodymium ions  $[(0.005\%)(8 \text{ Y ions})((100 \text{ kHz})/(1 \text{ GHz}))((2 \text{ cm})(300 \mu\text{m})(300 \mu\text{m}))/(1.44 \times 0.671 \times 1.04 \times \sin(122.17^\circ) \text{ nm}^3)]$ . The sample is in a liquid helium cryostat pumped below the lambda point ( $\approx 2$  K) to suppress phonons and magnetic field coils are used to roughly null the local magnetic field. This field compensation reduces the splitting of the  $\pm I$  states to within the inhomogeneous broadening of the spin transition ( $< 10$  kHz) in order to avoid the extra dephasing that would be present due to any larger splitting.

Our experimental setup is shown in fig. 3.7. We use a continuous wave ring dye laser frequency stabilized to a Fabry-Perot cavity via a Pound-Drever-Hall locking scheme that achieves a sub-kHz linewidth. We use acousto-optic modulators to generate the hole-burning, write, and read fields. The write and read fields overlap in the crystal at a small angle ( $\theta \approx 0.5^\circ$ ) and we collect the co-propagating heralding and retrieved fields with a single-mode fiber directly between the write and read fields. The angle prevents the bright write and read fields from saturating the detector. This co-propagating geometry leads to a small phase mismatch  $\Delta \mathbf{k} = \mathbf{k}_{\text{her}} + \mathbf{k}_{\text{ret}} - (\mathbf{k}_{\text{write}} + \mathbf{k}_{\text{read}}) \approx (8\pi/\lambda)\sin^2(\theta/4) \approx 2 \text{ cm}^{-1}$  in the direction of propagation. The phase mismatch leads to reduced efficiency of readout, however the co-propagating heralding and retrieved geometry has the advantages of simpler alignment and the

need for only a single detection system as perfect phase matching would require collecting heralding and retrieved fields in separate and well-matched modes.

We can estimate the loss we expect due to the phase mismatch by following the treatment in, for example, [94] to find the emission as a function of angle due to the read field. We find that, compared to a system with no phase mismatch, the intensity of the emission in our collection mode is reduced by a factor of  $\left| \frac{1}{N} \sum_j e^{i\Delta\mathbf{k}\cdot\mathbf{r}_j} \right|^2$ , the square of the average phase seen by each atom in the ensemble, which clearly goes to zero for large  $\Delta\mathbf{k}$ . If we assume our atoms are randomly distributed over the length,  $L$ , of the sample we can rewrite the loss factor as  $\sin^2(\Delta kL/2) / (\Delta kL/2)^2 \approx 0.2$  giving a maximum retrieval efficiency of 20 % for our geometry (we note also that this is highly sensitive to the angle between the read and write beams, doubling the angle to  $1^\circ$  reduces this number to 1.5 %).

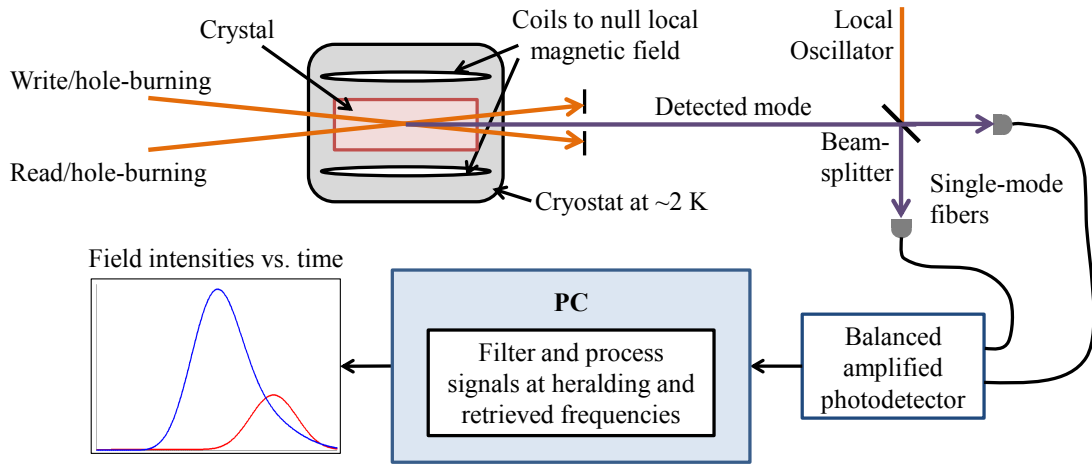


Figure 3.7: Experimental Setup.

We align this phase-matching configuration by performing a three-pulse photon echo and looking at the fields with a charge coupled device (CCD) camera (Fig. 3.8).

The photon echo sequence is  $\pi/2_{\text{input}}$ ,  $\pi/2_{\text{rephasing}_1}$ ,  $\pi/2_{\text{rephasing}_2}$ , echo. The phase matching condition for this echo sequence maps onto our quantum memory scheme with the input and echo as the heralding and retrieved fields and the rephasing pulses as the write and read. In Fig. 3.8 we see all four fields for reference, but for the experiment we use the image on the CCD to overlap the heralding and retrieved fields.

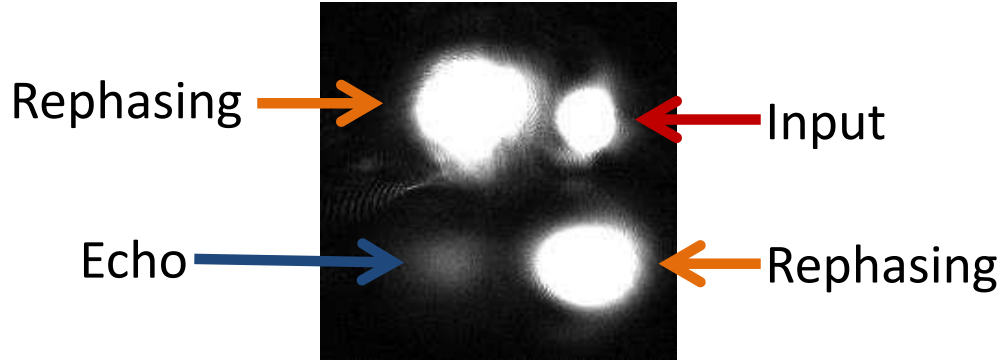


Figure 3.8: Example CCD image of a three pulse echo sequence used for aligning the phase-matching of the fields.

The write and read pulses are  $10 \mu\text{s}$  long transform limited pulses separated by  $35 \mu\text{s}$ . We implement the spectral hole-burning procedure described above before each write-read trial and repeat the full sequence 37,500 times. The detection is implemented with a commercial balanced amplified rf difference photodetector . We mix the heralding/retrieved mode on a 50/50 beam splitter with a local oscillator blue-detuned from all four fields by detunings  $\Delta_{\text{her}}$ ,  $\Delta_{\text{read}}$ ,  $\Delta_{\text{write}}$ ,  $\Delta_{\text{ret}}$  ranging from 5 MHz to 20 MHz. The signal from the difference amplifier is proportional to  $E_{\text{her}}e^{i\Delta_{\text{her}}t} + E_{\text{read}}e^{i\Delta_{\text{read}}t} + E_{\text{write}}e^{i\Delta_{\text{write}}t} + E_{\text{ret}}e^{i\Delta_{\text{ret}}t}$  where  $E_{\text{field}}$  are the amplitudes

of the electric fields in the various components.

We process the data in software and use the same time traces to obtain the intensities of the heralding and retrieved fields as functions of time. The amplifier output during each trial is beat down to dc by mixing it with a signal at  $\Delta_{\text{her}}$  ( $\Delta_{\text{ret}}$ ). The signal is Fourier transformed, put through a 1 MHz-wide filter, and inverse Fourier transformed back into the time domain. The square of the amplitude of the result of the inverse Fourier transform is proportional to the intensity in the heralding (retrieved) field.

### 3.3.2 Correlation model

As mentioned earlier, the signature of generation and retrieval of correlations is the cross-correlation between the heralding and retrieved fields. We defined the correlation functions in chapter 2 as a function of time difference  $\tau$ . Here we will look at the time resolved auto- and cross-correlations as a function of the times of the heralding and/or retrieved field detections with respect to the beginning of the trial. In this expression the  $\langle \rangle$  implies average over trials, not over all time, and  $j$  and  $k$  stand in for heralding or retrieved.

$$g_{j,k}^{(2)}(t_j, t_k) = \frac{\langle : \hat{n}_j(t_j) \hat{n}_k(t_k) : \rangle}{\langle \hat{n}_j(t_j) \rangle \langle \hat{n}_k(t_k) \rangle} \quad (3.2)$$

In practice, we normalize not by the overall mean number of photons in fields but by the correlation with the neighboring trials  $\langle \langle \hat{n}_k^{(\text{trial } i)} \hat{n}_j^{(\text{trial } i+1)} \rangle \rangle$  where the average is over trials  $i$ ). Slow drifts in the system cause the mean number of exci-

tations to vary over the course of many trials. This manifests as bunching in the canonical definition of the correlation function. The cross-trial normalization assumes that the trials are independent, which is the case in our system because we reset the medium with an incoherent hole-burning sequence each time.

We also note that in practice we compute the classical versions of the correlation functions, without normal ordering, because we do not insert a Hanbury Brown-Twiss interferometer into the detection. The error is proportional to  $1/\langle \hat{n} \rangle$ , which is small in our high gain regime. In order to properly obtain the normally ordered auto-correlation functions we would have to split the signal on a beam splitter before detection or calibrate the intensity detection to the true mean photon number and correct the classical version. Using the classical versions of the correlation functions also makes it impossible to observe violation of the Cauchy-Schwarz inequality, but as noted earlier the high gain regime makes the potential violation extremely small even with the correct correlation functions.

We can model what we expect to obtain for the auto- and cross- correlation functions of the heralding and retrieved fields. We assume a single mode of correlated emission with mean photon number  $\mu$  and thermal statistics; independent, uncorrelated emission in each arm with mean photon numbers  $\sigma_{\text{her}}$  and  $\sigma_{\text{ret}}$  and auto-correlation functions  $g_{\text{noise,her}}^{(2)}$  and  $g_{\text{noise,ret}}^{(2)}$ ; and independent, random losses in each arm  $\eta_{\text{her}}$  and  $\eta_{\text{ret}}$ . We do not assume anything about the statistics of the



uncorrelated emission. We find

$$\begin{aligned}
g_{\text{auto}}^{(2)} &= 2 - \frac{2\mu\sigma + \left(2 - g_{\text{noise}}^{(2)}\right)\sigma^2}{(\mu + \sigma)^2} \quad \text{for each field} \\
g_{\text{cross}}^{(2)} &= 2 + \frac{\mu(1 - \sigma_{\text{her}} - \sigma_{\text{ret}}) - \sigma_{\text{her}}\sigma_{\text{ret}}}{(\mu + \sigma_{\text{her}})(\mu + \sigma_{\text{ret}})} \\
g_{\text{cross}}^{(2)} &= 2 + \frac{1}{\mu} \quad \text{for } \sigma_{\text{her}} = \sigma_{\text{ret}} = 0.
\end{aligned} \tag{3.3}$$

We note that this does not depend on the losses in the heralding and retrieved arms. However, we see that the cross correlation decreases for larger mean photon numbers produced. For a given mean excitation number,  $g_{\text{cross}}^{(2)}$  is bounded by  $1 \leq g_{\text{cross}}^{(2)} \leq 2 + \frac{1}{\mu}$ . Thus, in practice, loss in the system forces operation at higher mean photon numbers and makes it more difficult to achieve large values for the cross-correlation.

We discuss our experimental results below in the context of this model.

### 3.3.3 Experimental results

Figure 3.9a shows the mean number of photons detected in the heralding and retrieved fields (solid lines) and the timing of the write and read pulses for reference (write and read are not to scale, only shown for timing). The heralding field is delayed with respect to the write field due to the strong absorption of the nearly resonant write field. The retrieved field is magnified 100x in the figure due to the low retrieval efficiency we observe. The shaded regions in figure 3.9a will be discussed below. The retrieval efficiency we observe (<1 %) is much lower than has been previously demonstrated in atomic gas systems (>50 %) or in other quantum memory protocols in REIC (69 %) [35, 95], but similar to other spin-state storage

protocols [96, 97]. One likely factor contributing to this inefficiency is the inherent phase-mismatch in our geometry discussed above. We expect moving to a geometry without an inherent phase mismatch would substantially increase the retrieval efficiency.

The measured cross-correlation between the detected heralding and retrieved fields is shown in figure 3.9b as a function of the detection times of both fields,  $t_h$  and  $t_r$ . The highest value of the cross-correlation is near the theoretical maximum for the high gain regime, 2.0(1) (statistical uncertainty). The correlation between the time separated heralding and retrieved fields is a signature of generation, storage, and retrieval of collective excitations. We note that the cross-correlation remains largely constant over the main part of the retrieved emission, seen as a broad maximum along the vertical axis. However the correlation peaks early during the heralding emission, and drops for later heralding detection times.

We check potential sources of correlations other than the generation and retrieval of collective excitations. We operate in a strongly phase mismatched configuration by applying co-propagating write and read pulses while collecting the heralding and retrieved light in a single spatial mode at a small angle (the only difference from Fig. 3.7 is that the read field propagates in the write mode). The heralding and retrieved fields in the detected mode should not be correlated with each other. The heralding field should be correlated with retrieved light in an undetected mode on the other side of the write/read mode at the same small angle. Unlike the small phase mismatch in the primary geometry, in which there is no better phase-matched mode for the retrieved field, this phase mismatch should eliminate correlations rather

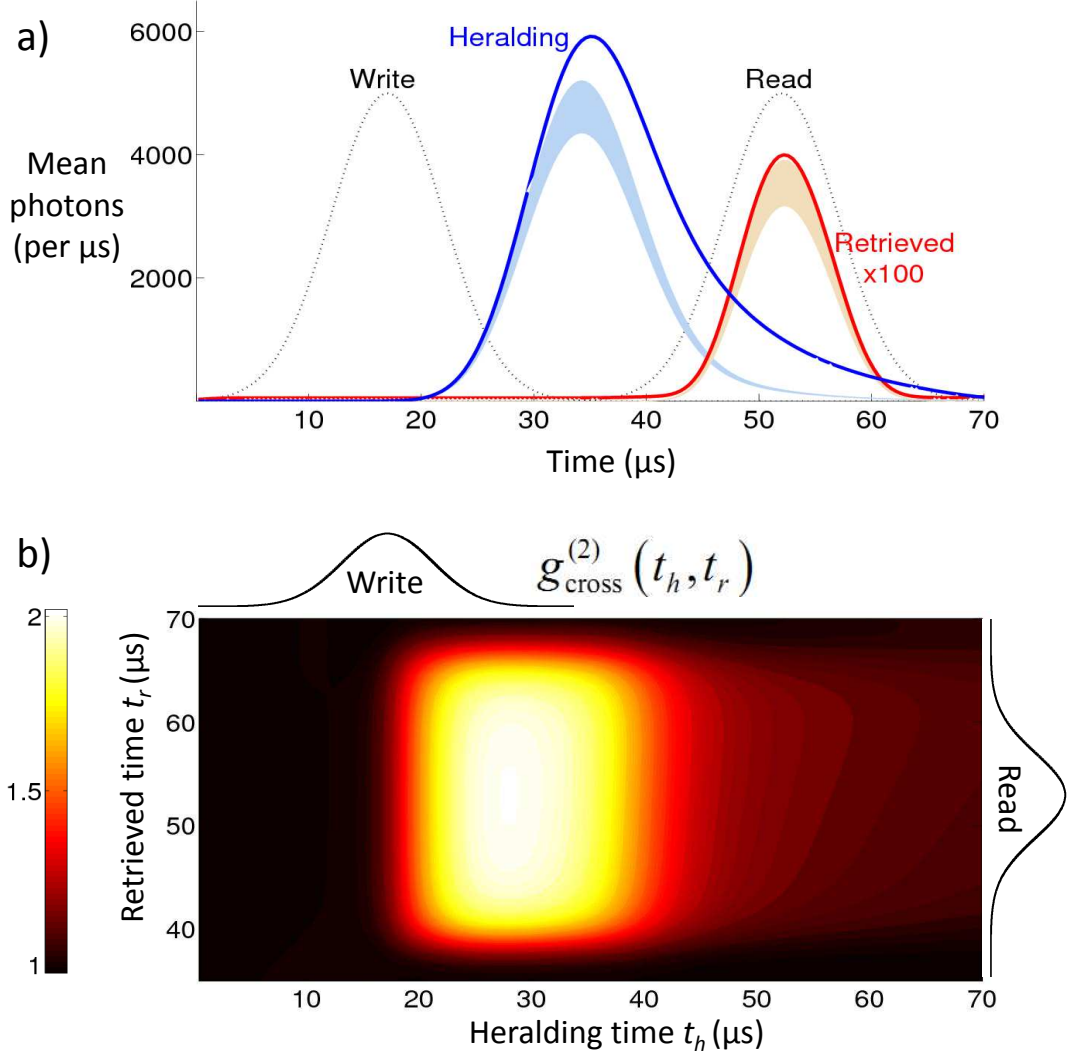


Figure 3.9: a) Mean detected heralding and retrieved (x100) photons per  $\mu\text{s}$ . Timing and width of write and read fields shown for reference, not to scale. Shaded bands are calculated profiles of the emission in the two channels that is correlated with correlated generation and retrieval. The widths of the bands represent the range of values that are consistent with the experimental results. b) Cross-correlation as a function of heralding (horizontal) and retrieved (vertical) detection times,  $t_{\text{her}}$  and  $t_{\text{ret}}$ . Write (read) temporal profile is fixed and shown along the heralding (retrieved) axis for reference.

than simply reducing retrieval efficiency ( $\Delta\mathbf{k} \approx (4\pi/\lambda)\sin(\theta/2) \approx 900 \text{ cm}^{-1}$ ). This configuration yields values of  $1.0 < g_{\text{cross}}^{(2)} < 1.3$  at all times, well below the values for the (nearly) phase-matched case. The lack of correlations in this configuration

implies that the correlations in the phase-matched case indicate coherent generation, storage, and retrieval of collective excitations.

The overall temporal behavior in our system is qualitatively different than what was seen in early experiments in cold atomic gas systems. Decoherence was so fast as to dominate the temporal dynamics, and the storage time ( $t_{\text{ret}} - t_{\text{her}}$ ) was the primary factor that determined the correlation [98]. Our system exhibits cross-correlation that is largely constant during the retrieved field, suggesting that there is negligible decoherence of the collective excitation during storage. This is consistent with previously reported coherence times for the spin transition  $\text{Pr}^{3+}:\text{Y}_2\text{SiO}_5$ , which are longer than the storage time demonstrated here [99]. However, the reduction of the cross-correlation for later detection times of the heralding field suggests the presence of an additional noise process with a temporal profile delayed with respect to the generation of collective excitations. We use equation 3.3 and our measured values of  $g_{\text{cross}}^{(2)}(t_{\text{her}}, t_{\text{ret}})$  to estimate the amount of uncorrelated emission in the fields ( $\sigma_{\text{her}}$  and  $\sigma_{\text{ret}}$ ) as functions of  $t_{\text{her}}$  and  $t_{\text{ret}}$ . We assume some fluctuation of the mean collective excitation rate,  $\mu$ , due to drift of experimental parameters such as laser intensity and pointing and find ranges of  $\sigma_{\text{her}}$  and  $\sigma_{\text{ret}}$  that are consistent with the data. Our results for the fraction of emission that is correlated with the generation and retrieval of collective excitations are plotted as the shaded bands in figure 3.9a along with the measured emission in each field. While the retrieved field is composed primarily of correlated emission, we find that the heralding field contains significant noise. We further note that the correlated and noise photons in the heralding field exhibit distinctly different temporal dynamics. Namely, we find that the correlated

field in the heralding channel peaks earlier than the overall emission, and that the tail of the emission is largely noise. This temporal separation should allow for gating of the heralding field to improve the fidelity of the heralding process.

### 3.3.4 Spectral filtering

As mentioned earlier, moving to the single excitation regime requires narrow-band spectral filtering that allows detection of single photons in the heralding and retrieved fields in the presence of the bright, classical write and read beams. We have begun work to develop a switchable, narrowband spectral filter based on spectral hole-burning in  $\text{Pr}^{3+}:\text{Y}_2\text{SiO}_5$  [100]. The switching is accomplished via the dc Stark effect that shifts the transition frequencies of the ions in the ensemble and importantly allows the same crystal to act as a filter during both the write and read processes.

The filter is prepared by first burning a spectral hole centered at  $\omega_1$  with a particular electric field configuration applied to the crystal. The electric field is then switched (switching time  $< 1 \mu\text{s}$ ) to an alternate distribution to shift all ions via the dc stark effect, and a spectral hole is burned at  $\omega_2$ . This hole-burning process is repeated many times, iterating between the two field configurations. The final result is two spectral profiles encoded in a single ensemble with the ability to choose which profile to use by switching the electric field. This scheme has been demonstrated with 60 dB attenuation for each of two 1 MHz-wide spectral holes in a 2-cm  $\text{Pr}^{3+}:\text{Y}_2\text{SiO}_5$  crystal (Fig. 3.10).

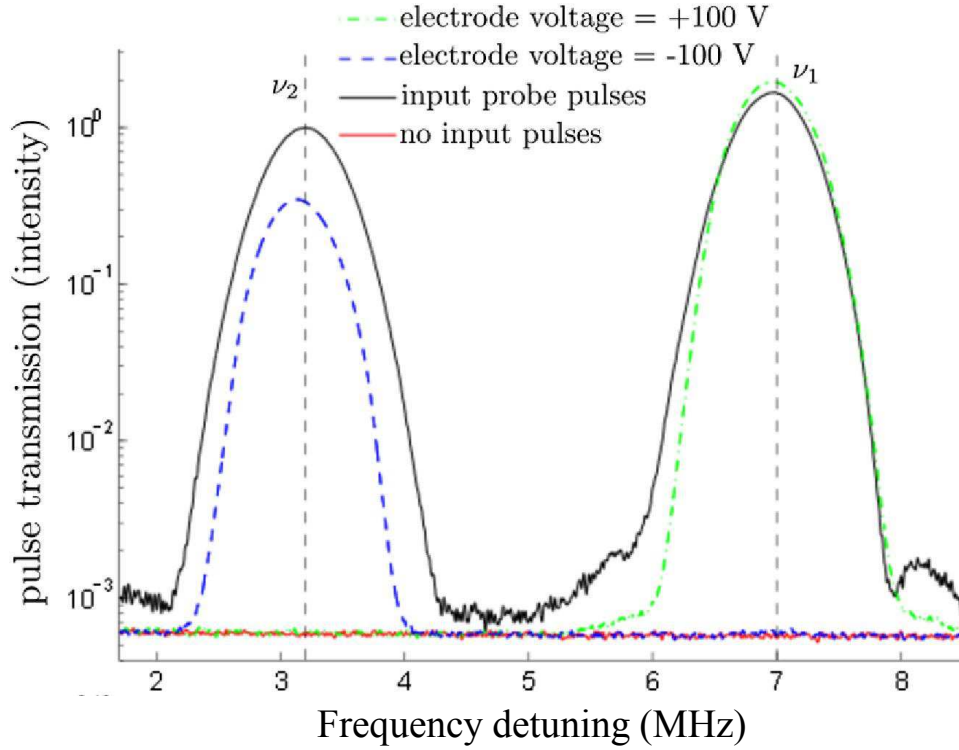


Figure 3.10: Filter transmission measured via heterodyne detection for two electric field configurations ( $\pm 100$  V). In both cases the ratio of the maximum to minimum transmission is  $>65$  dB. [100]

A filter of this type, integrated into a quantum memory system, should allow storage and retrieval of collective excitations in a DLCZ-type scheme at the single photon level. Along with the results storing and retrieving collective excitations this work suggests that a DLZ-type quantum memory is entirely feasible in rare-earth systems.

## Chapter 4: Non-classical detection for metrology

Since the advent of photomultiplier tubes in the 1930s it has been possible to detect light at the level of single optical photons. Most detectors that are sensitive at the level of a single photon, however, cannot distinguish the number of photons in a pulse. Such single photon counters simply signal a photo-detection event for any number of photons detected. This lack of photon number resolution is a challenge for many applications throughout quantum optics and quantum information [17] and has led to substantial research in recent years into developing photon number resolving (PNR) detectors.

A common method for obtaining photon number resolution is by multiplexing single photon counters, which is a technique we use in chapter 5 of this thesis to reconstruct the underlying modes of a light field. Such schemes are generally easy to implement and flexible due to the variety of single photon counters with different fundamental properties that are available. Such multiplexed systems, however, are limited in their degree of photon number resolution by the number of detectors, or in the case of temporal multiplexing with a single detector, the repetition rate. They also have reduced sensitivity for photon numbers near the number of detectors and tomography of such a system is generally required to fully characterize its

photoresponse [37].

Detectors with the ability to directly resolve the number of incident photons are rare, but becoming more common in the last decade [17]. One intrinsically PNR detector is the transition edge sensor (TES), a microbolometer capable of distinguishing photon number for a monochromatic source based on the amount of energy deposited on its superconducting tungsten film [101–103]. The energy deposited causes a temporary change in current whose integral is proportional to the energy absorbed. Thus, output photoresponse pulses from the TES can be integrated to yield the number of photons absorbed in each pulse. Clear discrimination of photon number greater than ten has been observed for 1550 nm photons [101, 104].

In this chapter we describe an experiment using a TES to study the limits of resolution and sensitivity in imaging and metrology applications [39]. There is widespread interest in improving resolution and sensitivity in imaging and metrology applications [105–109], but many of the proposed improvements for precise phase measurements and high-resolution imaging employ highly non-classical photon states such as photon-number (Fock) states and path-entangled photon-number (N00N) states or squeezed states [108, 110]. Unfortunately, such non-classical states are highly sensitive to loss [111]. This has led to interest in combining loss-tolerant coherent states with photon-number-resolving detectors to realize some improvement over standard classical techniques and avoid the immense challenges associated with generating exotic quantum states [112–116].

In the context of imaging, much attention has focused on improving resolution beyond the Rayleigh limit [117]. This limit is imposed by diffraction rather than



by quantum fluctuations of the light [116]. Giovannetti *et al.* proposed that PNR strategies could result in high-resolution images beyond the standard Rayleigh criterion [118]. They note that using a coherent source and a PNR measurement compresses the point spread function of an image but does not lead to improved image resolution. This compression could also be accomplished by classical post-processing of the data; however, it is not clear whether post-processing has an advantage in the presence of noise. Near the single-photon level, the presence of stray light degrades the utility of such post-processing, and classical detection itself becomes challenging. Nonetheless, direct detection of fringe compression can be used to improve the contrast between closely spaced diffracted beams. Similar techniques can also be used to improve contrast for applications other than imaging, for instance spectroscopy of radioactive atoms where the background count rate is high, but the increased likelihood of higher order photon number events on resonance allows better contrast of the spectral features by conditioning on higher order events [119].

Here, we report two experiments using PNR detectors to study the spatial irradiance profile of diffracted laser beams. The main components of our experimental setups are a laser source, a TES and a single slit, or pinhole. Our 1550 nm laser diode source has linewidth  $\approx 0.1$  nm, is modulated at 50 kHz, and is pulsed with 100 ns-wide pulses. We first diffract a Gaussian beam at a single slit and observe the expected narrowing of spatial fringes with increasing detected photon number. We then use this fringe compression to demonstrate increased contrast of two beams with Airy disk profiles separated by less than the separation given in the Rayleigh criterion.

## 4.1 Fringe compression

In our first experiment, we study the photon-number-resolved spatial profiles of a single-slit diffraction pattern. In the experimental setup, a beam exits a single-mode fiber and is collimated to generate a Gaussian profile with a beam waist several millimeters in diameter. It is then diffracted through a single  $\approx 250 \mu\text{m}$ -wide slit. We scan a standard  $9 \mu\text{m}$  core single-mode fiber coupled to the TES detector across the diffraction profile in  $50 \mu\text{m}$  steps,  $\approx 23 \text{ cm}$  from the slit, and detect a mean of  $\approx 3.6$  photons per pulse at the position of maximum irradiance. At each fiber position, we resolve photon number by integrating TES photoresponse pulses and placing them into histograms to reveal the photon number distribution [101]. The detected photon numbers can be extracted from these histograms, and in this experiment, we distinguish up to nine photons (higher photon numbers are neglected due to low count rates). Thus, the spatial diffraction patterns of different photon-number states are extracted.

We observe increased compression of the central lobe with increasing detected photon number, by up to a factor of three over a classical (average irradiance) signal (see Fig. 4.1). We reconstruct this classical signal from the PNR measurements by taking  $\sum k n_k$  where  $k$  is the detected photon number and  $n_k$  is the number of counts at a given  $k$  (see Fig. 4.1a). We observe the  $\text{sinc}^2(d \sin\theta/\lambda)$  dependence we expect from diffraction through a single slit, where  $d$  is the slit width,  $\lambda$  is the wavelength, and  $\theta$  is the angle ( $\theta \approx x_t/z$  where  $x_t$  is the transverse position seen in Fig. 4.1 and  $z \approx 23 \text{ cm}$  is the distance from the diffracting slit to the detection plane).

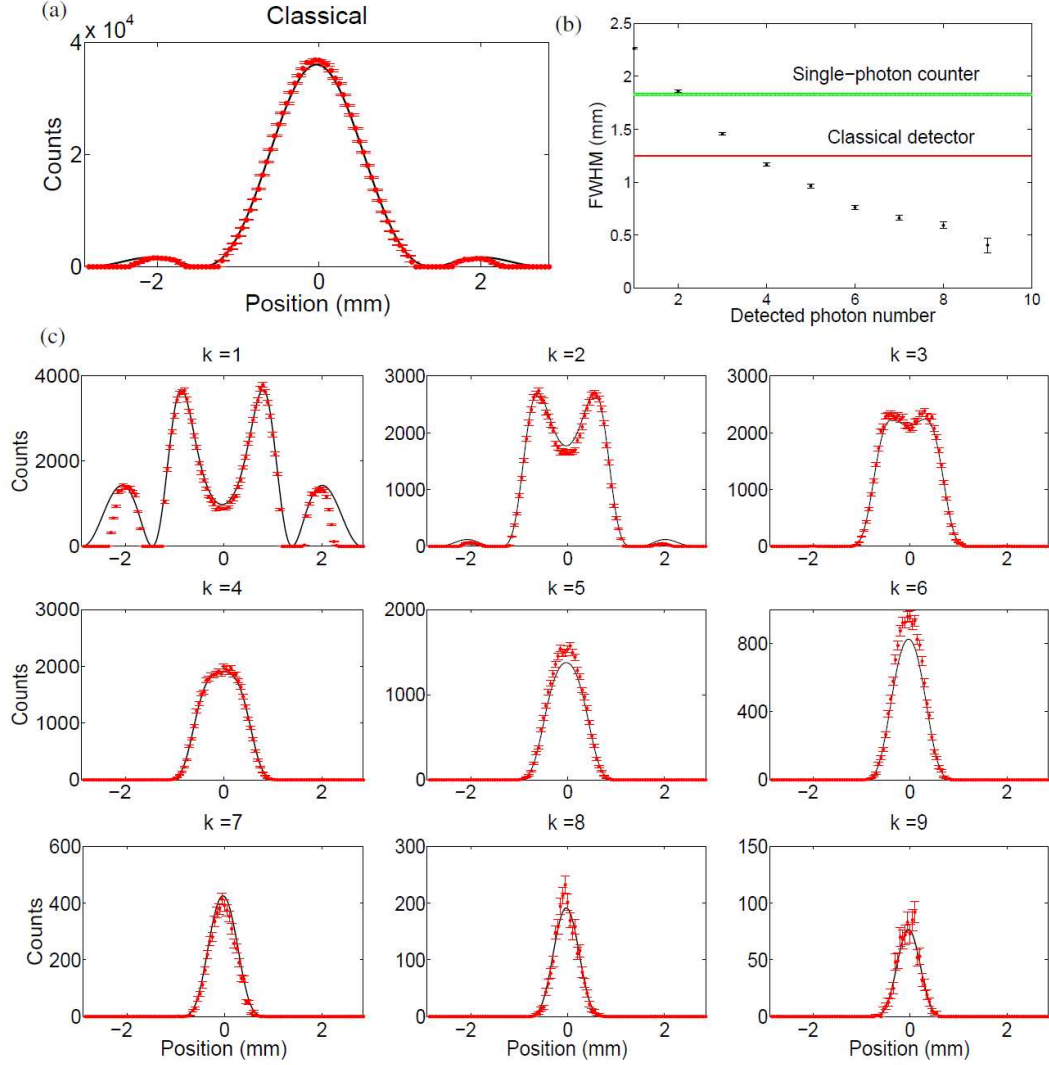


Figure 4.1: (a) Reconstructed classical spatial distribution with fit. (b) Full width at half maximum of the central fringe vs. photon number. Expected widths using reconstructed classical and conventional single-photon detectors shown for reference. (c) Spatial distribution of the diffraction pattern for up to nine photons with fits. Solid black lines are fit generated by minimizing the least-squares error between the data and a Poissonian distribution with a mean photon number that falls along the curve  $\mu(x) = \mu_0 \text{sinc}^2(d \sin \theta / \lambda)$ .

We then generate a fit to this curve by minimizing the least-squares error between  $\mu \cdot \text{sinc}^2(d \sin \theta / \lambda)$  and the data by varying  $\mu$  and  $\theta$ . We derive the photon-number profiles straightforwardly from the Poissonian distribution of a coherent source with a spatially varying detected mean photon number  $\mu(x) = \mu_0 \text{sinc}^2(d \sin \theta / \lambda)$  (see

Fig. 4.1c). The photon number distribution at each point is given by the Poisson distribution for the mean photon number at that position  $\mu(x)$ .

This result can also be derived using an effective beamsplitter approach, as described in Ref. [113]. In this case, the diffraction limited beam profile is modeled as a plane wave incident on a beamsplitter with spatially varying transmission coefficient  $T$  [113, 114, 120]. The equivalence between the two approaches can be shown directly in that the beamsplitter expression for the probability of detecting  $k$  photons reduces to a Poisson distribution:

$$p(k) = e^{-\mu} \sum_{j=k}^{\infty} \frac{\mu^j}{k!(j-k)!} |T|^{2k} (1 - |T|^2)^{j-k} = e^{-\mu|T|^2} \frac{(\mu|T|^2)^k}{k!}, \quad (4.1)$$

where  $|T|^2$  is replaced by the spatial profile of the beam, which in this case is the single slit far-field diffraction profile ( $\text{sinc}^2(d\sin\theta/\lambda)$ ).

The compression of the central fringe width we observe could also be obtained by post-processing of a classically detected signal. However, because classical detection at low intensities is difficult, such measurements are often performed with conventional single-photon detectors (with no photon-number discrimination). We compare our results with what we would have obtained with a conventional single-photon detector, which records a photodetection event for every pulse with one or more detected photons. By treating the single and multi-photon detection events from all of the photon-number resolved profiles in Fig. 4.1c as identical photodetection events, we reconstruct the spatial profile obtainable with a conventional single-photon detector and find that our result is compressed by a factor of more

than four (see Fig. 4.1b). We note that the fringe width obtained with a conventional single photon detector is wider compared to a classical average irradiance measurement because the response of a non-number-resolving detector cannot scale with photon flux, but saturates with the detection of a single photon.

We can convert the width  $\sigma$  of the feature into an error on the ability to find the center of the distribution. We take the error on the peak location for a set of data as  $\epsilon = \sigma/\sqrt{n}$  where  $n$  is the number of counts in the distribution. We can combine the different theoretical photon number resolved profiles using a weighted average depending on the overall mean photon number. Figure 4.2 shows the relative error for single photon detection (SPAD), classical intensity detection, and photon number resolved detection with 12- and 4-fold resolution. This illustrates the advantage of accessing the higher photon number statistics of the radiation field over using conventional single-photon detectors as the error for both PNR detection schemes falls below the error for the single photon detector at all mean photon numbers. However, we see that if classical intensity detection is possible, it will provide a lower error than photon number resolved detection.

## 4.2 Beam contrast

In the second experiment, we exploit the fringe compression observed above to study improved contrast of spatial profiles of two overlapping diffraction patterns with approximately equal irradiance, which are difficult to distinguish classically. To obtain this profile, we first diffract a  $\approx 2$  mm diameter Gaussian profile beam through

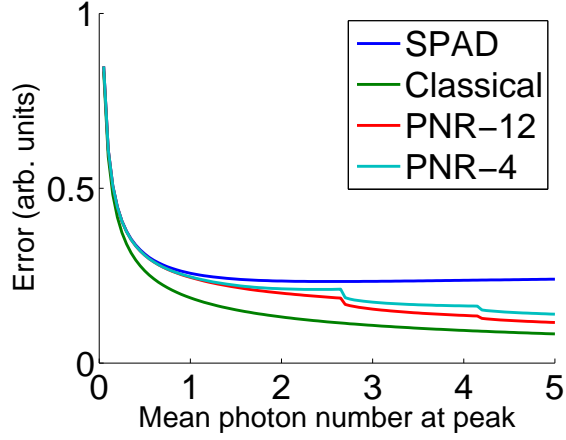


Figure 4.2: Error on the location of the center of the distribution that can be found using single photon detection, classical intensity detection, and 12- and 4-fold photon number resolved detection as a function of the mean photon number at the peak of the field.

a standard  $75 \mu\text{m}$  pinhole, obtaining a beam with an Airy disk profile. A 100 mm focal length lens,  $\approx 155$  mm after the pinhole, focuses the diffraction profile. The beam is split and recombined non-interferometrically using polarizing beam splitters in a Mach-Zehnder interferometer configuration (see Fig. 4.3b). We approximately equalize the photon flux in the arms using a fiber polarization controller and tune the spatial separation of the two beams by moving one of the mirrors. The detection system scans across the two nearly identical images for several different beam separation values while recording all photoresponse pulses. The maximum detected mean photon number per beam for all measurements is  $\approx 5.3$ , and we distinguish photon numbers up to twelve.

The Rayleigh criterion defines the classical limit for the minimum resolvable

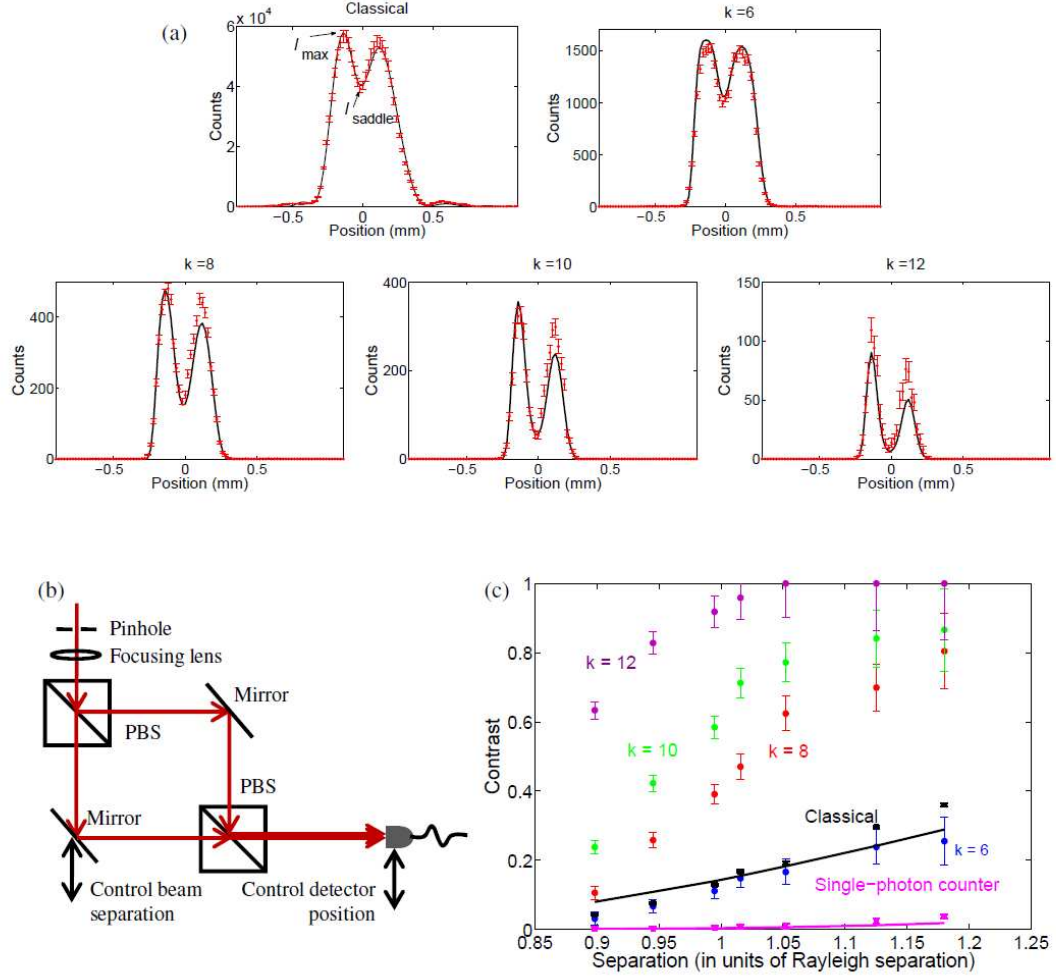


Figure 4.3: (a) Spatial profile at approximately the Rayleigh criterion for the reconstructed classical signal and photon-number detection at selected photon numbers larger than the mean photon number. (b) Experimental setup. PBS: polarizing beam splitter. (c) Contrast ( $C = (I_{\max} - I_{\text{saddle}}) / (I_{\max} + I_{\text{saddle}})$ ) vs. beam separation (in units of the Rayleigh criterion) for select photon numbers larger than the mean photon number. Contrasts derived from the reconstructed classical profile and single-photon counter profile are shown for reference.

separation between two imaged, focused Airy disk profiles

$$\left( \frac{2J_1 \left( \pi D \sqrt{x^2 + y^2} / \lambda f \right)}{\pi D \sqrt{x^2 + y^2} / \lambda f} \right)^2, \quad (4.2)$$

where  $J_1$  is a Bessel function of the first kind,  $x$  and  $y$  define the position in the image

plane,  $f$  is the focal length, and  $D$  is the aperture radius of the diffracting pinhole. This separation occurs where the main lobe of one beam falls on the first minimum of the other, and the angular separation with respect to the aperture is given by  $1.22\lambda f/D$ . The classical irradiance profile of two overlapping Airy disks is a saddle, and the contrast of this profile is defined as  $C = (I_{\max} - I_{\text{saddle}}) / (I_{\max} + I_{\text{saddle}})$ , where  $I_{\max}$  and  $I_{\text{saddle}}$  are the intensities at the peak and saddle points (see Fig. 4.3a).

The expected classical contrast for two equal intensity beams at the Rayleigh limit is 15 %. We observe contrast values greater than 80 % for detected photon numbers  $k \gg \mu$  at a separation of the Rayleigh limit (see Fig. 4.3c). At the smallest separation value studied, 90 % of the Rayleigh limit, a contrast of over 60 % is obtained for  $k = 12$ . We note that the contrast value of 13 % obtained from the reconstructed classical profile just below the Rayleigh limit matches closely with the theoretical Rayleigh limit value of 15 %. As expected, the contrast of reconstructed profiles assuming the use of a conventional single photon detector is  $< 5$  %, because it saturates and loses information by not exploiting the full photon statistics. We show a sample set of measured photon-number-resolved profiles for a separation near the Rayleigh limit along with a theoretical fit derived analogously to the fit used for the single-slit configuration. Fitting parameters account for the intensity difference of the two beams and the difference in optical path lengths. We show good agreement between the fits and data.

We have thus far demonstrated improved contrast between two Airy beam profiles at the Rayleigh criterion, using a coherent source which obeys Poissonian



statistics. This raises the question of the effect of a source’s statistical properties on the fringe compression and contrast measured with photon-number-resolving detectors. We point out that the compression of the central fringe is merely a consequence of the beam’s photon statistics in combination with PNR detection rather than a consequence of a particular aperture. Thus, this compression effect can be observed for any photon-number-resolved, diffraction-limited beam. To this end, we simulate photon-number-discriminated spatial distributions of Gaussian beam profile fields with coherent, thermal, and Fock statistics. We use the effective beamsplitter approach described above with a Gaussian profile replacing  $|T|^2$  in Eq. 4.1 and the appropriate photon statistics. As shown in Fig. 4.4 for  $k = 10$ , the Fock state ( $|n\rangle = 10$ ) shows the highest degree of narrowing of the central fringe.

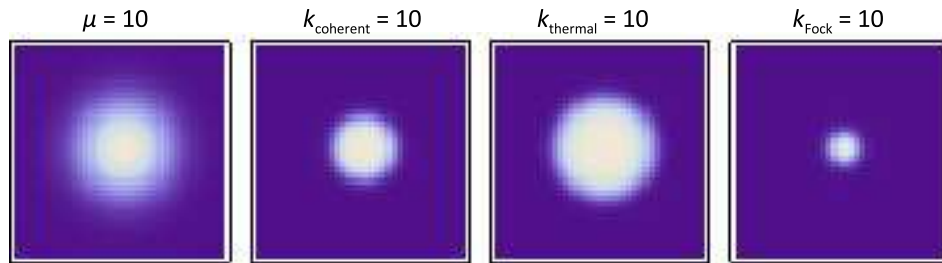


Figure 4.4: Calculated spatial distribution of (from left to right) a classically detected Gaussian profile coherent beam with a mean photon number of 10, a 10-photon detection of the same coherent state, a 10-photon detection of thermal light and same mean photon number, and a 10-photon detection of  $N=10$  Fock state.

This narrowing can translate directly into improved contrast if we add two coherent states or thermal states near the Rayleigh limit without interference as in our setup. The reason is that the compression from photon-number-resolved

detection acts on the sum of the irradiance profiles of the beams [118]. Thus, for these cases, the contrast is dictated completely by the amount of compression, which results in higher contrast for the Fock state profile over the thermal or coherent state profile. We note in this case that any increase in contrast can only occur for separations larger than the Sparrow limit,  $\approx 0.8$  of the Rayleigh criterion, where the two overlapping beam profiles combine to form a flat top [121]. The reason is that the photon-number-resolving detection amplifies the dip feature in profiles between two beams. In the case of two beams separated by less than the Sparrow limit, no such feature can be exploited.

In conclusion, we have experimentally observed the photon number resolved transverse profile of diffracted beams. We directly observe fringe compression of the diffraction pattern that is not possible with classical detectors or conventional single photon detectors. This fringe compression leads to the ability to better locate a peak than is possible with conventional single photon detectors. We further demonstrate that this fringe compression allows increased contrast of two nearly overlapping Airy disk profiles and discuss the effect of the source statistics on fringe compression. These studies may be useful for designing better metrology and imaging techniques.

## Chapter 5: Characterizing light

In chapter 2 we discussed how photon number statistics can be used to characterize light. In this chapter we present three experiments in which we do just that. In the first experiment we used the zero-time second-order intensity auto-correlation function,  $g^{(2)}$ , to characterize the multi-photon emission of a bright, broadband, fiber-based heralded single photon source [18]. In the second experiment we demonstrated the quantum nature of light by using entangled photons from this fiber source to violate theories of local and non-local realism [27]. In the third experiment we demonstrated the mode reconstruction method outlined in chapter 2. We reconstruct mixed states with contributions from up to three modes with thermal statistics, up to one mode with attenuated single-photon statistics, and up to one mode with Poissonian statistics [25].

### 5.1 Heralded single photon source

A common way to generate single photons is by producing photons in pairs and using one member of the pair to herald the presence of the other. Most physical processes that produce photon pairs do so in such a way that the number of pairs has a classical number distribution ( $g^{(2)} \geq 1$ ). So while either arm of the pair source will

exhibit  $g^{(2)} \geq 1$ , we can measure the conditional  $g^{(2)}$  of one arm by only considering pulses or time bins during which a photon is detected in the other arm. This conditioning decreases the probability of finding no photons in the signal, increasing the mean photon number without significantly changing the ratio of multi-photon emission to single photon emission. Thus, the conditional normalized correlation  $g_{\text{cond}}^{(2)}$  can be well below one, signifying a nearly pure single photon source. In the regime of a weak pair source with unconditional probability  $p_{\text{unc}}(1) \ll 1$  we demonstrate  $g_{\text{cond}}^{(2)} < 0.02$ .

This has been the primary method for obtaining single photons for a number of years even though there is a trade off between the real time rate of photons and the multi-photon suppression. To date, the most common physical system for photon pair generation has been spontaneous parametric down conversion (SPDC) in nonlinear crystal. On the other hand, pair production in optical fiber, rather than bulk crystal or waveguide, has the advantage photons can be produced, collected, encoded, distributed, and detected in a single transverse spatial mode.

Four-wave mixing (FWM) is a third-order nonlinear process in which two pump photons are converted into a pair of photons, termed signal and idler, constrained by energy and phase matching constraints. In amorphous-silica optical fiber, there is no second-order nonlinear susceptibility (and thus no possibility of SPDC). FWM in optical fiber has been shown to produce correlated photon pairs with high two-photon spectral brightness over a broad spectral range in a single-spatial-mode [122–125]. These features give fiber-based sources of correlated photon pairs unique advantages as heralded single-photon sources. The broad spectral bandwidth allows wavelength-

division-multiplexing at the single-photon level and the single-spatial-mode output allows photon collection with high efficiency. We measured the conditional second-order correlation function [42, 126],  $g_{\text{cond}}^{(2)}$ , of heralded single-photons generated via FWM in optical fiber to be much less than unity over a broad spectral range, suggesting that fiber-based heralded single-photon sources may be suitable for future quantum information applications.

We generate photon pairs in microstructure fiber, which is standard silica optical fiber that has a pattern of air holes that run the length of the fiber with the central hole absent (see fig. 5.1). The central, filled region acts as the fiber core in which the mode is guided and the surrounding air-filled holes act as the cladding. Compared to traditional single mode fiber, microstructure fiber has a smaller core diameter ( $\approx 1 \mu\text{m}$  vs.  $\approx 10 \mu\text{m}$ ) and a larger index difference between the core and the cladding ( $\Delta n \approx 0.4$  vs.  $\Delta n \approx 0.01$ ). Both of these effects contribute to an increased nonlinear coefficient, and thus a larger four-wave mixing gain, in microstructure fiber over standard single mode fiber [127].

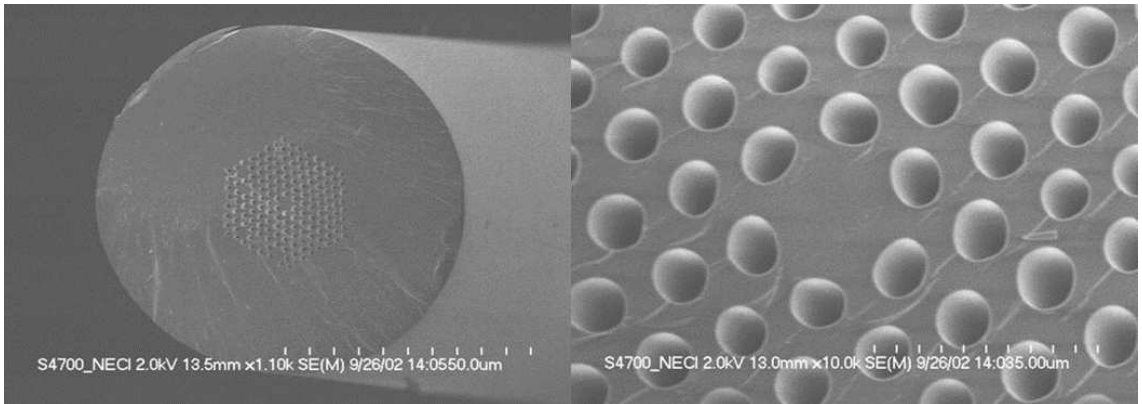


Figure 5.1: Scanning electron microscope image of microstructure fiber. The small core size and large index difference between the silica core and air cladding lead to high nonlinearity and four-wave mixing gain.

In the experiment (Fig. 5.2), 8 ps pulses from a mode-locked Ti:Sapphire laser are coupled into a microstructure fiber at a repetition rate of 76 MHz, with pump wavelength ( $\lambda_{\text{pump}} = 740.6 \text{ nm}$ ) located slightly on the normal-dispersion side of the fiber (zero-dispersion-wavelength  $\lambda_{\text{ZDW}} = 745 \text{ nm} \pm 5 \text{ nm}$ ). The high third-order nonlinearity ( $\gamma = 70 \text{ W}^{-1}\text{km}^{-1}$ ) of the fiber enables efficient FWM over a broad spectral band, depending on phase matching. A major source of noise in FWM in optical fiber is Raman scattering, which produces single, uncorrelated photons in a spectral region near the pump wavelength. The primary Raman scattering spectral band peaks at 765 nm in our fiber (see Fig. 5.3 inset), but careful selection of phase-matching conditions allowed us to efficiently produce photons outside the Raman band, detuned from the pump by 25-35 THz.

We measured a 20 nm wide bandwidth where the FWM signal is large but the accidental two-photon coincidence noise is small [124]. A two-pass grating configuration selects the frequency-conjugated signal ( $\omega_s$ ) and idler ( $\omega_i$ ) photon wavelengths that are connected by energy conservation,  $2\omega_{\text{pump}} = \omega_s + \omega_i$ . A slit following a transmission grating in the signal (idler) path allows selection of the signal (idler) wavelength via the position of the slit and the signal (idler) bandwidth via the width of the slit. Because the FWM process creates correlated pairs of signal and idler photons, the detection of a signal photon can be used to herald the existence of an idler photon, or vice versa.

The idler goes through a Hanbury Brown-Twiss interferometer in which the field is split on a 50/50 beamsplitter and sent to two single photon avalanche detectors ( $a$  and  $b$ ) while the signal field goes directly to a single photon avalanche

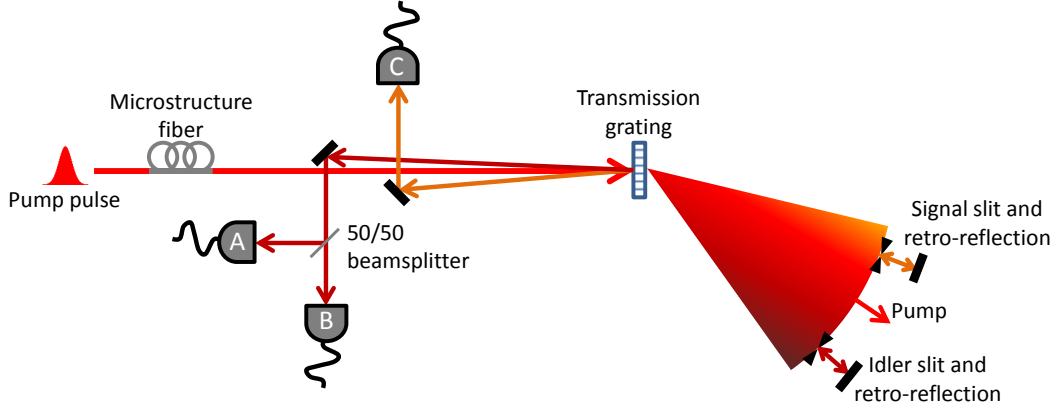


Figure 5.2: Experimental setup for the microstructure fiber pair source. Pair wavelengths are selected by the slits and retroreflecting mirrors following the transmission grating.

diode (detector  $c$ ). Thus, the conditional second-order correlation function is  $g_{\text{cond}}^{(2)} = p_{abd}/(p_{ac}p_{bc})$  while the unconditional correlation is  $g_{\text{unc}}^{(2)} = p_{ab}/(p_a p_b)$  where  $p_{ijk}$  is the probability of a time bin containing photodetections in the subscripted detectors. We measure the overall single-photon detection efficiencies to be  $\eta_s = 5\%$  for the signal arm, and  $\eta_a = 7\%$  ( $\eta_b = 7\%$ ) for idler arm a (idler arm b). [Breakdown of signal (idler) photon detection efficiencies: detection efficiency = 60% (50%), fiber coupling efficiency = 53% (58%), interference filter transmittance = 53% (60%), two passes through transmission grating efficiency = 39% (58%), efficiency from other optics = 75% (70%)].

In the experiment, photons collected in the signal and two idler arms are independently coupled into a Perkin Elmer SPCM-AQ4C four-channel silicon avalanche photodiode (APD) array. Each APD functions independently, outputting an electrical signal when detecting a photon (with 50 ns deadtime after each detection). The

electrical signals are fed into a home-built field programmable gate array (FPGA) that is synchronized to the 76 MHz pulsed laser and has 13 ns wide time bins [128]. The FPGA compares the input signals and reports coincidence analysis to a data-taking computer. Relative delays between signals from different channels are optimized for maximal coincidence rates with the temporal resolution of 100 ps.

We measure the conditional and unconditional correlations ( $g_{\text{cond}}^{(2)}$  and  $g_{\text{unc}}^{(2)}$ ) of the idler for different signal-idler wavelength pairs (Fig. 5.3a) and different collection bandwidths (Fig. 5.3b) to demonstrate that the multi-photon emission is suppressed over a wide bandwidth. It is important to note that shifting to a different signal-idler wavelength pair simply requires moving the slits in front of the retro-reflective mirrors (see Fig. 5.2) using micrometer stages, and does not require any optical realignment. We observe that  $g_{\text{cond}}^{(2)}$  is far below the classical limit of unity at low pump power. We see the expected rise in  $g_{\text{cond}}^{(2)}$  for higher pump powers. As discussed in chapter 2, the degree of multi-photon suppression possible with a heralded source decreases with increasing pair production rate.

We see that  $g_{\text{unc}}^{(2)} \approx 1.5$  and is larger for smaller collection bandwidths  $\Delta\lambda$ . We are collecting multiple spectral modes of the idler field, each of which we expect to exhibit thermal number statistics. Thus we expect a value of  $g_{\text{unc}}^{(2)}$  between 2, the value for a single thermal mode, and 1, the value for an infinite spectrum of thermal modes. At smaller bandwidths we collect fewer modes and thus see larger  $g_{\text{unc}}^{(2)}$ . The dip in  $g_{\text{unc}}^{(2)}$  at low pump powers is due to the contribution of random dark counts at those count rates, otherwise we observe constant  $g_{\text{unc}}^{(2)}$  for each set of experimental parameters, as expected from one arm of a pair source.



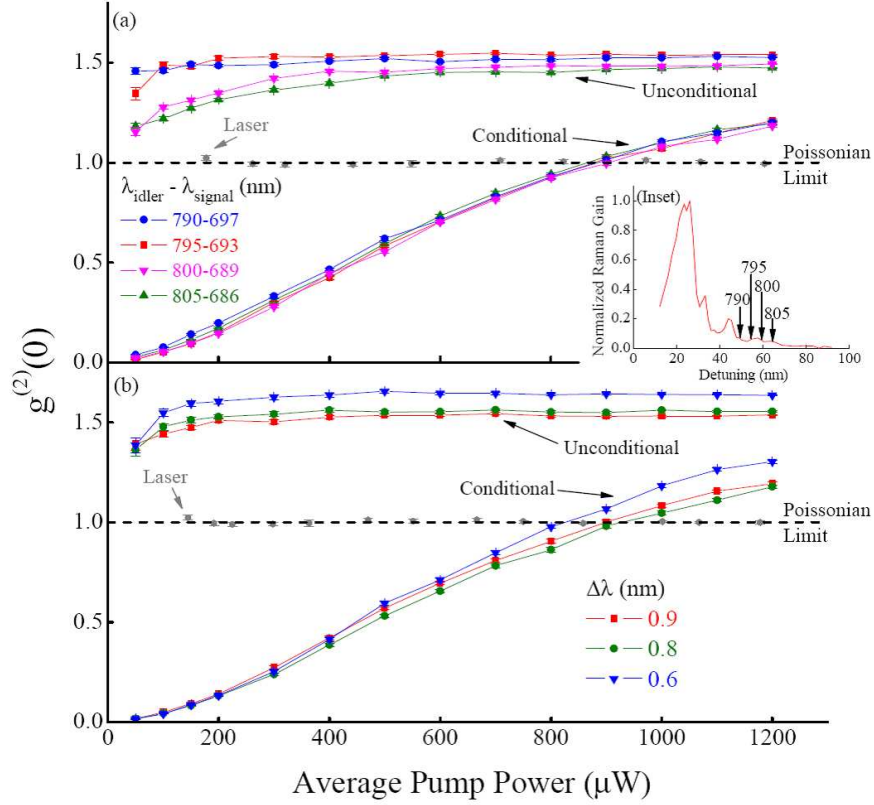


Figure 5.3: Conditional and unconditional  $g^{(2)}$  vs. pump power. (a) Different wavelength pairs.  $g_{\text{cond}}^{(2)}$  is near zero for low pump power (low pair production) and rises above the classical limit at high power.  $g_{\text{unc}}^{(2)}$  is between 1 and 2 for all wavelengths as expected for a multimode thermal source. (b) Different bandwidths for the pairs.  $g_{\text{cond}}^{(2)}$  is near zero for low pump power (low pair production) and rises above the classical limit at high power.  $g_{\text{unc}}^{(2)}$  is larger for smaller bandwidth, as expected for a source with multiple spectral modes. The lower values of  $g_{\text{unc}}^{(2)}$  for low pump power are a function of detector dark counts, which have a much smaller effect on  $g_{\text{cond}}^{(2)}$  because all quantities are coincidence counts in the latter. (inset) Raman spectrum of the fiber with collected wavelengths noted. We collect wavelengths outside the main part of the Raman emission.

For comparison, we also measured  $g^{(2)}$  of the pulsed Ti:Sapphire pump laser and found it to be equal to the expected value of one for all applied power levels, demonstrating that our pump laser approximates an ideal coherent source. Note that for the measurement of the pump laser,  $g^{(2)}$  is plotted versus pump powers that produce similar detected idler photon rates as the detected photon rates for

the  $g^{(2)}$  measurement of the laser (Fig. 5.3).

Our Source				
$\lambda_{\text{signal}}$ (nm)	$\lambda_{\text{idler}}$ (nm)	$g_{\text{cond}}^{(2)}$	Pair rate ( $\text{s}^{-1}$ )	$p(1)$
697	790	0.039(3)	280	0.47
		0.140(4)	2910	0.53
		0.330(8)	11900	0.60
693	795	0.014(2)	350	0.51
		0.095(3)	3210	0.54
		0.300(7)	14400	0.59
689	800	0.023(2)	330	0.51
		0.096(3)	3240	0.57
		0.290(7)	12700	0.63
686	805	0.029(3)	290	0.46
		0.110(3)	2660	0.52
		0.310(8)	11900	0.58
SPDC source [129]				
810	1550	0.0014(3)	350	0.61

Table 5.1: Some values of  $g_{\text{cond}}^{(2)}$ , detected signal-idler pair rates, and probability of emitting an idler photon given detection of a signal photon,  $p(1)$ , for different pump powers and signal-idler wavelengths along with data for a high quality SPDC source. Uncertainties are one standard deviation and represent statistical errors.

We list some values of conditional  $g_{\text{cond}}^{(2)}$  at various wavelengths in Table 5.1. In addition to  $g_{\text{cond}}^{(2)}$  we note the detected pair rate (recall that the pulse repetition is 76 MHz) and the probability of idler emission given a signal detection based on our measured idler detection efficiency of 7 %. At  $350 \text{ s}^{-1}$  detected coincidence rate, we have  $g_{\text{cond}}^{(2)}$  as low as 0.014, suppressed by a factor of more than 50 relative to the classical, Poissonian limit of one. This detected pair rate corresponds to 50  $\mu\text{W}$  average pump power (80 mW peak pump power) and, with our idler detection efficiency of 7 %, the probability of emitting an idler photon from the end of the fiber given detection of a signal photon is  $p(1) = 0.51$ .

As the coincidence rate is increased (by increasing the pump power),  $g_{\text{cond}}^{(2)}$  in-

creases due to the increased number of multi-pair events. At a detected coincidence rate of  $12000 \text{ s}^{-1}$  (peak pump power = 490 mW,  $p(1) = 0.6$ ,  $g_{\text{cond}}^{(2)} = 0.3$ ) we still observe suppression of multi-photon events below the classical limit. For a given coincidence rate,  $g_{\text{cond}}^{(2)}$  remains the same over a broad spectral range. For comparison, we include in Table 5.1 a high quality SPDC source which exhibits  $g_{\text{cond}}^{(2)}$  as low as 0.0014 at a bandwidth of  $\Delta\lambda = 6.9 \text{ nm}$ , a pump power (continuous wave) of 1.6 mW, and  $p(1) = 0.61$  [129].

## 5.2 Non-local realism

Quantum theory confounds our conventional perceptions of locality (events in spacelike separated regions cannot affect each other) and realism (the idea that an external reality exists independent of observation). Entanglement, for example, which lies at the heart of quantum theory, connects two polarization-entangled photons such that by measuring the polarization of photon 1, the polarization information of photon 2 is immediately determined, even when these two photons are spacelike separated. This behavior runs counter to our everyday experience with locality and realism. Locality demands the conservation of causality, meaning that information cannot be exchanged between two spacelike separated parties or actions, while realism requires that physical observations are properties possessed by the system whether observed or not. Quantum theory offers only probabilistic explanations to physical observations. Hidden-variable theories are an attempt to complete this description in the sense described by Einstein, Podolsky, and Rosen [5].

In local hidden-variable (LHV) theories, the quantum state of a physical system is completely characterized by a unique set of hidden variables ( $\lambda$ ) and a system-defined distribution function  $\rho(\lambda)$ . In the case where photon polarization is the observable of interest, the expectation value of the polarization observable ( $A$ ) on photon 1 is given as  $\bar{A} = \int_{\lambda} A(\lambda)\rho(\lambda)d\lambda$ , which is independent of the same measurement conducted on photon 2,  $\bar{B} = \int_{\lambda} B(\lambda)\rho(\lambda)d\lambda$ .

Even without assuming explicit forms of the hidden variables and their distribution functions, it is possible to make experimentally testable predictions with LHV theories. The most famous prediction is Bell's theorem [6], which proves that the predictions of quantum mechanics do not agree with local realistic theories. Experimental investigations of Bell's theorem typically test the Clauser, Horne, Shimony, and Holt (CHSH) form of Bell's inequality [130]. The violation of this inequality has been consistently reported in many experiments [7], and the primary loopholes have been closed in various systems [131–133] and are likely to be closed in a single test in the next few years. These experimental results strongly suggesting that LHV theories are invalid and we must abandon either locality or realism, if not both. However tests of the CHSH inequality do not tell us which (locality or realism) to abandon.

In going beyond LHV theories, Leggett defined a class of non-local hidden variable (NLHV) theories, violation of which supports abandoning realism by ruling out both local and non-local realism [26]. For the class of NLHV theories, expectation values of observables depend on the orientations of polarization analyzers  $\vec{a}$  (in detecting photon 1 which has polarization  $\vec{u}$ ) and  $\vec{b}$  (in detecting photon 2

which has polarization  $\vec{v}$ ,  $\overline{A}(\vec{u}) = \int_{\lambda} d\lambda \rho_{\vec{u},\vec{v}}(\lambda) A(\vec{a}, \vec{b}, \lambda) = \vec{u} \cdot \vec{a}$ ,  $\overline{B}(\vec{v}) = \int_{\lambda} d\lambda \rho_{\vec{u},\vec{v}}(\lambda) B(\vec{a}, \vec{b}, \lambda) = \vec{v} \cdot \vec{b}$ , and  $\overline{AB}(\vec{u}) = \int_{\lambda} d\lambda \rho_{\vec{u},\vec{v}}(\lambda) A(\vec{a}, \vec{b}, \lambda) B(\vec{a}, \vec{b}, \lambda)$ , where  $\rho_{\vec{u},\vec{v}}(\lambda)$  is the distribution function in the subensemble space spanned by photon 1 and photon 2 of different hidden variables. The joint property is averaged over all subensemble spaces,  $\langle AB \rangle = \int \int_{\vec{u},\vec{v}} d\vec{u} d\vec{v} F(\vec{u}, \vec{v}) \overline{AB}(\vec{u}, \vec{v})$ , where,  $F(\vec{u}, \vec{v})$  is the distribution function and  $\int_{\lambda} d\lambda \rho_{\vec{u},\vec{v}}(\lambda) = \int \int_{\vec{u},\vec{v}} d\vec{u} d\vec{v} F(\vec{u}, \vec{v}) = 1$ . Leggett theoretically proved that the prediction of this class of NLHV theories is incompatible with quantum theory, based on which, Gröblacher *et al.* further introduced a Leggett-type NLHV inequality to make this class of NLHV theories experimentally testable using polarization-entangled photon-pairs [134].

The introduced Leggett-type NLHV inequality [134] is expressed as

$$\begin{aligned} S_{NLHV} &= |E_{11}(\phi) + E_{23}(0)| + |E_{22}(\phi) + E_{23}(0)| \\ &\leq 4 - \frac{4}{\pi} \left| \sin \frac{\phi}{2} \right|, \end{aligned} \tag{5.1}$$

where  $E_{11}(\phi)$ ,  $E_{23}(0)$ , and  $E_2(\phi)$  are given as

$$E_{ij} = \frac{C_{ij} + C_{i^{\perp}j^{\perp}} - C_{ij^{\perp}} - C_{i^{\perp}j}}{C_{ij} + C_{i^{\perp}j^{\perp}} + C_{ij^{\perp}} + C_{i^{\perp}j}}. \tag{5.2}$$

$C_{ij}$  is the joint correlation measurement,  $C_{ij} = \int \int_{\vec{u},\vec{v},\lambda} d\vec{u} d\vec{v} d\lambda F(\vec{u}, \vec{v}) A(\vec{a}_i, \vec{b}_j, \lambda) B(\vec{a}_i, \vec{b}_j, \lambda) \rho(\vec{u}, \vec{v})$ , with  $A(\vec{a}_i, \vec{b}_j, \lambda) = 1$  for detecting photon 1 and  $A(\vec{a}_i, \vec{b}_j, \lambda) = -1$  for failing to detect photon 1 (and similarly for  $B(\vec{a}_i, \vec{b}_j, \lambda)$  and photon 2). The subscripts  $i$ ,  $j$ ,  $i^{\perp}$ , and  $j^{\perp}$  correspond to polarization analyzer settings with orientations along  $\vec{a}_i$ ,  $\vec{b}_j$ ,  $\vec{a}_{i^{\perp}}$  (orthogonal to  $\vec{a}_i$ ), and  $\vec{b}_{j^{\perp}}$ , respectively.

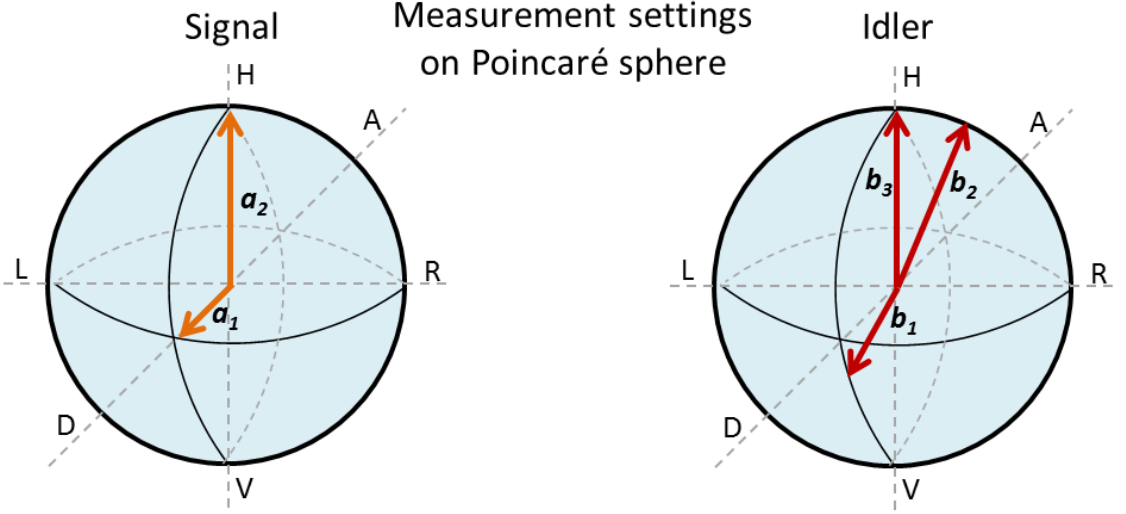


Figure 5.4: Poincaré spheres showing the polarization analyzer settings in detecting the signal (left) and idler (right) photons.

As shown in Fig. 5.4, with orientations of polarization analyzers chosen to have the plane  $\vec{a}_1 \times \vec{b}_1$  orthogonal to the plane  $\vec{a}_2 \times \vec{b}_2$  in the Poincaré sphere, and  $\vec{a}_2 = \vec{b}_3$ , at  $\phi = 18.8^\circ$  ( $\sin\phi = \frac{|\vec{a}_1 \times \vec{b}_1|}{|\vec{a}_1||\vec{b}_1|} = \frac{|\vec{a}_2 \times \vec{b}_2|}{|\vec{a}_2||\vec{b}_2|}$ ), quantum theory predicts  $S_{\text{NLHV}} = 2(1 + \cos\phi) = 3.893$  for polarization-entangled photon pairs of singlet, while the class of NLHV theories to be examined gives a bound of 3.792, resulting in the maximal violation of the inequality, thus excluding a class of NLHV theories [134]. In the meantime, the Bell's inequality can be examined in the form of

$$S_{\text{CHSH}} = |E_{11}(\phi) + E_{12}(\phi) + E_{21}(\phi) - E_{22}(\phi)| \leq 2. \quad (5.3)$$

At  $\phi = 18.8^\circ$ , quantum theory predicts  $S_{\text{CHSH}} = 2\cos\phi + \sin\phi = 2.215$ , while the LHV limit is 2 at all angles, thus simultaneously invalidating the LHV theories.

In addition to the derivation of the Leggett type NLHV inequality, Gröblacher *et al.* conducted the first experiment to show the violation of this inequality us-

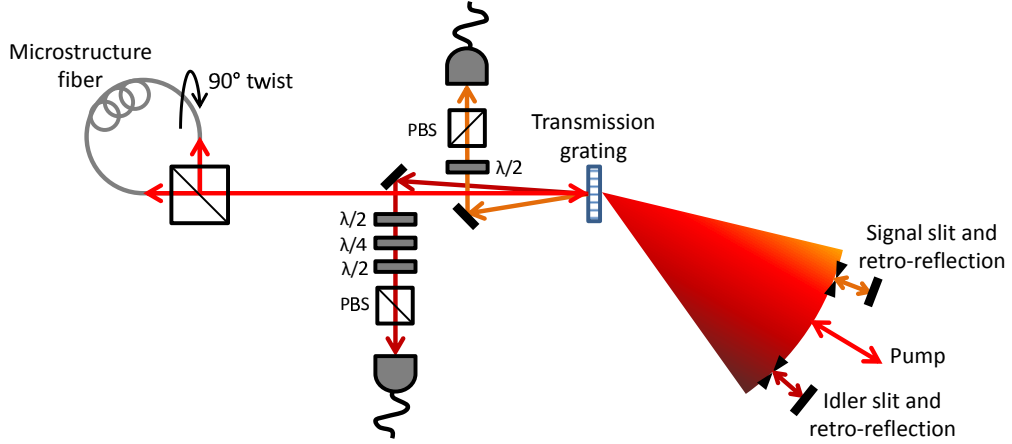


Figure 5.5: Schematic of the experimental setup. PBS: polarizing beam splitter,  $\lambda/2$ : half-wave plate,  $\lambda/4$ : quarter-wave plate. The Sagnac interferometer outputs Bell states in the form of  $\Phi^- = \frac{1}{\sqrt{2}}(H_{\text{signal}}H_{\text{idler}} - V_{\text{signal}}V_{\text{idler}})$ , which are rotated to be the singlet state  $\psi^- = \frac{1}{\sqrt{2}}(H_1V_2 - V_1H_2)$  by the first half-wave plate in the idler arm.

ing polarization-entangled photon pairs created via spontaneous parametric down conversion [134]. We examine Bell's inequality and the Leggett type NLHV inequality using a polarization-entangled two-photon singlet state  $\psi^- = \frac{1}{\sqrt{2}}(H_1V_2 - V_1H_2)$  where  $H_i(V_j)$  denotes that photon  $i(j)$  is horizontally(vertically) polarized. We show the simultaneous violations of the local and non-local inequalities by 15 and 3 standard deviations respectively, excluding LHV and a class of NLHV theories.

We use the fiber-based pair source described above, this time in a Sagnac interferometer configuration (Fig. 5.5) to generate our entangled photons. The microstructure fiber is polarization maintaining and its principal axis is twisted by  $90^\circ$  from one end to the other. Two identical pump pulses (8 ps,  $\lambda_p=740.7$  nm, repetition rate 76 MHz) counterpropagate along the fiber with each creating biphoton states over a broad spectral range via FWM. The twisted fiber configuration causes

the biphoton states from the two FWM processes, which are cross-polarized with respect to each other, to combine on the polarizing beamsplitter to form polarization entangled pairs. The same two-pass grating configuration used in the previous experiment is used to select the signal-idler wavelength pairs (bandwidth  $\Delta\lambda = 0.9$  nm). With appropriate phase control of the pump, the Sagnac configuration outputs the Bell state  $\Phi^- = \frac{1}{\sqrt{2}}(H_{\text{signal}}H_{\text{idler}} - V_{\text{signal}}V_{\text{idler}})$  [123]. A half-wave plate in the idler path converts this to the singlet state.

Considering the rotational symmetry of the singlet state, the correlation measurement of  $C_{ij}$  can be obtained from two-photon coincidence events counted for a few groups of polarization analyzer settings. Following the experimental scheme proposed by Gröblacher *et al.* [134], the orientations of the polarization analyzers are chosen to have  $\vec{a}_1 = D$  ( $D$  is diagonal  $H + V$ ),  $\vec{b}_1$  at an angle  $\phi$  to  $\vec{a}_1$  in the  $D \times H$  plane,  $\vec{a}_2 = H$ ,  $\vec{b}_2$  at an angle  $\phi$  to  $\vec{a}_2$  in the  $H \times L$  plane ( $L$  is left circular  $H + iV$ ), and  $\vec{b}_3 = \vec{a}_2$ . A half-wave plate and a polarizing beamsplitter allow linear polarization analysis of the signal. For the idler, we perform more general elliptical polarization analysis and use a quarter-wave plate, a half-wave plate, and a polarizing beamsplitter.

With a two-photon coincidence rate of  $3500 \text{ s}^{-1}$  we measure interference visibilities greater than 97 % for the singlet state in the H-V, A-D, and L-R bases (Table 5.2). As shown in Fig. 5.6, the violations of the non-local and local inequalities occur for a range of polarization analyzer settings. At  $\phi = 20^\circ$  we observe simultaneous violations of the non-local and local inequalities by 3 and 15 standard deviations respectively (Table 5.2). This violation demonstrates not only the quantum nature



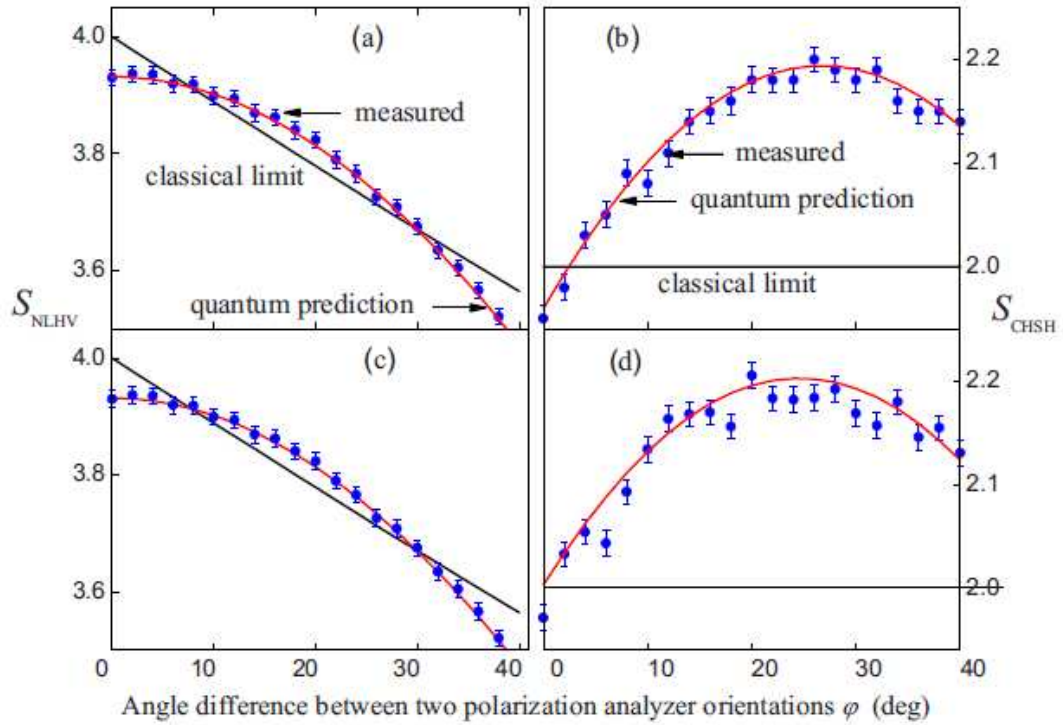


Figure 5.6: Measured values (blue circles), the quantum prediction (red line), and the classical limit (black line) of  $S_{\text{NLHV}}$  [(a) and (c)] and  $S_{\text{CHSH}}$  [(b) and (d)] as a function of  $\phi$  at two pairs of wavelengths:  $\lambda_{\text{signal}} = 689 \text{ nm}$ ,  $\lambda_{\text{idler}} = 800 \text{ nm}$  [(a) and (b)],  $\lambda_{\text{signal}} = 685 \text{ nm}$ ,  $\lambda_{\text{idler}} = 805 \text{ nm}$  [(c) and (d)].

of our source, but also its suitability for many quantum information applications that require high-quality entangled photons.

$\lambda_{\text{signal}}$ (nm)	$\lambda_{\text{idler}}$ (nm)	Visibility (%)	Correlation coefficients	Inequality parameter	Violation
685	805	$V_{D/A} =$ 98.5(8)	$E_{23} = -0.9886(71)$		
		$V_{R/L} =$ 97.5(8)	$E_{11} = -0.8776(66)$	$S_{\text{NLHV}} =$ 3.824(14)	$3.2\sigma$
		$V_{H/V} =$ 98.6(7)	$E_{22} = -0.9689(74)$		
			$E_{12} = -0.0637(55)$	$S_{\text{CHSH}} =$ 2.176(13)	$14\sigma$
			$E_{21} = -0.3935(51)$		
689	800	$V_{D/A} =$ 99.0(8)	$E_{23} = -0.9902(76)$		
		$V_{R/L} =$ 98.0(8)	$E_{11} = -0.8949(75)$	$S_{\text{NLHV}} =$ 3.831(15)	$3.4\sigma$
		$V_{H/V} =$ 99.0(7)	$E_{22} = -0.9557(81)$		
			$E_{12} = -0.0555(60)$	$S_{\text{CHSH}} =$ 2.205(12)	$17\sigma$
			$E_{21} = -0.3886(56)$		

Table 5.2: Summary of local and non-local realism test measured for two sets of wavelengths. The non-local inequality parameters were extracted from  $E_{23}$ ,  $E_{11}$ , and  $E_{22}$  while the local inequality parameters were extracted from  $E_{11}$ ,  $E_{22}$ ,  $E_{12}$ , and  $E_{21}$ . All measurements here are at  $\phi = 20^\circ$ . Visibilities given here are after subtracting background coincidences and all uncertainties are one standard deviation. Violations are calculated by subtracting the classical limits for  $S_{\text{NLHV}}$  and  $S_{\text{CHSH}}$  from the measured values and dividing by the standard deviation.

### 5.3 Mode reconstruction

We presented in chapter 2 a method for reconstructing the underlying modes of a light field using the photon number statistics of the field. Characterizing the underlying mode spectrum of a light field has wide ranging applications including

mode-matching biphoton collection [54], producing factorizable states of photon pairs [23], minimizing classical background emission from single-emitter sources [55], and characterizing the number and degree of squeezing in multimode continuous variable entangled states [52,54,56–59]. Also, full mode reconstruction allows a more subtle distinction between classical and nonclassical fields. Here we present a proof-of-principle experiment demonstrating such a reconstruction for mixed states with contributions from one or more modes with thermal statistics, up to one mode with attenuated single-photon statistics, and up to one mode with Poissonian statistics. We detect with four-fold photon number resolution and successfully identify the distribution of contributions from up to three total modes of classical and non-classical light.

Figure 5.7 shows the three light sources and the photon number resolving detection scheme that we employ for our experimental demonstration. We generate pseudo-thermal light by sending a pulsed laser through a rotating ground glass disk. The random phase and amplitude perturbations imparted on the coherent light by the disk produce an incoherent field that approximates a thermally distributed field [135,136]. We find our pseudo-thermal state has  $g^{(2)} > 1.9$  in all cases, signifying that we are close to a true thermal state ( $g^{(2)} = 2$ ). We use attenuated light directly from the laser for our Poissonian distributed field. And we obtain single photons from a low-noise heralded single-photon source based on SPDC in a periodically-poled lithium niobate crystal [137]. We find that the state of the idler field, conditioned on detection of a signal photon, is close to a single-photon Fock state, with  $g^{(2)} < 0.05$  [137].

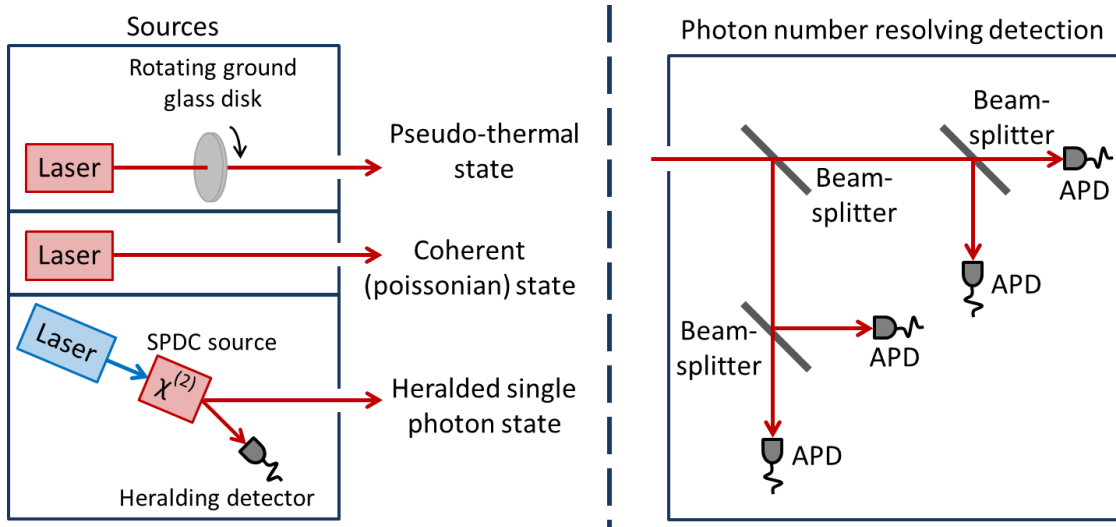


Figure 5.7: Source and detector configurations. SPDC: spontaneous parametric down conversion. APD: avalanche photo-diode.

We combine up to three pulsed modes of such light using beam splitters and insert short time delays between the fields to avoid coherent interference between them. We detect the resulting field with four single-photon avalanche diodes in a tree configuration. After some post-processing of the data according to the positive-operator valued measure of the detection system, we obtain photon number resolution up to four photons [37]. We perform a least-squares minimization over the space of all possible mode configurations to find the distribution that best fits the measured photon number statistics.

We point out that our method can reconstruct all modes within the (typically broad) spectral range of the detector and can reconstruct spectral modes with arbitrarily small frequency difference. And our reconstruction requires only a single measurement of the photon number distribution of the field, unlike most quantum tomography procedures, which require measurements in multiple config-

urations to reconstruct the unknown quantum state [138]. We use a pulsed source with pulse length much shorter than the coherence time of the pseudo-thermal light to ensure that the detection window is within the temporal width of the photon bunching [136]. The temporal resolution of the detection, set by the shorter of the detector resolution and the pulse duration, must be within the coherence time of the source to perform an accurate reconstruction. For applications such as SPDC, pulsed excitation is a common operation and generally ensures correct measurement of the zero-time correlation functions [139].

We take data in a variety of regimes. We define a fidelity of reconstruction as

$$f = \frac{2 |\vec{\mu}_m \cdot \vec{\mu}_r|}{(|\vec{\mu}_m|^2 + |\vec{\mu}_r|^2)} \quad (5.4)$$

where  $\vec{\mu}_m$  and  $\vec{\mu}_r$  are the sets of measured and reconstructed mean photon numbers respectively. This fidelity goes to one if the measured and reconstructed values are identical.

First, we detect fields containing one, two, and three thermal modes. We use the data to reconstruct detected photon numbers in three thermal modes. Figure 5.8 shows examples of these fits for one, two, and three incident thermal modes. We find excellent agreement for a range of powers with  $f \geq 0.98$  in all cases. In addition, the reconstruction correctly identifies the actual number of modes present and sets the remaining mean photon numbers to zero.

Reconstructing a set of modes with underlying thermal statistics is useful for applications involving photon pair sources with such statistics, such as SPDC-based

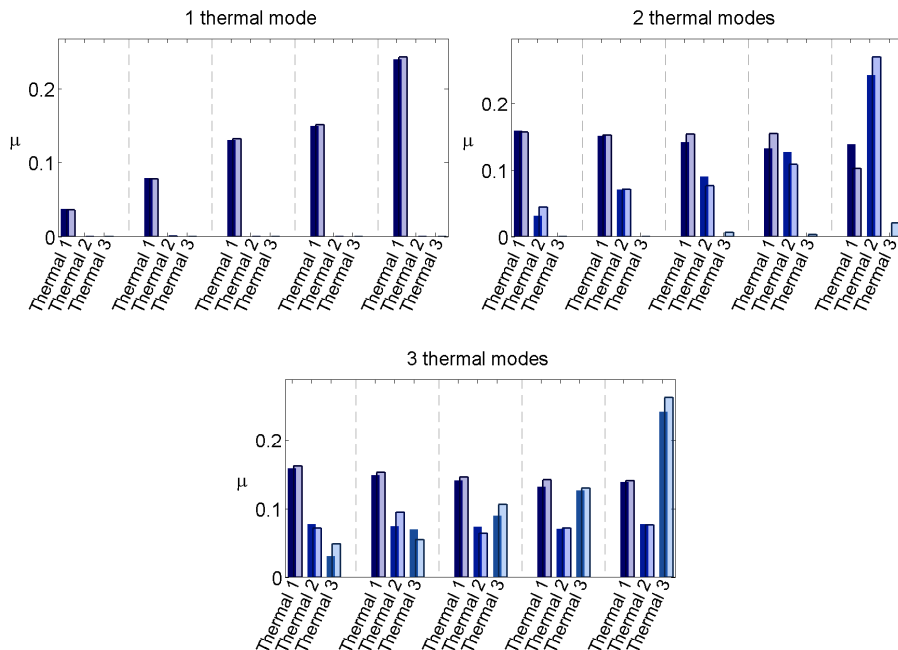


Figure 5.8: Bar heights are mean photon numbers  $\mu$ . Each group of three bars represents a single experiment with a particular set of mean photon numbers. Dark bars in back are measured mean photon numbers,  $\vec{\mu}_m$ , and translucent bars overlaid are the reconstructed mean photon numbers,  $\vec{\mu}_r$ . Noted above each plot is the set of input modes.

sources. In particular, there are applications which require performing a Schmidt decomposition of such a source [23, 140, 141] or ensuring the overlap of collected pairwise modes from a highly multi-mode source [54]. Our method, if applied to the pairwise statistics of such a source, would reconstruct the distribution of pairwise modes without the need to measure the spectral or spatial distribution of the pairs. The extension of this method to pairwise statistics is, however, beyond the scope of this thesis.

We next take data with zero, one, and two thermal modes plus one Poissonian mode and fit it to two thermal modes plus one Poissonian mode. We also fit data with two input thermal modes to a distribution with two thermal modes plus one

Poissonian mode. In Fig. 5.9, we see excellent agreement for a range of input powers with  $f \geq 0.99$  in all cases and correctly identify which modes are present and which are absent.

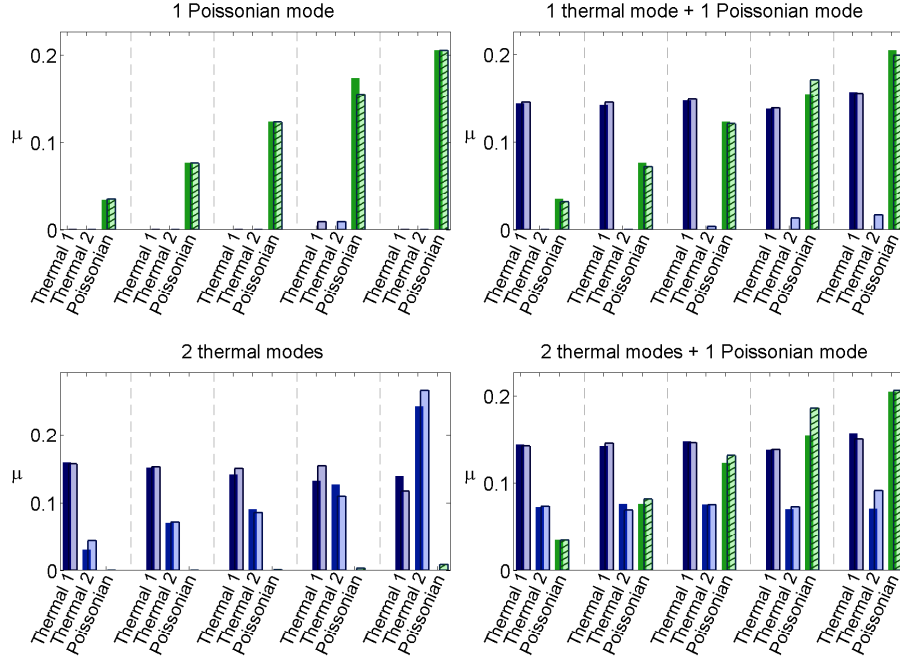


Figure 5.9: Bar heights are mean photon numbers  $\mu$ . Each group of three bars represents a single experiment with a particular set of mean photon numbers. Dark bars in back are measured mean photon numbers,  $\vec{\mu}_m$ , and translucent bars overlaid are the reconstructed mean photon numbers,  $\vec{\mu}_r$ . Blue bars are thermal modes and rightmost, green, crosshatched bar is Poissonian mode. Noted above each plot is the actual set of input modes.

Many sources of non-classical light for quantum information applications, such as SPDC or four-wave mixing, produce single- or multi-mode light with thermal statistics. In these cases it is important to ensure the desired state is not polluted by laser light, which has Poissonian statistics. Our method identifies how much laser pollution is present, even at the same frequency as the thermal light.

Finally, we take data for the SPDC-based heralded single-photon source described above. We fit the data to two thermal modes plus one single photon mode.

We also combine the single photon data with data for a single thermal mode and fit it to two thermal modes plus one single photon mode. In Fig. 5.10 we again find excellent agreement for a range of input powers with  $f \geq 0.96$  in all cases and our method identifies how many modes (up to three) and which type of mode are present.

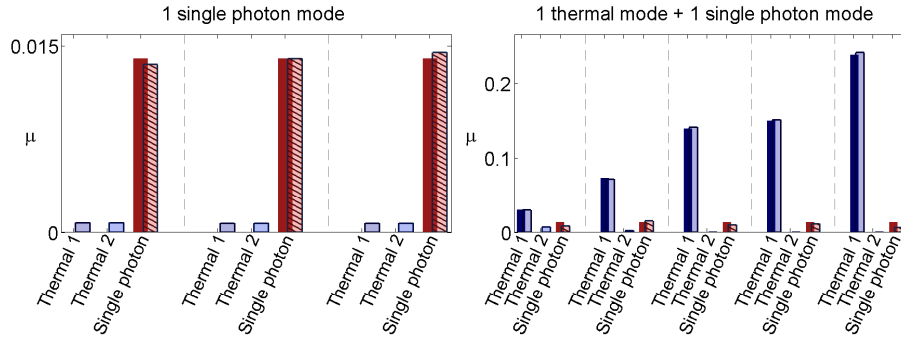


Figure 5.10: Bar heights are mean photon numbers  $\mu$ . Each group of three bars represents a single experiment with a particular set of mean photon numbers. Dark bars in back are measured mean photon numbers,  $\vec{\mu}_m$ , and translucent bars overlaid are the reconstructed mean photon numbers,  $\vec{\mu}_r$ . Blue bars are thermal modes and rightmost, red, crosshatched bar is single-photon mode. Noted above each plot is the set of input modes.

In the second case in Fig. 5.10, the non-classical source is heavily polluted with classical thermal light. The mixing of non-classical and thermal light is common to heralded single photon sources such as those based on SPDC, because the unheralded statistics are thermal. All the states of mixed classical and non-classical light are in the nominally classical regime ( $g^{(2)} > 1$ ). However our method is robust enough to identify the presence of the non-classical component, even when there is a strong classical component present masking the non-classical field.

Our method clearly recognizes cases where only one or two modes are present as well as faithfully reconstructing all modes present. We obtain substantially more



information than is contained in the second order correlation function alone, particularly in the cases where we allow the reconstruction to determine the occupation of modes with different statistics. With additional detectors, or a true photon number resolving detector, we should be able to reconstruct more modes, and do so more faithfully.

## Chapter 6: Conclusion and outlook

We have presented a variety of experimental and theoretical work toward the generation, characterization, storage, and detection of non-classical light with an eye toward applications in quantum information. We characterized a heralded single photon source based on four wave mixing in microstructure optical fiber and showed that such a source produces high purity single photons over a broad spectral bandwidth. We demonstrated storage and retrieval of collective excitations in a solid-state rare-earth doped system, a necessary step toward implementing a quantum memory in such a system. We studied how photon number resolved detection can improve resolution for metrological applications. And finally we developed and implemented a method to use photon number statistics to reconstruct the underlying mode spectrum of a multi-mode light field.

Some extensions of this work are already underway. We are moving toward the single excitation limit in our quantum memory scheme. This requires a narrow spectral filter that can reject the bright, classical write and read fields so that we can detect single heralding and retrieved photons with single photon detectors, which do not have the spectral resolution that our heterodyne detection scheme provides but can detect at the single photon level. We have already demonstrated such a

filter and are working toward integrating it into our system. The RASE protocol, which is similar to the DLCZ scheme, though requires optical  $\pi$ -pulses which add noise, has been demonstrated at the single photon limit by collaborators in [91].

We are also applying our mode reconstruction method to a quantum dot-based single photon source. We are combining higher order photon number detection with temporally resolved detection to better understand the sources of both multi-photon emission and distinguishability when exciting the quantum dot in a variety of regimes. As quantum dots become more common as bases for single photon sources, improved metrics are important for characterizing their emission in the context of quantum information applications. We believe that our mode reconstruction method can be used in just such a way for many sources of non-classical light, building up information about many features of a light source without resorting to an entire toolbox of equipment, but rather making a simple measurement of the photon number statistics in a single configuration.

## Bibliography

- [1] S. J. Freedman and J. F. Clauser, “Experimental Test of Local Hidden-Variable Theories,” *Phys. Rev. Lett.* **28**, 938–941 (1972).  
<http://link.aps.org/doi/10.1103/PhysRevLett.28.938>  
(Cited on page 1.)
- [2] D. J. Wineland, R. E. Drullinger, and F. L. Walls, “Radiation-Pressure Cooling of Bound Resonant Absorbers,” *Phys. Rev. Lett.* **40**, 1639–1642 (1978).  
<http://link.aps.org/doi/10.1103/PhysRevLett.40.1639>  
(Cited on page 1.)
- [3] S. Haroche, “Nobel Lecture: Controlling photons in a box and exploring the quantum to classical boundary,” *Rev. Mod. Phys.* **85**, 1083–1102 (2013).  
<http://link.aps.org/doi/10.1103/RevModPhys.85.1083>  
(Cited on page 1.)
- [4] D. J. Wineland, “Nobel Lecture: Superposition, entanglement, and raising Schrödinger’s cat,” *Rev. Mod. Phys.* **85**, 1103–1114 (2013).  
<http://link.aps.org/doi/10.1103/RevModPhys.85.1103>  
(Cited on page 1.)
- [5] A. Einstein, B. Podolsky, and N. Rosen, “Can Quantum-Mechanical Description of Physical Reality Be Considered Complete?” *Phys. Rev.* **47**, 777–780 (1935).  
<http://link.aps.org/doi/10.1103/PhysRev.47.777>  
(Cited on pages 1, 5, and 90.)
- [6] J. S. Bell, “On the Einstein-Podolsky-Rosen paradox,” *Physics* **1**, 195–200 (1964).  
<http://philoscience.unibe.ch/documents/TexteHS10/bell1964epr.pdf>  
(Cited on pages 1, 5, and 91.)
- [7] A. Aspect, P. Grangier, and G. Roger, “Experimental Tests of Realistic Local Theories via Bell’s Theorem,” *Phys. Rev. Lett.* **47**, 460–463 (1981).

<http://link.aps.org/doi/10.1103/PhysRevLett.47.460>  
(Cited on pages [1](#) and [91](#).)

- [8] R. P. Feynman, “Simulating physics with computers,” *International Journal of Theoretical Physics* **21**, 467–488 (1982).  
<http://dx.doi.org/10.1007/BF02650179>  
(Cited on page [1](#).)
- [9] D. Deutsch, “Quantum Theory, the Church-Turing Principle and the Universal Quantum Computer,” *Proceedings of the Royal Society of London. A. Mathematical and Physical Sciences* **400**, 97–117 (1985).  
<http://rspa.royalsocietypublishing.org/content/400/1818/97.abstract>  
(Cited on page [1](#).)
- [10] W. K. Wootters and W. H. Zurek, “A single quantum cannot be cloned,” *Nature* **299**, 802–803 (1982).  
<http://dx.doi.org/10.1038/299802a0>  
(Cited on page [1](#).)
- [11] C. H. Bennett and G. Brassard, “Quantum Cryptography: Public key distribution and coin tossing,” *Proceedings of the IEEE International Conference on Computers, Systems, and Signal Processing* **1**, 175 (1984).  
<http://www.cs.ucsb.edu/%7Echong/290N-W06/BB84.pdf>  
(Cited on page [1](#).)
- [12] M. A. Nielsen and I. L. Chuang, *Quantum Computation and Quantum Information* (Cambridge University Press, 2000).  
(Cited on page [2](#).)
- [13] P. Kok and B. W. Lovett, *Introduction to Optical Quantum Information Processing* (Cambridge University Press, 2010).  
(Cited on pages [2](#) and [10](#).)
- [14] V. Scarani, H. Bechmann-Pasquinucci, N. J. Cerf, M. Dušek, N. Lütkenhaus, and M. Peev, “The security of practical quantum key distribution,” *Rev. Mod. Phys.* **81**, 1301–1350 (2009).  
<http://link.aps.org/doi/10.1103/RevModPhys.81.1301>  
(Cited on page [3](#).)
- [15] E. Knill, R. Laflamme, and G. J. Milburn, “A scheme for efficient quantum computation with linear optics,” *Nature* **409**, 46–52 (2001).  
<http://dx.doi.org/10.1038/35051009>  
(Cited on pages [3](#) and [8](#).)
- [16] C. K. Hong, Z. Y. Ou, and L. Mandel, “Measurement of subpicosecond time intervals between two photons by interference,” *Phys. Rev. Lett.* **59**, 2044–2046 (1987).

<http://link.aps.org/doi/10.1103/PhysRevLett.59.2044>  
(Cited on page 3.)

- [17] M. D. Eisaman, J. Fan, A. Migdall, and S. V. Polyakov, “Single-photon sources and detectors,” *Review of Scientific Instruments* **82**, 071 101 (2011).  
<http://link.aip.org/link/?RSI/82/071101/1>  
(Cited on pages 3, 4, 8, 26, 29, 70, and 71.)
- [18] E. A. Goldschmidt, M. D. Eisaman, J. Fan, S. V. Polyakov, and A. Migdall, “Spectrally bright and broad fiber-based heralded single-photon source,” *Phys. Rev. A* **78**, 013 844 (2008).  
<http://link.aps.org/doi/10.1103/PhysRevA.78.013844>  
(Cited on pages 3, 4, 34, and 82.)
- [19] P. Michler, A. Kiraz, C. Becher, W. V. Schoenfeld, P. M. Petroff, L. Zhang, E. Hu, and A. Imamoglu, “A Quantum Dot Single-Photon Turnstile Device,” *Science* **290**, 2282–2285 (2000).  
<http://www.sciencemag.org/content/290/5500/2282.abstract>  
(Cited on page 4.)
- [20] J. McKeever, A. Boca, A. D. Boozer, R. Miller, J. R. Buck, A. Kuzmich, and H. J. Kimble, “Deterministic Generation of Single Photons from One Atom Trapped in a Cavity,” *Science* **303**, 1992–1994 (2004).  
<http://www.sciencemag.org/content/303/5666/1992.abstract>  
(Cited on page 4.)
- [21] T. B. Pittman, B. C. Jacobs, and J. D. Franson, “Single photons on pseudo-demand from stored parametric down-conversion,” *Phys. Rev. A* **66**, 042 303 (2002).  
<http://link.aps.org/doi/10.1103/PhysRevA.66.042303>  
(Cited on pages 4 and 7.)
- [22] E. A. Goldschmidt, S. E. Beavan, S. V. Polyakov, A. L. Migdall, and M. J. Sellars, “Storage and retrieval of collective excitations on a long-lived spin transition in a rare-earth ion-doped crystal,” *Opt. Express* **21**, 10 087–10 094 (2013).  
<http://www.opticsexpress.org/abstract.cfm?URI=oe-21-8-10087>  
(Cited on pages 4, 7, and 54.)
- [23] W. Mauerer, M. Avenhaus, W. Helwig, and C. Silberhorn, “How colors influence numbers: Photon statistics of parametric down-conversion,” *Phys. Rev. A* **80**, 053 815 (2009).  
<http://link.aps.org/doi/10.1103/PhysRevA.80.053815>  
(Cited on pages 5, 33, and 100.)
- [24] Z. H. Levine, J. Fan, J. Chen, A. Ling, and A. Migdall, “Heralded, pure-state single-photon source based on a Potassium Titanyl Phosphate waveguide,”

- Opt. Express **18**, 3708–3718 (2010).  
<http://www.opticsexpress.org/abstract.cfm?URI=oe-18-4-3708>  
(Cited on page 5.)
- [25] E. A. Goldschmidt, F. Piacentini, I. Ruo Berchera, S. V. Polyakov, S. Peters, S. Kück, G. Brida, I. P. Degiovanni, A. Migdall, and M. Genovese, “Mode reconstruction of a light field by multiphoton statistics,” Phys. Rev. A **88**, 013822 (2013).  
<http://link.aps.org/doi/10.1103/PhysRevA.88.013822>  
(Cited on pages 5, 8, 9, 34, and 82.)
- [26] A. J. Leggett, “Nonlocal Hidden-Variable Theories and Quantum Mechanics: An Incompatibility Theorem,” Foundations of Physics **33**, 1469–1493 (2003).  
<http://dx.doi.org/10.1023/A%3A1026096313729>  
(Cited on pages 5 and 91.)
- [27] M. D. Eisaman, E. A. Goldschmidt, J. Chen, J. Fan, and A. Migdall, “Experimental test of nonlocal realism using a fiber-based source of polarization-entangled photon pairs,” Phys. Rev. A **77**, 032339 (2008).  
<http://link.aps.org/doi/10.1103/PhysRevA.77.032339>  
(Cited on pages 5 and 82.)
- [28] A. I. Lvovsky, B. C. Sanders, and W. Tittel, “Optical quantum memory,” Nature Photonics **3**, 706–714 (2009).  
<http://dx.doi.org/10.1038/nphoton.2009.231>  
(Cited on pages 5, 40, and 50.)
- [29] P. Kok, W. J. Munro, K. Nemoto, T. C. Ralph, J. P. Dowling, and G. J. Milburn, “Linear optical quantum computing with photonic qubits,” Rev. Mod. Phys. **79**, 135–174 (2007).  
<http://link.aps.org/doi/10.1103/RevModPhys.79.135>  
(Cited on page 6.)
- [30] H.-J. Briegel, W. Dür, J. I. Cirac, and P. Zoller, “Quantum Repeaters: The Role of Imperfect Local Operations in Quantum Communication,” Phys. Rev. Lett. **81**, 5932–5935 (1998).  
<http://link.aps.org/doi/10.1103/PhysRevLett.81.5932>  
(Cited on pages 6 and 50.)
- [31] C. H. Bennett, G. Brassard, C. Crépeau, R. Jozsa, A. Peres, and W. K. Wootters, “Teleporting an unknown quantum state via dual classical and Einstein-Podolsky-Rosen channels,” Phys. Rev. Lett. **70**, 1895–1899 (1993).  
<http://link.aps.org/doi/10.1103/PhysRevLett.70.1895>  
(Cited on pages 6 and 52.)
- [32] B. L. Glebov, J. Fan, and A. Migdall, “Deterministic generation of single photons via multiplexing repetitive parametric downconversions,” Applied Physics

Letters **103**, 031 115 (2013).  
<http://link.aip.org/link/?APL/103/031115/1>  
(Cited on page 7.)

- [33] G. Heinze, C. Hubrich, and T. Halfmann, “Stopped Light and Image Storage by Electromagnetically Induced Transparency up to the Regime of One Minute,” *Phys. Rev. Lett.* **111**, 033 601 (2013).  
<http://link.aps.org/doi/10.1103/PhysRevLett.111.033601>  
(Cited on pages 7, 45, 53, and 54.)
- [34] J. J. Longdell, E. Fraval, M. J. Sellars, and N. B. Manson, “Stopped Light with Storage Times Greater than One Second Using Electromagnetically Induced Transparency in a Solid,” *Phys. Rev. Lett.* **95**, 063 601 (2005).  
<http://link.aps.org/doi/10.1103/PhysRevLett.95.063601>  
(Cited on pages 7, 45, 53, and 54.)
- [35] M. P. Hedges, J. J. Longdell, Y. Li, and M. J. Sellars, “Efficient quantum memory for light,” *Nature* **465**, 1052–1056 (2010).  
<http://dx.doi.org/10.1038/nature09081>  
(Cited on pages 7, 53, and 64.)
- [36] R. H. Hadfield, “Single-photon detectors for optical quantum information applications,” *Nature Photonics* **3**, 696–705 (2009).  
<http://dx.doi.org/10.1038/nphoton.2009.230>  
(Cited on page 8.)
- [37] G. Brida, L. Ciavarella, I. P. Degiovanni, M. Genovese, A. Migdall, M. G. Mingolla, M. G. A. Paris, F. Piacentini, and S. V. Polyakov, “Ancilla-Assisted Calibration of a Measuring Apparatus,” *Phys. Rev. Lett.* **108**, 253 601 (2012).  
<http://link.aps.org/doi/10.1103/PhysRevLett.108.253601>  
(Cited on pages 8, 34, 71, and 98.)
- [38] S. A. Castelletto, I. P. Degiovanni, V. Schettini, and A. L. Migdall, “Reduced deadtime and higher rate photon-counting detection using a multiplexed detector array,” *Journal of Modern Optics* **54**, 337–352 (2007).  
<http://www.tandfonline.com/doi/abs/10.1080/09500340600779579>  
(Cited on page 8.)
- [39] A. J. Pearlman, A. Ling, E. A. Goldschmidt, C. F. Wildfeuer, J. Fan, and A. Migdall, “Enhancing image contrast using coherent states and photon number resolving detectors,” *Opt. Express* **18**, 6033–6039 (2010).  
<http://www.opticsexpress.org/abstract.cfm?URI=oe-18-6-6033>  
(Cited on pages 8 and 71.)
- [40] R. Loudon, *The Quantum Theory of Light* (Oxford University Press, USA, 2000), 3rd edn.  
(Cited on pages 10, 13, 23, and 29.)



- [41] L. Mandel and E. Wolf, *Optical Coherence and Quantum Optics* (Cambridge University Press, 1995).  
(Cited on pages [10](#), [13](#), [23](#), [29](#), and [35](#).)
- [42] R. J. Glauber, “The Quantum Theory of Optical Coherence,” *Phys. Rev.* **130**, 2529–2539 (1963).  
<http://link.aps.org/doi/10.1103/PhysRev.130.2529>  
(Cited on pages [14](#), [22](#), and [84](#).)
- [43] C. F. McCormick, V. Boyer, E. Arimondo, and P. D. Lett, “Strong relative intensity squeezing by four-wave mixing in rubidium vapor,” *Opt. Lett.* **32**, 178–180 (2007).  
<http://ol.osa.org/abstract.cfm?URI=ol-32-2-178>  
(Cited on pages [18](#), [26](#), and [31](#).)
- [44] C. R. Müller, B. Stoklasa, C. Peuntinger, C. Gabriel, J. Řeháček, Z. Hradil, A. B. Klimov, G. Leuchs, C. Marquardt, and L. L. Sánchez-Soto, “Quantum polarization tomography of bright squeezed light,” *New Journal of Physics* **14**, 085 002 (2012).  
<http://stacks.iop.org/1367-2630/14/i=8/a=085002>  
(Cited on page [18](#).)
- [45] C. T. Lee, “Many-photon antibunching in generalized pair coherent states,” *Phys. Rev. A* **41**, 1569–1575 (1990).  
<http://link.aps.org/doi/10.1103/PhysRevA.41.1569>  
(Cited on page [18](#).)
- [46] E. Waks, B. C. Sanders, E. Diamanti, and Y. Yamamoto, “Highly nonclassical photon statistics in parametric down-conversion,” *Phys. Rev. A* **73**, 033 814 (2006).  
<http://link.aps.org/doi/10.1103/PhysRevA.73.033814>  
(Cited on page [19](#).)
- [47] K. Laiho, M. Avenhaus, and C. Silberhorn, “Characteristics of displaced single photons attained via higher order factorial moments,” *New Journal of Physics* **14**, 105 011 (2012).  
<http://stacks.iop.org/1367-2630/14/i=10/a=105011>  
(Cited on page [19](#).)
- [48] D. T. Pegg and S. M. Barnett, “Phase properties of the quantized single-mode electromagnetic field,” *Phys. Rev. A* **39**, 1665–1675 (1989).  
<http://link.aps.org/doi/10.1103/PhysRevA.39.1665>  
(Cited on page [19](#).)
- [49] D. T. Pegg and S. M. Barnett, “Quantum optical phase,” *Journal of Modern Optics* **44**, 225–264 (1997).  
<http://www.tandfonline.com/doi/abs/10.1080/09500349708241868>  
(Cited on page [19](#).)

- [50] L. Davidovich, “Sub-Poissonian processes in quantum optics,” *Rev. Mod. Phys.* **68**, 127–173 (1996).  
<http://link.aps.org/doi/10.1103/RevModPhys.68.127>  
(Cited on page 19.)
- [51] R. Hanbury Brown and R. Q. Twiss, “Correlations between photons in two coherent beams of light,” *Nature* **177**, 27–29 (1956).  
<http://dx.doi.org/10.1038/177027a0>  
(Cited on page 20.)
- [52] V. Boyer, A. M. Marino, R. C. Pooser, and P. D. Lett, “Entangled Images from Four-Wave Mixing,” *Science* **321**, 544–547 (2008).  
<http://www.sciencemag.org/content/321/5888/544.abstract>  
(Cited on pages 31 and 34.)
- [53] M. D. Reid and D. F. Walls, “Violations of classical inequalities in quantum optics,” *Phys. Rev. A* **34**, 1260–1276 (1986).  
<http://link.aps.org/doi/10.1103/PhysRevA.34.1260>  
(Cited on page 32.)
- [54] G. Brida, M. Genovese, and I. Ruo Berchera, “Experimental realization of sub-shot-noise quantum imaging,” *Nature Photonics* **4**, 227–230 (2010).  
<http://dx.doi.org/10.1038/nphoton.2010.29>  
(Cited on pages 33, 34, and 100.)
- [55] E. B. Flagg, S. V. Polyakov, T. Thomay, and G. S. Solomon, “Dynamics of Nonclassical Light from a Single Solid-State Quantum Emitter,” *Phys. Rev. Lett.* **109**, 163601 (2012).  
<http://link.aps.org/doi/10.1103/PhysRevLett.109.163601>  
(Cited on page 34.)
- [56] A. M. Marino, J. B. Clark, Q. Glorieux, and P. D. Lett, “Extracting spatial information from noise measurements of multi-spatial-mode quantum states,” *The European Physical Journal D* **66**, 1–9 (2012).  
<http://dx.doi.org/10.1140/epjd/e2012-30037-1>  
(Cited on page 34.)
- [57] G. Brida, L. Caspani, A. Gatti, M. Genovese, A. Meda, and I. Ruo Berchera, “Measurement of Sub-Shot-Noise Spatial Correlations without Background Subtraction,” *Phys. Rev. Lett.* **102**, 213602 (2009).  
<http://link.aps.org/doi/10.1103/PhysRevLett.102.213602>  
(Cited on page 34.)
- [58] A. I. Lvovsky and M. G. Raymer, “Continuous-variable optical quantum-state tomography,” *Rev. Mod. Phys.* **81**, 299–332 (2009).  
<http://link.aps.org/doi/10.1103/RevModPhys.81.299>  
(Cited on page 34.)

- [59] B. Kanseri, T. Iskhakov, I. Agafonov, M. Chekhova, and G. Leuchs, “Three-dimensional quantum polarization tomography of macroscopic Bell states,” *Phys. Rev. A* **85**, 022 126 (2012).  
<http://link.aps.org/doi/10.1103/PhysRevA.85.022126>  
 (Cited on page 34.)
- [60] C. Kurtsiefer, S. Mayer, P. Zarda, and H. Weinfurter, “Stable Solid-State Source of Single Photons,” *Phys. Rev. Lett.* **85**, 290–293 (2000).  
<http://link.aps.org/doi/10.1103/PhysRevLett.85.290>  
 (Cited on page 34.)
- [61] D. Press, S. Götzinger, S. Reitzenstein, C. Hofmann, A. Löffler, M. Kamp, A. Forchel, and Y. Yamamoto, “Photon Antibunching from a Single Quantum-Dot-Microcavity System in the Strong Coupling Regime,” *Phys. Rev. Lett.* **98**, 117 402 (2007).  
<http://link.aps.org/doi/10.1103/PhysRevLett.98.117402>  
 (Cited on page 34.)
- [62] W. Schmunk, M. Gramegna, G. Brida, I. P. Degiovanni, M. Genovese, H. Hofer, S. Kück, L. Lolli, M. G. A. Paris, S. Peters, M. Rajteri, A. M. Racu, A. Ruschhaupt, E. Taralli, and P. Traina, “Photon number statistics of NV centre emission,” *Metrologia* **49**, S156 (2012).  
<http://stacks.iop.org/0026-1394/49/i=2/a=S156>  
 (Cited on page 34.)
- [63] A. Kuzmich, W. P. Bowen, A. D. Boozer, A. Boca, C.-W. Chou, L.-M. Duan, and H. J. Kimble, “Generation of nonclassical photon pairs for scalable quantum communication with atomic ensembles,” *Nature* **423**, 731–734 (2003).  
<http://dx.doi.org/10.1038/nature01714>  
 (Cited on page 34.)
- [64] M. Scholz, L. Koch, and O. Benson, “Statistics of Narrow-Band Single Photons for Quantum Memories Generated by Ultrabright Cavity-Enhanced Parametric Down-Conversion,” *Phys. Rev. Lett.* **102**, 063 603 (2009).  
<http://link.aps.org/doi/10.1103/PhysRevLett.102.063603>  
 (Cited on page 34.)
- [65] M. Aßmann, F. Veit, M. Bayer, M. van der Poel, and J. M. Hvam, “Higher-Order Photon Bunching in a Semiconductor Microcavity,” *Science* **325**, 297–300 (2009).  
<http://www.sciencemag.org/content/325/5938/297.abstract>  
 (Cited on page 34.)
- [66] M. Hennrich, A. Kuhn, and G. Rempe, “Transition from Antibunching to Bunching in Cavity QED,” *Phys. Rev. Lett.* **94**, 053 604 (2005).  
<http://link.aps.org/doi/10.1103/PhysRevLett.94.053604>  
 (Cited on page 34.)

- [67] D. Elvira, X. Hachair, V. B. Verma, R. Braive, G. Beaudoin, I. Robert-Philip, I. Sagnes, B. Baek, S. W. Nam, E. A. Dauler, I. Abram, M. J. Stevens, and A. Beveratos, “Higher-order photon correlations in pulsed photonic crystal nanolasers,” *Phys. Rev. A* **84**, 061 802 (2011).  
<http://link.aps.org/doi/10.1103/PhysRevA.84.061802>  
 (Cited on page 34.)
- [68] M. Aßmann, F. Veit, M. Bayer, C. Gies, F. Jahnke, S. Reitzenstein, S. Höfling, L. Worschech, and A. Forchel, “Ultrafast tracking of second-order photon correlations in the emission of quantum-dot microresonator lasers,” *Phys. Rev. B* **81**, 165 314 (2010).  
<http://link.aps.org/doi/10.1103/PhysRevB.81.165314>  
 (Cited on page 34.)
- [69] J. S. Lundeen, A. Feito, H. Coldenstrodt-Ronge, K. L. Pregnell, C. Silberhorn, T. C. Ralph, J. Eisert, M. B. Plenio, and I. A. Walmsley, “Tomography of quantum detectors,” *Nature Physics* **5**, 27–30 (2009).  
<http://dx.doi.org/10.1038/nphys1133>  
 (Cited on page 34.)
- [70] A. E. Lita, A. J. Miller, and S. W. Nam, “Counting near-infrared single-photons with 95% efficiency,” *Opt. Express* **16**, 3032–3040 (2008).  
<http://www.opticsexpress.org/abstract.cfm?URI=oe-16-5-3032>  
 (Cited on page 34.)
- [71] G. Brida, L. Ciavarella, I. P. Degiovanni, M. Genovese, L. Lolli, M. G. Mingolla, F. Piacentini, M. Rajteri, E. Taralli, and M. G. A. Paris, “Quantum characterization of superconducting photon counters,” *New Journal of Physics* **14**, 085 001 (2012).  
<http://stacks.iop.org/1367-2630/14/i=8/a=085001>  
 (Cited on page 34.)
- [72] M. Avenhaus, K. Laiho, M. V. Chekhova, and C. Silberhorn, “Accessing Higher Order Correlations in Quantum Optical States by Time Multiplexing,” *Phys. Rev. Lett.* **104**, 063 602 (2010).  
<http://link.aps.org/doi/10.1103/PhysRevLett.104.063602>  
 (Cited on page 34.)
- [73] D. A. Kalashnikov, S. H. Tan, M. V. Chekhova, and L. A. Krivitsky, “Accessing photon bunching with a photon number resolving multi-pixel detector,” *Opt. Express* **19**, 9352–9363 (2011).  
<http://www.opticsexpress.org/abstract.cfm?URI=oe-19-10-9352>  
 (Cited on page 34.)
- [74] J. F. Dynes, Z. L. Yuan, A. W. Sharpe, O. Thomas, and A. J. Shields, “Probing higher order correlations of the photon field with photon number resolving avalanche photodiodes,” *Opt. Express* **19**, 13 268–13 276 (2011).

<http://www.opticsexpress.org/abstract.cfm?URI=oe-19-14-13268>  
(Cited on page 34.)

- [75] A. V. Gorshkov, A. André, M. Fleischhauer, A. S. Sørensen, and M. D. Lukin, “Universal Approach to Optimal Photon Storage in Atomic Media,” *Phys. Rev. Lett.* **98**, 123 601 (2007).  
<http://link.aps.org/doi/10.1103/PhysRevLett.98.123601>  
(Cited on page 40.)
- [76] Y. O. Dudin, L. Li, and A. Kuzmich, “Light storage on the time scale of a minute,” *Phys. Rev. A* **87**, 031 801 (2013).  
<http://link.aps.org/doi/10.1103/PhysRevA.87.031801>  
(Cited on page 41.)
- [77] C. W. Thiel, T. Böttger, and R. L. Cone, “Rare-earth-doped materials for applications in quantum information storage and signal processing,” *Journal of Luminescence* **131**, 353 – 361 (2011).  
<http://www.sciencedirect.com/science/article/pii/S002223131000534X>  
(Cited on pages 41 and 47.)
- [78] E. Fraval, M. J. Sellars, and J. J. Longdell, “Dynamic Decoherence Control of a Solid-State Nuclear-Quadrupole Qubit,” *Phys. Rev. Lett.* **95**, 030 506 (2005).  
<http://link.aps.org/doi/10.1103/PhysRevLett.95.030506>  
(Cited on pages 41 and 53.)
- [79] A. J. Freeman and R. E. Watson, “Theoretical Investigation of Some Magnetic and Spectroscopic Properties of Rare-Earth Ions,” *Phys. Rev.* **127**, 2058–2075 (1962).  
<http://link.aps.org/doi/10.1103/PhysRev.127.2058>  
(Cited on pages 42 and 43.)
- [80] G. Liu and B. Jacquier, *Spectroscopic Properties of Rare Earths in Optical Materials* (Springer, 2005).  
(Cited on pages 42, 43, and 59.)
- [81] M. Nilsson, L. Rippe, S. Kröll, R. Klieber, and D. Suter, “Hole-burning techniques for isolation and study of individual hyperfine transitions in inhomogeneously broadened solids demonstrated in  $\text{Pr}^{3+}:\text{Y}_2\text{SiO}_5$ ,” *Phys. Rev. B* **70**, 214 116 (2004).  
<http://link.aps.org/doi/10.1103/PhysRevB.70.214116>  
(Cited on pages 42, 46, 49, and 58.)
- [82] G. H. Dieke, in *Spectra and energy levels of rare earth ions in crystals*, H. Crosswhite, ed. (Interscience Publishers, 1968).  
(Cited on pages 43 and 44.)

- [83] J. J. Longdell, M. J. Sellars, and N. B. Manson, “Hyperfine interaction in ground and excited states of praseodymium-doped yttrium orthosilicate,” *Phys. Rev. B* **66**, 035 101 (2002).  
<http://link.aps.org/doi/10.1103/PhysRevB.66.035101>  
 (Cited on page 45.)
- [84] R. W. Equall, R. L. Cone, and R. M. Macfarlane, “Homogeneous broadening and hyperfine structure of optical transitions in  $\text{Pr}^{3+}:\text{Y}_2\text{SiO}_5$ ,” *Phys. Rev. B* **52**, 3963–3969 (1995).  
<http://link.aps.org/doi/10.1103/PhysRevB.52.3963>  
 (Cited on pages 45 and 47.)
- [85] E. Fraval, M. J. Sellars, and J. J. Longdell, “Method of Extending Hyperfine Coherence Times in  $\text{Pr}^{3+}:\text{Y}_2\text{SiO}_5$ ,” *Phys. Rev. Lett.* **92**, 077 601 (2004).  
<http://link.aps.org/doi/10.1103/PhysRevLett.92.077601>  
 (Cited on page 45.)
- [86] S. E. Beavan, E. Fraval, M. J. Sellars, and J. J. Longdell, “Demonstration of the reduction of decoherent errors in a solid-state qubit using dynamic decoupling techniques,” *Phys. Rev. A* **80**, 032 308 (2009).  
<http://link.aps.org/doi/10.1103/PhysRevA.80.032308>  
 (Cited on page 45.)
- [87] R. L. Ahlefeldt, N. B. Manson, and M. J. Sellars, “Optical lifetime and linewidth studies of the  ${}^7\text{F}_0 \rightarrow {}^5\text{D}_0$  transition in  $\text{EuCl}_3 \cdot 6\text{H}_2\text{O}$ : A potential material for quantum memory applications,” *Journal of Luminescence* **133**, 152 – 156 (2013), 16th International Conference on Luminescence ICL’11.  
<http://www.sciencedirect.com/science/article/pii/S0022231311006892>  
 (Cited on page 47.)
- [88] P. M. Ledingham, W. R. Naylor, J. J. Longdell, S. E. Beavan, and M. J. Sellars, “Nonclassical photon streams using rephased amplified spontaneous emission,” *Phys. Rev. A* **81**, 012 301 (2010).  
<http://link.aps.org/doi/10.1103/PhysRevA.81.012301>  
 (Cited on pages 53 and 55.)
- [89] M. Afzelius, I. Usmani, A. Amari, B. Lauritzen, A. Walther, C. Simon, N. Sangouard, J. Minář, H. de Riedmatten, N. Gisin, and S. Kröll, “Demonstration of Atomic Frequency Comb Memory for Light with Spin-Wave Storage,” *Phys. Rev. Lett.* **104**, 040 503 (2010).  
<http://link.aps.org/doi/10.1103/PhysRevLett.104.040503>  
 (Cited on page 53.)
- [90] E. Saglamyurek, N. Sinclair, J. Jin, J. A. Slater, D. Oblak, F. Bussi eres, M. George, R. Ricken, W. Sohler, and W. Tittel, “Broadband waveguide quantum memory for entangled photons,” *Nature* **469**, 512–515 (2011).  
<http://dx.doi.org/10.1038/nature09719>  
 (Cited on page 53.)

- [91] S. E. Beavan, M. P. Hedges, and M. J. Sellars, “Demonstration of Photon-Echo Rephasing of Spontaneous Emission,” *Phys. Rev. Lett.* **109**, 093 603 (2012).  
<http://link.aps.org/doi/10.1103/PhysRevLett.109.093603>  
 (Cited on pages 53, 54, and 105.)
- [92] I. D. Abella, N. A. Kurnit, and S. R. Hartmann, “Photon Echoes,” *Phys. Rev.* **141**, 391–406 (1966).  
<http://link.aps.org/doi/10.1103/PhysRev.141.391>  
 (Cited on page 53.)
- [93] L.-M. Duan, M. D. Lukin, J. I. Cirac, and P. Zoller, “Long-distance quantum communication with atomic ensembles and linear optics,” *Nature* **414**, 413–418 (2001).  
<http://dx.doi.org/10.1038/35106500>  
 (Cited on pages 54 and 57.)
- [94] N. E. Rehler and J. H. Eberly, “Superradiance,” *Phys. Rev. A* **3**, 1735–1751 (1971).  
<http://link.aps.org/doi/10.1103/PhysRevA.3.1735>  
 (Cited on page 60.)
- [95] J. Laurat, H. de Riedmatten, D. Felinto, C.-W. Chou, E. W. Schomburg, and H. J. Kimble, “Efficient retrieval of a single excitation stored in an atomic ensemble,” *Opt. Express* **14**, 6912–6918 (2006).  
<http://www.opticsexpress.org/abstract.cfm?URI=oe-14-15-6912>  
 (Cited on page 64.)
- [96] B. S. Ham and P. R. Hemmer, “Coherence Switching in a Four-Level System: Quantum Switching,” *Phys. Rev. Lett.* **84**, 4080–4083 (2000).  
<http://link.aps.org/doi/10.1103/PhysRevLett.84.4080>  
 (Cited on page 65.)
- [97] B. S. Ham and J. Hahn, “Dichromatic light halting using double spin coherence gratings,” *New Journal of Physics* **13**, 083 012 (2011).  
<http://stacks.iop.org/1367-2630/13/i=8/a=083012>  
 (Cited on page 65.)
- [98] D. Felinto, C.-W. Chou, H. de Riedmatten, S. V. Polyakov, and H. J. Kimble, “Control of decoherence in the generation of photon pairs from atomic ensembles,” *Phys. Rev. A* **72**, 053 809 (2005).  
<http://link.aps.org/doi/10.1103/PhysRevA.72.053809>  
 (Cited on page 67.)
- [99] B. S. Ham, M. S. Shahriar, M. K. Kim, and P. R. Hemmer, “Frequency-selective time-domain optical data storage by electromagnetically induced transparency in a rare-earth-doped solid,” *Opt. Lett.* **22**, 1849–1851 (1997).  
<http://ol.osa.org/abstract.cfm?URI=ol-22-24-1849>  
 (Cited on page 67.)

- [100] S. E. Beavan, E. A. Goldschmidt, and M. J. Sellars, “Demonstration of a dynamic bandpass frequency filter in a rare-earth ion-doped crystal,” *J. Opt. Soc. Am. B* **30**, 1173–1177 (2013).  
<http://josab.osa.org/abstract.cfm?URI=josab-30-5-1173>  
 (Cited on pages 68 and 69.)
- [101] A. J. Miller, S. W. Nam, J. M. Martinis, and A. V. Sergienko, “Demonstration of a low-noise near-infrared photon counter with multiphoton discrimination,” *Applied Physics Letters* **83**, 791–793 (2003).  
<http://link.aip.org/link/?APL/83/791/1>  
 (Cited on pages 71 and 73.)
- [102] M. Giustina, A. Mech, S. Ramelow, B. Wittmann, J. Kofler, J. Beyer, A. Lita, B. Calkins, T. Gerrits, S. W. Nam, R. Ursin, and A. Zeilinger, “Bell violation using entangled photons without the fair-sampling assumption,” *Nature* **497**, 227–230 (2013).  
<http://dx.doi.org/10.1038/nature12012>  
 (Cited on page 71.)
- [103] N. Namekata, Y. Takahashi, G. Fujii, D. Fukuda, S. Kurimura, and S. Inoue, “Non-Gaussian operation based on photon subtraction using a photon-number-resolving detector at a telecommunications wavelength,” *Nature Photonics* **4**, 655–660 (2010).  
<http://dx.doi.org/10.1038/nphoton.2010.158>  
 (Cited on page 71.)
- [104] Z. H. Levine, T. Gerrits, A. L. Migdall, D. V. Samarov, B. Calkins, A. E. Lita, and S. W. Nam, “Algorithm for finding clusters with a known distribution and its application to photon-number resolution using a superconducting transition-edge sensor,” *J. Opt. Soc. Am. B* **29**, 2066–2073 (2012).  
<http://josab.osa.org/abstract.cfm?URI=josab-29-8-2066>  
 (Cited on page 71.)
- [105] S. Lloyd, “Enhanced Sensitivity of Photodetection via Quantum Illumination,” *Science* **321**, 1463–1465 (2008).  
<http://www.sciencemag.org/content/321/5895/1463.abstract>  
 (Cited on page 71.)
- [106] T. Nagata, R. Okamoto, J. L. O’Brien, K. Sasaki, and S. Takeuchi, “Beating the Standard Quantum Limit with Four-Entangled Photons,” *Science* **316**, 726–729 (2007).  
<http://www.sciencemag.org/content/316/5825/726.abstract>  
 (Cited on page 71.)
- [107] J. J. . Bollinger, W. M. Itano, D. J. Wineland, and D. J. Heinzen, “Optimal frequency measurements with maximally correlated states,” *Phys. Rev. A* **54**, R4649–R4652 (1996).



<http://link.aps.org/doi/10.1103/PhysRevA.54.R4649>  
(Cited on page 71.)

- [108] A. N. Boto, P. Kok, D. S. Abrams, S. L. Braunstein, C. P. Williams, and J. P. Dowling, “Quantum Interferometric Optical Lithography: Exploiting Entanglement to Beat the Diffraction Limit,” *Phys. Rev. Lett.* **85**, 2733–2736 (2000).  
<http://link.aps.org/doi/10.1103/PhysRevLett.85.2733>  
(Cited on page 71.)
- [109] M. D’Angelo, M. V. Chekhova, and Y. Shih, “Two-Photon Diffraction and Quantum Lithography,” *Phys. Rev. Lett.* **87**, 013602 (2001).  
<http://link.aps.org/doi/10.1103/PhysRevLett.87.013602>  
(Cited on page 71.)
- [110] J. P. Dowling, “Quantum optical metrology - the lowdown on high-N00N States,” *Contemporary Physics* **49**, 125–143 (2008).  
<http://www.tandfonline.com/doi/abs/10.1080/00107510802091298>  
(Cited on page 71.)
- [111] M. A. Rubin and S. Kaushik, “Loss-induced limits to phase measurement precision with maximally entangled states,” *Phys. Rev. A* **75**, 053805 (2007).  
<http://link.aps.org/doi/10.1103/PhysRevA.75.053805>  
(Cited on page 71.)
- [112] S. J. Bentley and R. W. Boyd, “Nonlinear optical lithography with ultra-high sub-Rayleigh resolution,” *Opt. Express* **12**, 5735–5740 (2004).  
<http://www.opticsexpress.org/abstract.cfm?URI=oe-12-23-5735>  
(Cited on page 71.)
- [113] C. F. Wildfeuer, A. J. Pearlman, J. Chen, J. Fan, A. Migdall, and J. P. Dowling, “Resolution and sensitivity of a Fabry-Perot interferometer with a photon-number-resolving detector,” *Phys. Rev. A* **80**, 043822 (2009).  
<http://link.aps.org/doi/10.1103/PhysRevA.80.043822>  
(Cited on pages 71 and 75.)
- [114] G. Khoury, H. S. Eisenberg, E. J. S. Fonseca, and D. Bouwmeester, “Nonlinear Interferometry via Fock-State Projection,” *Phys. Rev. Lett.* **96**, 203601 (2006).  
<http://link.aps.org/doi/10.1103/PhysRevLett.96.203601>  
(Cited on pages 71 and 75.)
- [115] P. R. Hemmer, A. Muthukrishnan, M. O. Scully, and M. S. Zubairy, “Quantum Lithography with Classical Light,” *Phys. Rev. Lett.* **96**, 163603 (2006).  
<http://link.aps.org/doi/10.1103/PhysRevLett.96.163603>  
(Cited on page 71.)

- [116] N. Treps, N. Grosse, W. P. Bowen, C. Fabre, H.-A. Bachor, and P. K. Lam, “A Quantum Laser Pointer,” *Science* **301**, 940–943 (2003).  
<http://www.sciencemag.org/content/301/5635/940.abstract>  
 (Cited on pages 71 and 72.)
- [117] Lord Rayleigh, “Investigations in optics, with special reference to the spectro-scope,” *Philosophical Magazine Series 5* **8**, 261–274 (1879).  
<http://www.tandfonline.com/doi/abs/10.1080/14786447908639684>  
 (Cited on page 71.)
- [118] V. Giovannetti, S. Lloyd, L. Maccone, and J. H. Shapiro, “Sub-Rayleigh-diffraction-bound quantum imaging,” *Phys. Rev. A* **79**, 013 827 (2009).  
<http://link.aps.org/doi/10.1103/PhysRevA.79.013827>  
 (Cited on pages 72 and 81.)
- [119] A. G. Martin, S. B. Dutta, W. F. Rogers, and D. L. Clark, “Laser spectroscopy of radioactive atoms using the photon-burst technique,” *J. Opt. Soc. Am. B* **4**, 405–412 (1987).  
<http://josab.osa.org/abstract.cfm?URI=josab-4-3-405>  
 (Cited on page 72.)
- [120] C. C. Gerry and P. L. Knight, *Introductory Quantum Optics* (Cambridge University Press, 2005).  
 (Cited on page 75.)
- [121] C. M. Sparrow, “On Spectroscopic Resolving Power,” *Astrophysical Journal* **44**, 76 (1916).  
<http://adsabs.harvard.edu/doi/10.1086/142271>  
 (Cited on page 81.)
- [122] G. P. Agrawal, *Nonlinear Fiber Optics, 2nd ed.* (Academic Press, 1995).  
 (Cited on page 83.)
- [123] J. Fan, M. D. Eisaman, and A. Migdall, “Bright phase-stable broadband fiber-based source of polarization-entangled photon pairs,” *Phys. Rev. A* **76**, 043 836 (2007).  
<http://link.aps.org/doi/10.1103/PhysRevA.76.043836>  
 (Cited on pages 83 and 95.)
- [124] J. Fan and A. Migdall, “A broadband high spectral brightness fiber-based two-photon source,” *Opt. Express* **15**, 2915–2920 (2007).  
<http://www.opticsexpress.org/abstract.cfm?URI=oe-15-6-2915>  
 (Cited on pages 83 and 85.)
- [125] J. Fan, M. D. Eisaman, and A. Migdall, “Quantum state tomography of a fiber-based source of polarization-entangled photon pairs,” *Opt. Express* **15**, 18 339–18 344 (2007).

<http://www.opticsexpress.org/abstract.cfm?URI=oe-15-26-18339>  
(Cited on page 83.)

- [126] R. J. Glauber, “Coherent and Incoherent States of the Radiation Field,” *Phys. Rev.* **131**, 2766–2788 (1963).  
<http://link.aps.org/doi/10.1103/PhysRev.131.2766>  
(Cited on page 84.)
- [127] J. Fan, A. Migdall, J. Chen, and E. A. Goldschmidt, “Microstructure-Fiber-Based Source of Photonic Entanglement,” *IEEE Journal of Selected Topics in Quantum Electronics* **15**, 1724–1732 (2009).  
<http://ieeexplore.ieee.org/xpl/articleDetails.jsp?arnumber=5332292>  
(Cited on page 84.)
- [128] S. V. Polyakov, A. Migdall, and S. W. Nam, “Real-Time Data-Acquisition Platform for Pulsed Measurements,” *AIP Conference Proceedings* **1327**, 505–519 (2011).  
<http://link.aip.org/link/?APC/1327/505/1>  
(Cited on page 87.)
- [129] S. Fasel, O. Alibart, S. Tanzilli, P. Baldi, A. Beveratos, N. Gisin, and H. Zbinden, “High-quality asynchronous heralded single-photon source at telecom wavelength,” *New Journal of Physics* **6**, 163 (2004).  
<http://stacks.iop.org/1367-2630/6/i=1/a=163>  
(Cited on pages 89 and 90.)
- [130] J. F. Clauser, M. A. Horne, A. Shimony, and R. A. Holt, “Proposed Experiment to Test Local Hidden-Variable Theories,” *Phys. Rev. Lett.* **23**, 880–884 (1969).  
<http://link.aps.org/doi/10.1103/PhysRevLett.23.880>  
(Cited on page 91.)
- [131] G. Weihs, T. Jennewein, C. Simon, H. Weinfurter, and A. Zeilinger, “Violation of Bell’s Inequality under Strict Einstein Locality Conditions,” *Phys. Rev. Lett.* **81**, 5039–5043 (1998).  
<http://link.aps.org/doi/10.1103/PhysRevLett.81.5039>  
(Cited on page 91.)
- [132] M. A. Rowe, D. Kielpinski, V. Meyer, C. A. Sackett, W. M. Itano, C. Monroe, and D. J. Wineland, “Experimental violation of a Bell’s inequality with efficient detection,” *Nature* **409**, 791–794 (2001).  
<http://dx.doi.org/10.1038/35057215>  
(Cited on page 91.)
- [133] T. Scheidl, R. Ursin, J. Kofler, S. Ramelow, X.-S. Ma, T. Herbst, L. Ratschbacher, A. Fedrizzi, N. K. Langford, T. Jennewein, and A. Zeilinger, “Violation of local realism with freedom of choice,” *Proceedings of the National Academy of Sciences* **107**, 19 708–19 713 (2010).

<http://www.pnas.org/content/107/46/19708.abstract>  
(Cited on page 91.)

- [134] S. Gröblacher, T. Paterek, R. Kaltenbaek, Č. Brukner, M. Żukowski, M. Aspelmeyer, and A. Zeilinger, “An experimental test of non-local realism,” *Nature* **446**, 871–875 (2007).  
<http://dx.doi.org/10.1038/nature05677>  
(Cited on pages 92, 93, 94, and 95.)
- [135] F. T. Arecchi, “Measurement of the Statistical Distribution of Gaussian and Laser Sources,” *Phys. Rev. Lett.* **15**, 912–916 (1965).  
<http://link.aps.org/doi/10.1103/PhysRevLett.15.912>  
(Cited on page 98.)
- [136] J. H. Churnside, “Speckle from a rotating diffuse object,” *J. Opt. Soc. Am.* **72**, 1464–1469 (1982).  
<http://www.opticsinfobase.org/abstract.cfm?URI=josa-72-11-1464>  
(Cited on pages 98 and 99.)
- [137] G. Brida, I. P. Degiovanni, M. Genovese, A. Migdall, F. Piacentini, S. V. Polyakov, and I. Ruo Berchera, “Experimental realization of a low-noise heralded single-photon source,” *Opt. Express* **19**, 1484–1492 (2011).  
<http://www.opticsexpress.org/abstract.cfm?URI=oe-19-2-1484>  
(Cited on page 98.)
- [138] G. Zambra, A. Andreoni, M. Bondani, M. Gramegna, M. Genovese, G. Brida, A. Rossi, and M. G. A. Paris, “Experimental Reconstruction of Photon Statistics without Photon Counting,” *Phys. Rev. Lett.* **95**, 063 602 (2005).  
<http://link.aps.org/doi/10.1103/PhysRevLett.95.063602>  
(Cited on page 99.)
- [139] P. R. Tapster and J. G. Rarity, “Photon statistics of pulsed parametric light,” *Journal of Modern Optics* **45**, 595–604 (1998).  
<http://www.tandfonline.com/doi/abs/10.1080/09500349808231917>  
(Cited on page 100.)
- [140] W. P. Grice, A. B. U’Ren, and I. A. Walmsley, “Eliminating frequency and space-time correlations in multiphoton states,” *Phys. Rev. A* **64**, 063 815 (2001).  
<http://link.aps.org/doi/10.1103/PhysRevA.64.063815>  
(Cited on page 100.)
- [141] S. S. Straupe, D. P. Ivanov, A. A. Kalinkin, I. B. Bobrov, and S. P. Kulik, “Angular Schmidt modes in spontaneous parametric down-conversion,” *Phys. Rev. A* **83**, 060 302 (2011).  
<http://link.aps.org/doi/10.1103/PhysRevA.83.060302>  
(Cited on page 100.)